PERFORMANCE OF UNBOUND AGGREGATE BASES AND IMPLICATIONS FOR INVERTED BASE PAVEMENTS

A Thesis
Presented to
The Academic Faculty

by

Efthymios G. Papadopoulos

In Partial Fulfillment
of the Requirements for the Degree
of Doctor of Philosophy in the
School of Civil and Environmental Engineering

Georgia Institute of Technology
May 2014

PERFORMANCE OF UNBOUND AGGREGATE BASES AND IMPLICATIONS FOR INVERTED BASE PAVEMENTS

Approved by:

Dr. Juan Carlos Santamarina, Advisor
School of Civil and Environmental Engineering
Georgia Institute of Technology

Dr. Chris Huber
School of Earth and Atmospheric Sciences
Georgia Institute of Technology

Dr. David J. Frost
School of School of Civil and Environmental Engineering
Georgia Institute of Technology

Dr. Glenn J. Rix
Geosyntec Consultants / CEE
Georgia Institute of Technology

Dr. Paul W. Mayne
School of School of Civil and Environmental Engineering
Georgia Institute of Technology

Date Approved: April 2nd 2014

To free thinking

ACKNOWLEDGEMENTS

I would like to express my gratitude to my professors at Georgia Tech, as they stimulated my creativity and taught me the foundation knowledge for this thesis. Particularly I would like to thank the members of my committee, Dr. Mayne, Dr. Frost, Dr. Rix and Dr. Huber, for their insightful comments and advice.

My coworkers throughout the years at PMRL, namely Marco, Sherie, Junbong, Liang, Seth, Song hun, Junghee, Zhonghao, Qi, Adrian, Lucio, Cesar, Seunghee, Sheng, Minsu, Xingwei and Norimasa taught me many things but most importantly provided a great environment to work in. I would also like to acknowledge the support of the rest of the students in the Geosystems group.

Several people that I met outside of civil engineering also contributed making the Atlanta experience unforgettable. Some of them worth mention are Evan, Irene, Yannis, Spyros, Kostakis, Michael, Tony, George and Michalis and Domenic.

My gratitude should also be extended to my former advisors Ioannis Anastasopoulos and George Gazetas. I appreciate working with them and thank them for introducing me to geotechnical engineering.

The most influential person during the last three years, not just in research but in all aspects of life has been my advisor, Carlos Santamarina. Words cannot describe how much I owe to him. Above all however, he taught me how to dream.

Finally, I would not be writing these words today had it not been for all the support that has been provided by my family over the last 26 years. I need not stretch my words; Margarita, George, Charilaos, Panagiotis and Ioanna: thank you so much!

TABLE OF CONTENTS

LIST OF TABLES

LIST OF FIGURES

SUMMARY

The current economic situation has severely affected the US road infrastructure and funding has become inadequate for either maintenance or future growth.

The inverted base pavement structure is a promising alternative to achieve high quality roads at considerably lower cost than conventional pavements. The proximity of the unbound granular base layer to the tire load makes the response of the granular base critical to the performance of the pavement structure. Therefore extensive material characterization is conducted on the granular materials that make the base. In particular, a true triaxial chamber is developed to study the mechanical response and the stress-dependent stiffness of granular bases compacted at different water contents.

A novel method is developed to assess the as-built stress-dependent anisotropic stiffness of granular bases in-situ using both crosshole and uphole test configurations. The two inverted base pavements built in Georgia at the Morgan County quarry haul road and the Lagrange south Loop are tested as part of this study.

A nonlinear orthotropic constitutive model is selected to capture the deformational behavior of compacted granular bases. The response of the pavement is analyzed by implementing this constitutive behavior in a three-dimensional finite-element model. Different pavement structures are simulated. It is shown that thin asphalt concrete layers resting directly on granular bases deform as membranes.

Finally, numerical simulations are extended to compare inverted base pavements to conventional pavements used in practice. Results highlight the inadequacy of ASSHTO's

structural layer coefficient for the analysis of inverted base pavement structures as well as the potential economic advantages of inverted base pavements.

CHAPTER 1
INTRODUCTION

1.1 Motivation

The United States transportation system is a vast network of roads, railways and airports. The road network is the longest of the three, with 4.19 million kilometers of existing paved roads and a growth rate of approximately 56,000 lane-kilometers each year during the last 10 years (FHWA 2013). In Georgia, the transportation system comprises 124,000 miles of roadway, to support almost 300 million vehicle-miles traveled per day (GDOT 2013).

The annual expenditures in the transportation infrastructure have averaged $40 billion in the last ten years (DOT.gov). Yet, the infrastructure remains in bad condition, as observed by the American Society of Civil Engineers 2013 report (ASCE 2013):

- 42% of urban highways are congested at some time of the day, every day.
- $101 million is wasted on man-hours and fuel every day.
- 32% of American major roads are in poor to mediocre condition.

The implications arising from an ailing infrastructure are evident, both economically and socially. The FHWA estimates that approximately $170 billion in annual investments is required to substantially improve the road infrastructure. Unfortunately, the economic situation in the last few years has discouraged public spending. In this context, new alternatives with lower life-cycle costs would be welcome.

1.2 Scope

The construction of pavement structures is a significant part of annual expenditures. Pavement structures distribute the large traffic loads to the weaker natural soil or subgrade. The two types of pavement structures built in the U.S. are "flexible" asphalt concrete (AC) and "rigid" Portland-cement concrete (PCC) pavements.

Inverted base pavements are an alternative flexible pavement structure used in other countries, such as South Africa. In inverted base pavements the stiffness profile does not decrease monotonically with depth. Inverted base pavements typically involve a thin asphalt concrete AC surface layer laid over a top-quality unbound aggregate base GAB that is compacted on a cement-treated base CTB. The asphalt concrete layer acts as a seal and a riding surface, while the GAB is the main load redistribution course and protects the CTB and the subgrade. The CTB serves as a rigid substrate for improved compaction of the GAB and provides stability for the GAB layer. Inverted base pavements emerge as a viable long-term alternative to conventional pavements for traffics of all magnitudes.

The inverted base pavement's structural capacity relies on the performance of the unbound aggregate base which rests directly below the thin asphalt layer and tire loads. The stress-dependent properties of the granular base and the increased confinement provided by cement-treated base underneath will determine whether the GAB has the strength and stiffness required to withstand very high traffic loads.

The scope of this work is to investigate the potential of inverted base pavements as a reliable and more economical alternative to conventional pavements. To this end an extensive characterization study is first conducted to provide physical understanding on

the performance of the granular base which constitutes a critical component of inverted base pavements.

1.3 Organization

Chapter 2 provides an extensive compilation of documented inverted base pavements in the US and abroad, with emphasis on the reported inverted base pavement response.

Chapter 3 reports a comprehensive laboratory investigation designed to study the stress-dependent response of coarse granular materials such as the GAB. A new true triaxial device is specifically designed and built for this purpose.

Chapter 4 reviews the effects of compaction-related variables, mainly water content, on the stiffness of the GAB and presents the results of a unique experimental study.

Chapter 5 presents the development of two novel testing methods to characterize the stiffness of the GAB in-situ. The two methods were applied to characterize the two inverted base pavements in Georgia.

Chapter 6 proposes a simple constitutive model to characterize the deformational behavior of the granular GAB away from failure. Subsequently, the model is calibrated and implemented in the finite-element code ABAQUS, and a series of numerical simulations are conducted to analyze inverted base pavements.

Chapter 7 identifies inverted base pavements that are equivalent to standard flexible pavement sections regularly used in Georgia.

Chapter 8 summarizes the findings of this project, proposes topics for further study and suggests additional steps towards the implementation of inverted base pavements.

Note: chapters are prepared as self-contained documents. Therefore, there is some repetition between introductory concepts presented in different chapters.

CHAPTER 2
INVERTED BASE PAVEMENTS: CONSTRUCTION & PERFORMANCE

2.1 Introduction

Inverted base pavements are flexible pavement structures where the aggregate base is placed between a cement-treated base and a thin (usually <100mm) asphalt concrete surface layer. Inverted base pavements can reduce the dependency of pavement construction on asphalt while at the same time provide a high quality pavement for all traffic levels by utilizing the granular base as a key structural element (Tutumluer 2013). Differences in structural characteristics between conventional flexible pavements and inverted base pavements are captured in **figure 2.1**.

Inverted base pavements are extensively used in South Africa to support heavy traffic loads; the French design guide also recommends inverted base pavements to prevent reflective cracking between cohesive layers (Corté and Goux 1996). FHWA representatives visited South Africa in 1995 and assessed first-hand the potential of inverted base pavements (Horne et al. 1997). Still, recorded construction experience and performance data on inverted base pavements in the US remain scarce. This chapter reviews documented case histories, starting with the extensive South African experience and includes past and recent case histories in the US.

2.2 Case Histories

Available studies and case histories are briefly described next. Performance information follows in subsequent sections.

2.2.1 South Africa – Heavy Vehicle Simulator

Inverted base pavement developed in South Africa as a cost-effective alternative to concrete pavements. Design faced early scrutiny as it was believed that they could not match the performance of full depth asphalt or concrete pavements. Improvements in aggregate base technology and extensive case histories eventually contributed to the establishment of inverted base pavements as the primary design for high-traffic roads. (Freeme et al. 1980). Accelerated pavement testing (APT) facilities such as the Heavy Vehicle Simulator played a critical role in the development of inverted base pavements and integration into design guidelines. (Du Plessis et al. 2006; Freeme et al. 1982; Theyse et al. 2011). Several inverted base pavements have been tested using the Heavy Vehicle Simulator (**Table 2.1**). Unfortunately, most Heavy Vehicle Simulator reports are not publicly available.

2.2.2 United States Experience

All reported US inverted base pavement case histories are summarized in **Table 2.2** (See also NCHRP Synthesis by Tutumluer 2013). The first reported case of inverted base pavement was the rehabilitation of rigid pavements in New Mexico in 1954. Two inverted pavement sections were also constructed at the I-010-1 Road Forks-East project while in the Project F-51-8 near Santa Fe, NM inverted base designs were tested to address unstable micaceous soils in the subgrade (Johnson 1961). In the 1970s The US

Army Corps of Engineers tested two quasi-inverted base pavements by stabilizing the upper 38cm (15") of a clay subgrade using lime and cement (Ahlvin et al. 1971; Barker et al. 1973; Grau 1973).

In the 1980s, two inverted base designs were tested at Georgia Tech as part of an extensive laboratory study (Barksdale 1984; Barksdale and Todres 1983). Measurements were later used to calibrate a nonlinear finite-element code (Tutumluer and Barksdale 1995). More recently, inverted base pavements were tested in Louisiana under both field and accelerated pavement testing conditions in an effort to reduce reflective cracking occurring in full depth soil-cement pavements (Metcalf et al. 1999; Rasoulian et al. 2000; Titi et al. 2003).

Two experimental inverted base pavement sections have been constructed in Georgia in the last 15 years, one in the Morgan county quarry and the other at the South Lagrange Loop (Cortes 2010; Terrell et al. 2003). The documented construction of the Lagrange project shows that no special equipment is required for construction of inverted base pavements. Another inverted base pavement has been constructed at Bull Run, VA; no data have yet been published on the latter. Currently, state DOTs in Tennessee and New Mexico are considering inverted base pavement test projects (Buchanan 2010; Tutumluer 2013).

2.3 Inverted Base Pavement Construction

2.3.1 Compaction Techniques

Earlier pavements in South Africa were built with granular bases made of natural gravel and various forms of Macadam (Jooste and Sampson 2005). The structural

requirements from the granular base increased when the application of inverted base pavements was extended to high-volume roads. Crushed stone bases became the norm as an unbound aggregate material and the slushing technique was developed to achieve a high density and stable base, called G1.

Slushing is applied to a granular base following compaction with standard vibratory rollers at optimum moisture content. The base is flooded and compacted using static rollers; segregated fines that appear at the top of the base are washed away. This procedure forms a tightly interlocked matrix of coarse aggregates (details in Kleyn 2012). The density increase due to slushing can reach 3-4% (Jooste and Sampson 2005). Contrary to the South African experience, application of the slushing technique in the inverted base pavement in Morgan county, GA did not result in any significant improvement in either density or stiffness (Terrell et al. 2003). Nevertheless, both inverted base trial sections exhibited very high density which was attributed to the rigid support offered by the CTB during compaction.

2.3.2 Aggregate Quality

Figure 2.2 compares South African specifications for aggregates used in unbound bases to GDoT and CALTRANS specifications. South African specifications impose strict guidelines on particle origin, shape and fines plasticity (Kleyn 2012; Theyse 2002). Note that the expected density is expressed as a fraction of the density of the solid particle rather than relative to Proctor density. The base gradation follows the Fuller curve to maximize attainable density with the upper and lower bounds based on strength demands and constructability issues.

2.4 Inverted Base Pavement Performance

The performance of inverted base pavement structures presented above is reported in **tables 4.3** through **4.7**. Findings related to deformation, cracking and granular base stiffness are discussed below.

2.4.1 Rutting and Deflection

Deformation measured one year after construction of the I-010-1 Road Folks-East project was larger for the inverted base pavements than the conventional designs (Johnson 1961). Measurements for the F-051-1 project in Santa Fe showed that inverted base pavement outperformed conventional flexible pavements (**Table 2.3**). Deflection measurements in the US Army Corps of Engineers study showed similar results for both inverted base pavements and conventional pavements (**Table 2.4**, Barker et al 1973). In the Georgia Tech project, the inverted base pavements experienced relatively low deformation which was concentrated mainly in the asphalt base (**Table 2.5**, Barksdale and Todres 1983). Both the inverted base pavement and the full depth soil-cement sections in the Louisiana field study exhibited similar rutting (**Table 2.6**). Rutting observed in the Morgan County project five years after construction was insignificant for the inverted base sections, but greater than 25mm in the conventional section (**Table 2.7**).

In the Morgan county study, Falling Weight Deflectometer tests conducted 8 years after construction were used to calculate pavement life (Lewis et al. 2012). Inverted base pavements clearly exhibited better performance (**Table 2.7**).

2.4.2 Surface Cracking

No sign of cracking was observed in the New Mexico inverted base sections after one year contrary to some conventional pavements (Johnson 1961). The use of cement instead of asphalt for the inverted base pavements in the Georgia Tech study proved more effective in reducing tensile strain in the asphalt surface (**Table 2.5**, Barksdale and Todres 1983). The inverted base section in the Louisiana field project exhibited much less cracking compared to the full-depth soil-cement pavement (**Table 2.6**, Titi et al 2003). Visual inspection during the Morgan county project revealed no cracks in the inverted base section while cracks were present in the conventional section, particularly where trucks decelerated near the quarry gate (Lewis et al. 2012).

Monitoring of the integrity of the CTB during the Lagrange project showed that it was able to withstand the compaction process without cracking (Cortes and Santamarina 2013).

2.4.3 Aggregate Base Stiffness

Figure 2.3 shows back-calculated resilient modulus data gathered during several Heavy Vehicle Simulator tests (Maree et al. 1981; Theyse 2002). G1 and G2 crushed stone bases develop higher stiffness for the same stress than natural gravel bases. The increased confinement offered by the cement-treated base in inverted base pavements is also demonstrated as the same external load leads to higher confinement within the granular base (**figure 2.3**). During the Morgan County project wave propagation was used to measure the stiffness of the granular base in the pavements tested (Terrell et al. 2003). The traditional section displayed higher stiffness than the two inverted sections (**table 2.7**). The vertical stiffness was higher than the horizontal both in the loaded and

unloaded cases (Terrell et al. 2003). Dynaflect (LWD) measurements were used to back-calculate the resilient modulus of the subgrade in the Louisiana project (Titi et al. 2003). Both pavements showed similar values ranging from approximately 60MPa to 170MPa. On average resilient modulus decreased with the number of passes, a possible indication of ongoing gradual deterioration.

The strain level associated with the measurement must be taken into consideration when reviewing stiffness measurements. Large-strain measurements (HVS) reflect an equivalent secant modulus for that level of strain. On the contrary, wave propagation techniques provide the modulus at very small strains. The Dynaflect modulus is derived from a back-calculation algorithm at intermediate strain levels.

2.5 Economic Comparisons

South African studies during the 1980s concluded that inverted base pavements are the most economic option for all traffic levels (Freeme et al. 1980; Mitchell and Walker 1985). More recent studies conducted in South Africa (**Figure 2.4**) as well as in the US (**Figure 2.5**) agree that inverted base pavements can be more economical both in terms of construction as well as lifecycle costs (Cortes 2010; Jooste and Sampson 2005; Weingart 2009). Finally, Titi et al. (2003) state that although the inverted base design analyzed is 20% more costly than the conventional full-depth soil-cement section, given the increased life expectancy (4 times longer according to accelerated pavement testing or 2 times longer according to in-situ performance data analysis) the added cost is justifiable (Metcalf et al. 1999).

2.6 Discussion

The structural capacity of inverted base pavements cannot be captured by empirical design guidelines such as the Structural Number concept. In the Louisiana study the estimated structural number was higher for the inverted base pavement (**table 2.6**) even though the design SN was identical (Kinchen and Temple 1980; Rasoulian et al. 2000). **Figure 2.6** shows inverted base pavements outperforming all conventional pavements in Louisiana and in the Georgia Tech studies. South Africa employs a mechanistic pavement design process for the last 20 years and the use of inverted base pavements has been widespread (TRH 1996).

Results highlight the synergy between the compacted granular base and the cement-treated base. The CTB is stiff and can effectively redistribute loads but cracks in tension under high loads and reflective cracking can affect the asphalt layers (**table 2.6**). On the other hand, the granular base stiffness is inherently stress-dependent and the rigid CTB substrate contributes to lateral confinement (**figure 2.3**). Furthermore, the presence of a cemented substrate provides a stiff foundation support that prevents bending beneath rollers and promotes volume contraction of the granular base during compaction.

The quality of the granular base emerges as the most critical factor in the performance of inverted base pavements. Granular bases with non-plastic fines perform better in all studies reported in t**able 2.3**, while crushed-stone bases develop higher stiffness than gravel (**figure 2.3**). Furthermore, the high-quality G1 base used in inverted base pavements in South Africa has performed very well even under when wet (Jooste and Sampson 2005). The superior performance of crushed stone is corroborated with laboratory studies and is in agreement with South African design guidelines (Bilodeau

and Doré 2012; Cunningham et al. 2012; Ekblad and Isacsson 2006; Ekblad and Isacsson 2008).

2.7 Summary of Findings

This study synthesized reported construction and performance findings on inverted base pavements. While available data are scarce, few robust trends begin to emerge:

- Inverted base pavements can be constructed using conventional techniques.
- Very high densities can be attained in the granular base when compacting on a cement-treated base. In fact, compaction density is best specified as a percentage of apparent solid density rather than Proctor density.
- In most case studies, inverted base pavements outperformed their conventional counterparts.
- Reflective cracking is greatly reduced when a granular base sits between the CTB and asphalt layers.
- Inverted base pavements can be economically advantageous from both a construction cost and life-cycle cost perspective.

On the other hand, several questions remain unanswered. In particular, the following topics need further investigation:

- The role of slushing remains unclear. Apparently slushing leads to the removal of excess fines and prompts the development of an interlocked structure. In this case, a minor increase in density may have a profound effect on stability, dilatancy and strength.

- Studies need to be extended to inverted base pavement designs under different conditions and for various traffic levels.
- Data are lacking with respect to the degradation of the CTB during compaction or traffic loading as well as the performance of very thin asphalt layers (<50mm).

Table 2.1. Inverted base pavements tested by the Heavy Vehicle Simulator (Data and original references in Theyse 2002, and Jooste and Sampson, 2005).

Location	Year	Layer thickness from top to bottom [mm]
S12 Cloverdene C17	1978	Gap-graded asphalt [70] G1 [320] Lightly cemented subbase [280] Natural gravel [100]
P157/1 Olifantsfontein	1980	Semi-gap asphalt [30] G2 [200] Lightly cemented subbase [100] Natural gravel [200]
P157/2 Jan Smuts	1980	Semi-gap asphalt [35] G1 [140] Cemented gravel [255] Natural gravel [125]
N3, Mooi River, Kwazulu-Natal	1982	Gap-graded asphalt [50] G1 [200] Lime stabilized subbase [155]
TR86, Macleantown, Eastern Cape (303A2)	1986	Asphalt [40] G2 [150] Drainage layer [150] C4 [200] C5 [140] G6 subgrade
N2-23 Umkomaas, KawZulu-Natal (327A3)	1988	Asphalt [80] G1 [160] C3 [140] C4 [120]
Road 2388, Cullinan, Gauteng (398A4)	1997	Asphalt [30] G3 [100] C3 [150]

Note: G: granular base/subbase C: cemented subbase. Lower number denotes higher quality.

Table 2.2. Inverted base pavement case histories in the US.

Location	Year	Layer thickness from top to bottom [mm]		Reference
I-010-1 Road Forks-East Mexico	1960	AC [38] UAB [152] CTB [152]	AC [76] UAB [152] CTB [152]	Johnson, 1961
F-51-1Santa Fe New Mexico	1960	AC [76] UAB [152] CTB [152]		Johnson, 1961
US Army Corps Vicksburg, MS	1971	AC [76] UAB [152] Stabilized clay subbase [381]		Ahlvin et al. 1971 Barker et al. 1973
Georgia Tech Atlanta, GA	1980	AC [89] UAB [203] CTB [152]		Barksdale 1984 Barksdale and Todres 1983
Louisiana	1991	AC [89] UAB [102] Soil-cement [152]		Metcalf et al. 1999 Rasoulian et al. 2000 Titi et al. 2003
Morgan County, GA	1999	AC [76] UAB [152] CTB [203] Filler [51] Prepared subgrade (CBR 15)		Lewis et al. 2012 Terrell et al. 2003
Lagrange, GA	2008	AC [89] UAB [152] CTB [254] Stabilized subgrade [152]		Cortes 2010
Bull Run, VA	2010	AC [127] UAB [152] CTB [254] prepared subgrade		Weingart, 2010

Note: AC: asphalt concrete, GAB: graded aggregate base, CTB: cement-treated base

Table 2.3. Benkelman beam deflection measurements for different pavement sections on the I-010-1 Road project and the F-051-8 project (Johnson, 1961).

I-010-1			F-51-8		
	Layer thickness [mm]	Deflection [mm]		Layer thickness [mm]	Deflection [mm]
Inverted base pavements	AC [38] UAB 3-6 PI [152] CTB [152] Untreated subbase [89]	0.43	Inverted base pavements	AC [76] UAB non-plastic [152] CTB 4% [152]	0.36
	AC [76] UAB non-plastic [152] CTB [152] Untreated subbase [229]	0.41		AC [76] UAB PI:3-6 [152] CTB 4% [152]	0.48
				AC [76] UAB non-plastic [152] Asphalt-treated base [152]	0.43
Conventional Pavements	AC [76] CTB 1.5% [152] Untreated subbase [178]	0.28		AC [76] UAB PI:3-6 [152] Asphalt-treated base [152]	0.46
	AC [76] CTB 1.5% [152] Untreated subbase [356]	0.38	Conventional Pavements	AC [76] UAB non-plastic [152] Subbase [254]	0.61
	AC [76] UAB non-plastic [152] Untreated subbase [356]	0.46		AC [76] UAB PI:3-6 [152] Subbase [254]	0.61
	AC [76] CTB 3% [152] Untreated subbase [356]	0.25		AC [76] Asphalt-treated base [152] Subbase [254]	0.43
	AC [76] CTB 3% [152] Untreated subbase [178]	0.28		AC [76] CTB 4% [152] Subbase [254]	0.38
	AC [76] CTB 3% [152] UAB non-plastic [152]	0.48		AC [76] CTB 2% [152] Subbase [254]	0.43

Note: AC: asphalt concrete; UAB: unbound aggregate base; CTB: cement-treated base.

Table 2.4. Performance data for the US Army Corps of Engineers study in Vicksburg, Mississippi (Barker et al 1973).

Layer thickness [mm]	**load assembly**			
	1600kN 12 wheel assembly			135kN single wheel
	Surface deflection [mm]	**Subgrade vertical stress [kPa]**	**Load applications to failure**	**UAB vertical strain [microns]**
Asphalt concrete [76] Crushed stone base [152] Cement-treated clay [381]	0.53	131	198	1800
Asphalt concrete [76] Crushed stone base [152] Lime-treated clay [381]	0.61	124	1871	800
Asphalt concrete [76] Crushed stone base [533]	0.58	172	5,037	900
Asphalt concrete [76] Cement-treated clayey gravely sand [533]	0.56	55	10,406	-

Table 2.5. Perfomance data on the Georgia Tech laboratory study (Barksdale and Todres 1984, Tutumluer and Barksdale 1995).

Layer thickness [mm]	Fail mode	Reps to failure [thousands]	Rutting [mm]	AC strain [microns]	Subgrade strain [microns]	Base strain [microns]
AC [89] UAB [305]	F/R	3000	12.7	465	170	-
AC [89] UAB [203]	R	1000	25	674	1310	2130
AC [229]	R	130	25	319	1380	-
AC [165]	R	440	25	460	1500	-
AC [178]	R	150	29.5	410	2200	-
AC [89] UAB [203]	R	550	15	300	1850	110
AC [89] UAB [203]	F	2400	7.1	280	1750	340
AC [89] UAB [203]	F	2900	8.6	390	2500	400
AC [89] UAB [203] Soil-cement[152]	F/R	3600	12.7	340	390	370
AC [89] UAB [203] CTB [152]	F/R	4400	11.2	260	340	420

Note: F: fatigue cracking failure, R: rutting failure.

Table 2.6. Performance data on the Louisiana field test study (Titi et al. 2003).

	Inverted Base Pavement		**Full-depth soil-cement pavement**	
Layer thickness [mm]	Asphalt concrete [89] Crushed limestone [102] Soil-cement [152]		Asphalt concrete [89] Soil-cement [165]	
Average rut [mm]	3.8		3.3	
Cracking length [m]	Total: Low severity: Medium severity: High severity:	118 95 24 0	Total: Low severity: Medium severity: High severity:	233 152 64 17
Average SN	5.57		4.69	
Serviceability Index	4.2		4.0	
International Roughness Index	1.03 mm/m		1.25 mm/m	
Final subgrade resilient modulus	103.4 MPa		103.4 MPa	

Note: Structural number and Resilient modulus were estimated through Dynaflect measurements (Kinchen & Temple 1980). Reported figures are at the end of the 10.2 year monitoring period.

Table 2.7. Performance of pavement sections in the Morgan country quarry study (Terrell et al 2002, Lewis, 2012).

Layer thickness [mm]	max rut [mm]	Cracking	Max FWD Deflections [mm]	Remaining Life	E_{hor} [MPa]
AC [76] GAB [152] (Slushing) CTB [203]	9.525	No cracking	0.28	94.61%	250
AC [76] GAB [152] CTB [203]	minimal	No cracking	0.25	99.34%	550
AC [76] 203 GAB SS [152]	>25	Extensive	2.03	67.92%	650

Note: AC: asphalt concrete, GAB: graded aggregate base, CTB: cement-treated base, SS: surge stone.
Remaining life was calculated through FWD measurements.
Horizontal Young's modulus E_{hor} measured for a horizontal stress of 100kPa.

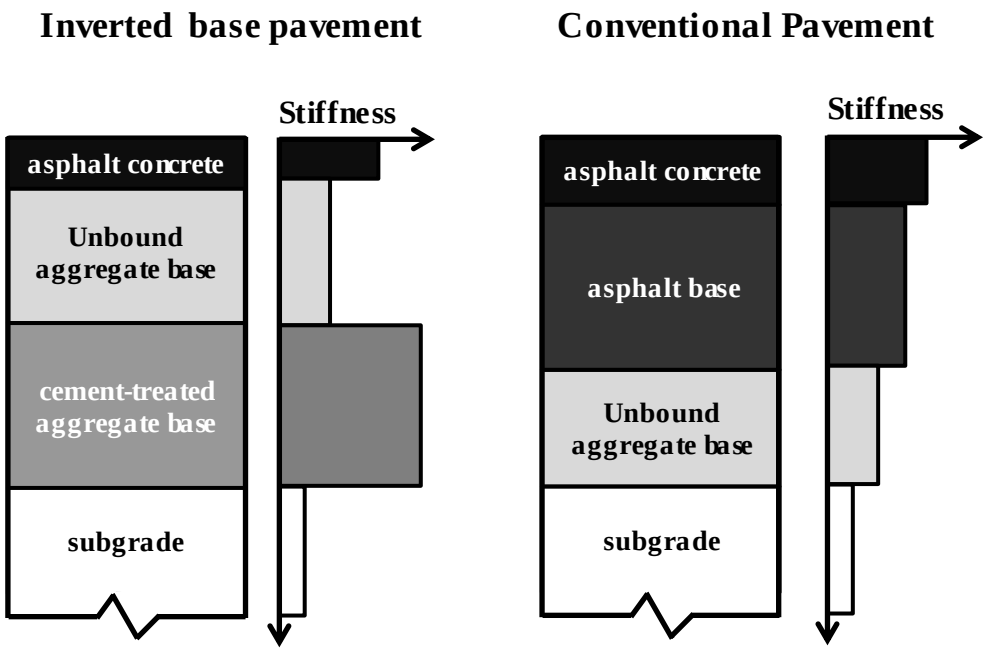

Figure 2.1. Schematic comparison between an inverted base pavement and a conventional asphalt pavement.

(a)

	South Africa G1 base	CALTRANS base	GDoT GAB
Fines	LL<25%, PI<4	Sand Equivalent <21	Sand Equivalent <20
Shape	flackiness (sphericity) <35%	N/A	Elongated particles <10%
Density	86-88% of apparent solid density	95% of CTM 231	98% mod. Proctor

(b)

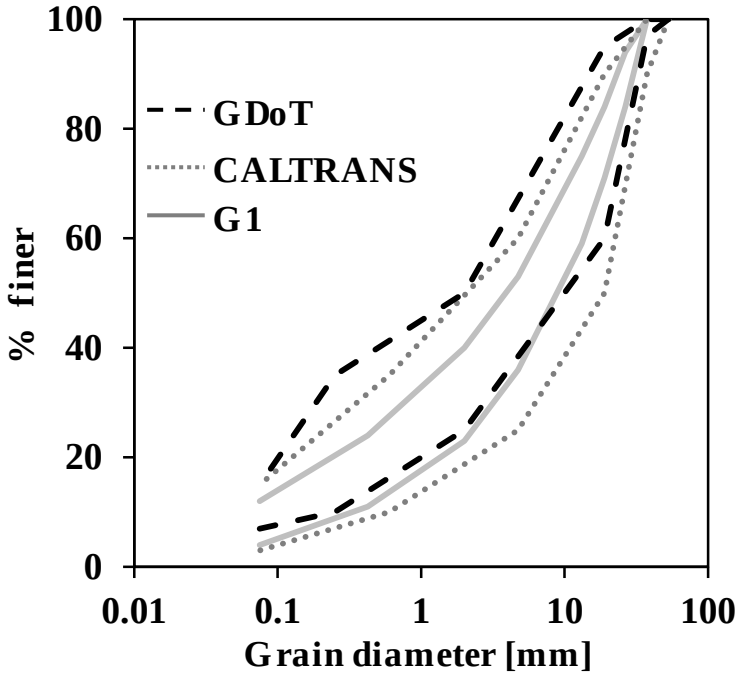

Figure 2.2. Granular base specifications: (a) aggregate specifications and (b) gradation requirements for granular bases in the South African, CALTRANS and GDoT design guidelines.

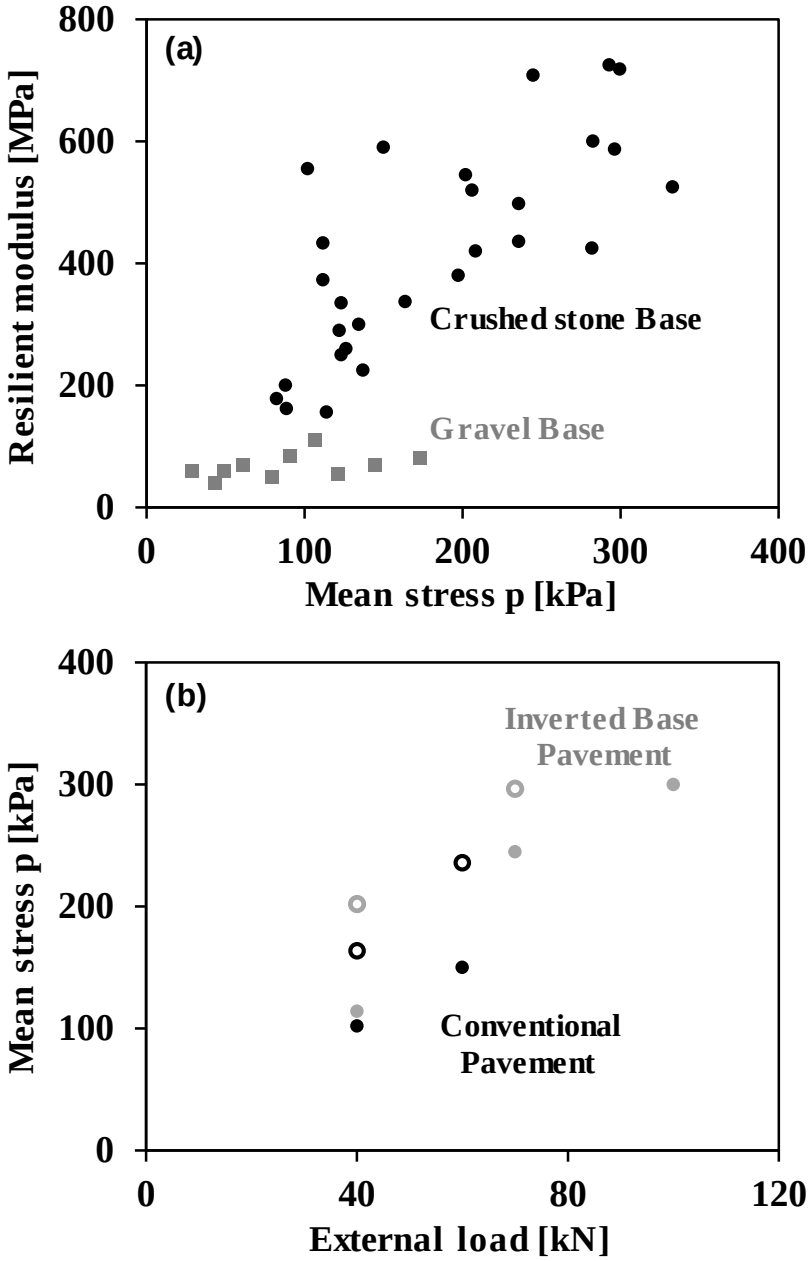

Figure 2.3. Inverted base pavement response: (a) Resilient modulus versus mean stress $p=(\sigma_1+\sigma_2+\sigma_3)/3$ for G1/G2 crushed stone base and G5 gravel base and (b) Mean stress for a given externally applied load for both inverted base pavements and conventional pavements.

Note: Hollow circles correspond to values at the bottom of the base, while filled circles correspond to values at the top of the base. Data from Theyse (2002).

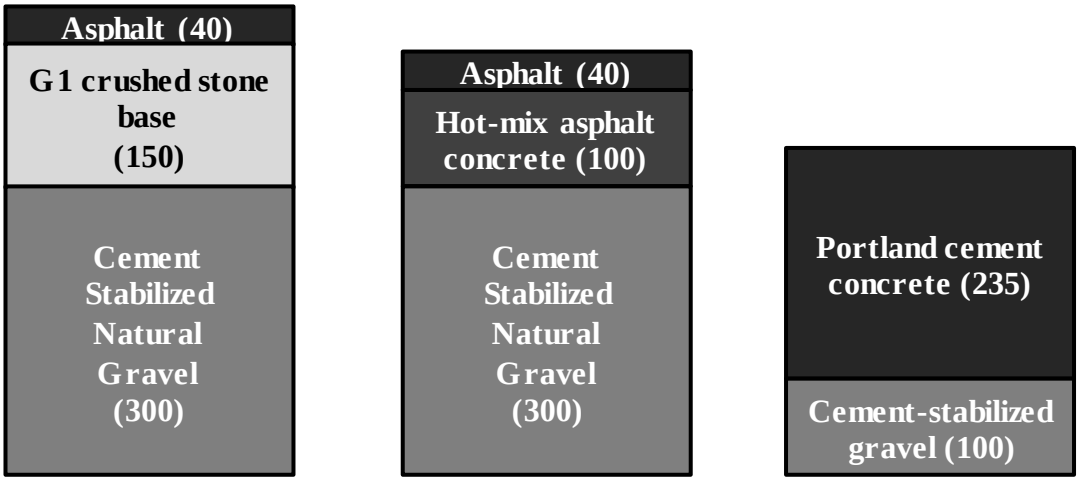

Structural number: 4.23	**Structural number: 4.88**	**Structural number: -**
Present cost (discount rate)	**Present cost (discount rate)**	**Present cost (discount rate)**
26.2 Rand/m^2 (4%)	**36.4 Rand/m^2 (4%)**	**32.5 Rand/m^2 (4%)**
21.3 Rand/m^2 (8%)	**31.5 Rand/m^2 (8%)**	**31.0 Rand/m^2 (8%)**
21.8 Rand/m^2 (12%)	**28.9 Rand/m^2 (12%)**	**30.3 Rand/m^2 (12%)**

Figure 2.4. Illustration of pavements included in the economic comparison by Mitchell and Walker (1985). Layer thickness in mm shown in parentheses.

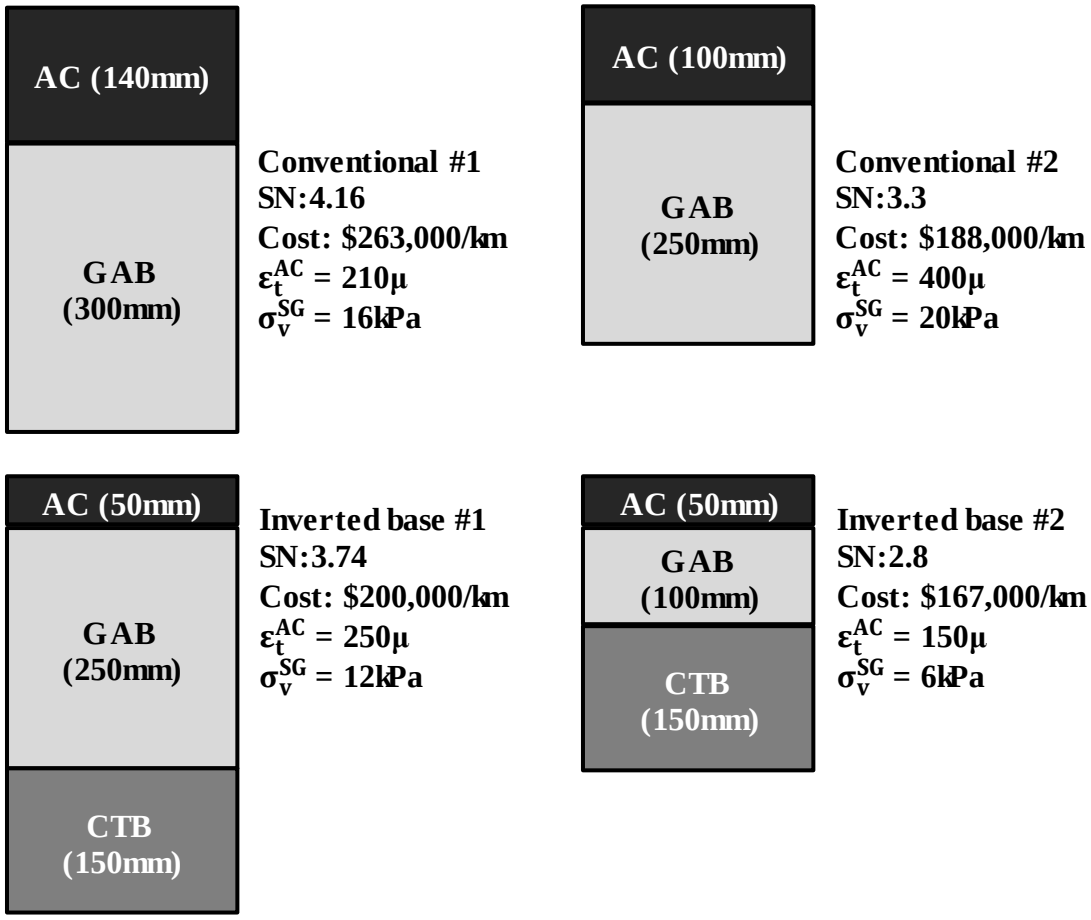

Figure 2.5. Illustration of pavements structures included in the economic comparison by Cortes (2010).
Note: AC: asphalt concrete, GAB: graded aggeregate base, CTB: cement-treated base. ε_t^{AC}: AC tensile strain, σ_v^{SG}: subgrade vertical stress
Structural number SN calculated base on GDoT Specifications.

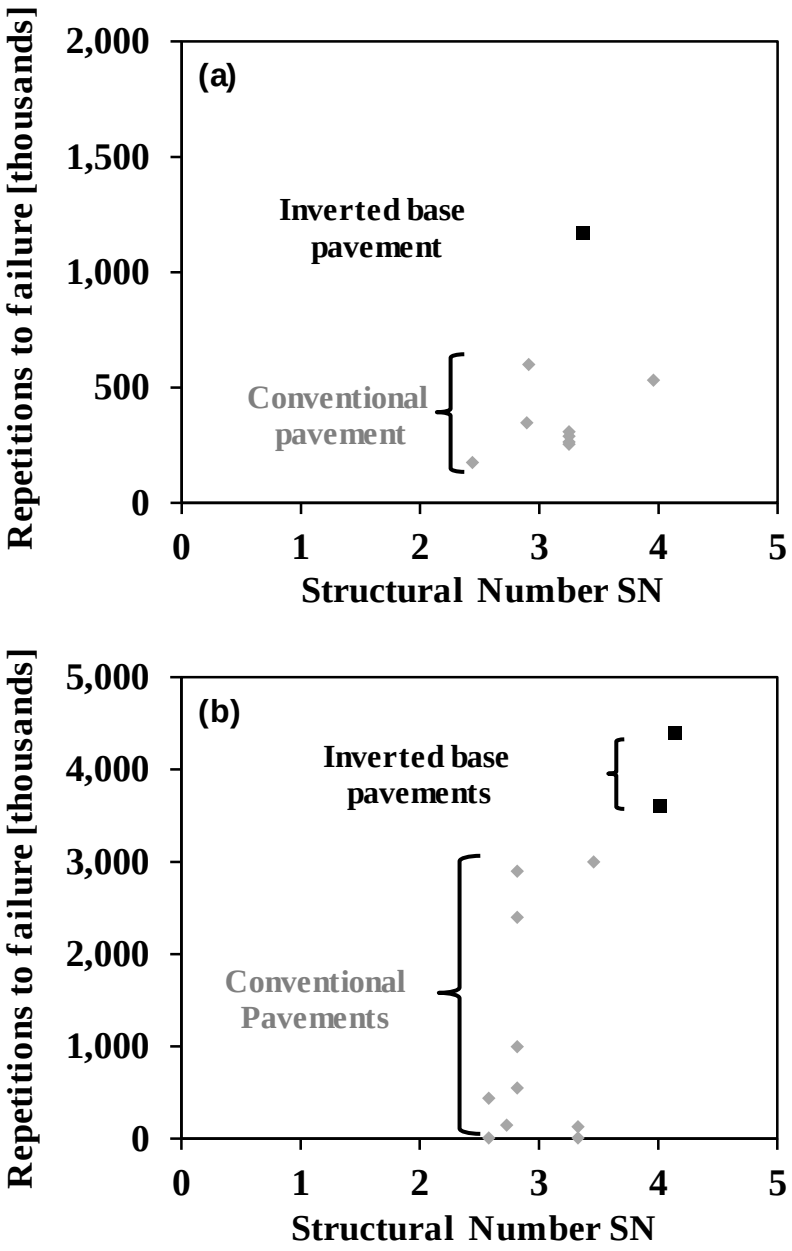

Figure 2.6. Load applications to failure as a function of structural number SN for (a) the Louisiana full-scale accelerated pavement testing study (Metcalf et all 1999) and (b) the Georgia Tech laboratory study (Barksdale and Todres 1984). **Note:** SN calculated using GDoT specifications.

CHAPTER 3
LABORATORY DETERMINATION OF ANISOTROPIC GRANULAR BASE STIFFNESS UNDER TRUE TRIAXIAL STRESS

3.1 Introduction

Flexible pavements typically include one or more unbound granular layers. Unbound granular layers are particularly important in inverted base pavements where they are placed beneath a thin asphalt layer directly below the load. The mechanical properties of granular bases are key design inputs in both empirical pavement design methods as well as in mechanistic guidelines (AASHTO 1993; NCHRP 2004; TRH 1996). Granular bases exhibit non-linear, anisotropic, post-peak softening behavior, yet design guidelines are based on the simplest assumptions (Clayton 2011; Dawson et al. 2000).

Previous studies have demonstrated the implications of anisotropy in stress and deformation fields (Barden 1963; Tutumluer 1995; Tutumluer and Thompson 1997). Nevertheless, robust characterization of the true anisotropy of unbound granular materials is lacking while most studies have neglected the combined presence of inherent and stress-induced anisotropy (Adu-Osei et al. 2001; Rowshanzamir 1997; Tutumluer and Seyhan 1999).

A true triaxial apparatus was designed and built to study the complex behavior of unbound granular bases. The three principal stresses can vary independently to impose any arbitrary state of stress and stress path on a cubical specimen. This chapter reviews

previous studies on unbound aggregate material, documents the design and manufacturing of the true triaxial device and presents a comprehensive dataset.

3.2 Previous Studies

Granular materials under repetitive loading accumulate plastic strain (Lekarp and Dawson 1998; Pasten et al. 2013; Uzan 2004). The plastic strain per cycle is small and difficult to measure for typical pavement applications. After a large number of load cycles, it is assumed that the material behaves quasi-elastically. This condition is called resilient response (shakedown). The elastic strain during one cycle of loading is correlated with the accumulated plastic strains over many repetitions. Therefore it is possible to conduct elastic analyses of pavements using the resilient modulus to predict their long-term performance (Monismith 2004).

3.2.1 Resilient Modulus

The resilient modulus M_r is the ratio of applied vertical stress over the recoverable axial strain under constant radial stress; it is equivalent to Young's modulus in linear elasticity. The resilient modulus M_r is used for the determination of the structural capacity of a subgrade, as well as the structural coefficient of unbound granular bases and subbases (AASHTO 1993). Mechanistic pavement design models account for granular base stiffness using the resilient modulus (NCHRP 2004; TRH 1996).

The test protocol used to determine the resilient modulus was first developed by the Strategic Highway Research Program in the 1980's; the current standard is the AASHTO T-307 (NCHRP 2004). In the past, the stiffness of unbound aggregates has been studied in cyclic triaxial tests (McVay and Taesiri 1985; Uzan 1999), resonant column and

torsional shear tests (Kim et al. 1997). The applicability of laboratory values to in situ conditions is questionable (Maree et al. 1981; Puppala 2008). Resilient moduli tests augmented with bender elements have shown that the ratio between resilient modulus and small-strain Young's modulus is in the order of 0.6 ±0.2 (Davich et al. 2004).

Many studies have focused on the anisotropic properties of granular bases (Adu-Osei et al. 2001; Rowshanzamir 1997; Tutumluer and Thompson 1997). Results show that granular bases are anisotropic due to inherent conditions related to compaction as well as due to the anisotropic state of stress (Majmudar and Behringer 2005; Oda et al. 1985). P-wave measurements in 3D can be used to explore stiffness anisotropy (Kopperman et al. 1982, Cortes 2010).

The resilient modulus and small-strain stiffness of granular materials also depends on stress history, state of stress, density, gradation and water content (Uzan 1985). The effect of deviatoric stress on modulus remains unclear (Morgan 1966).

3.2.2 True Triaxial Tests

The intermediate principal stress σ_2 affects both the strength and shear stiffness of granular materials (Bishop and Wesley 1975; Matsuoka and Nakai 1974). True triaxial devices are used to assess the effect of the intermediate principal stress (Abelev and Lade 2003; Alshibli and Williams 2005; Choi et al. 2008; Hambly 1969; Ismail et al. 2005; Kjellman 1936; Lade and Duncan 1973; Li and Puri 2003; Rowshanzamir 1997). Common difficulties with true triaxial tests include edge effects, which occur when faces interfere with each other, as well as the development of friction along the loading faces. Flexible membranes and lubrication can reduce boundary effects.

3.3 True Triaxial Chamber Design

A true triaxial device was specifically designed for the characterization of unbound granular bases. Design criteria sough a simple yet robust device that avoids common problems associated with triaxial testing. The testing chamber is composed of a set of six stainless steel loading plates (**figure 3.1a**). Each plate is attached to a high pressure hydraulic cylinder capable of applying up to 5 tons of force, except for the base, which is fixed. The cylinders on the horizontal plane react against a rigid stainless steel frame and the top cylinder against the upper reaction plate that is connected to the bottom plate via a set of rods to create a self-reacting system. Numerical simulations were conducted using COMSOL to determine the maximum induced stresses, strains and displacements in all chamber components (**Figure 3.2)**.

The specimen is compacted inside the chamber to reduce disturbance. A vibratory hammer is used to compact the specimen in 4 layers. Rigid stabilizing braces fix adjacent loading plates together during compaction and are detached before loading begins.

The coarse gradation and high stiffness of granular bases permit leaving a considerable gap between the loading plates. The gap is wider that the anticipated deformation, but small enough to prevent material loss. A custom-made latex membrane is placed around the specimen to prevent fines loss. The loading plates are lubricated to minimize friction.

The testing chamber accommodates 100mm cubic specimens. Aggregates above 19mm (¾") are removed from the specimen to reduce scaling effects and are replaced with the same mass of coarse particles within the size tolerance i.e. scalping and replacement. This can lead to a reduction in stiffness (Donaghe and Townsend 1976);

however the overall portion of material that was substituted is very small and therefore changes should be minor.

The device is instrumented with three sets of piezocrystals to emit and receive P-waves. Signals are preamplified, captured and stored using a digital storage oscilloscope. The five hydraulic cylinders are operated in pairs and monitored using pressure transducers. LVDTs are mounted on the reaction frame to monitor the displacement of loading plates. Peripheral electronics are shown in **figure 3.1b**

Wave propagation through coarse-grained granular materials must be carefully designed to balance competing constraints. In particular:

- The travel length s must be much larger than the particle size to adopt an equivalent continuum analysis; we targeted $s/D_{90}>10$ where D_{90} is the particle diameter for the 90% percentile by mass.
- The wavelength λ must be larger than the median grain size D_{50}, $\lambda/D_{50}>2$ to minimize internal Brillouin filtering.
- The travel length s must be longer than the wave length λ, $s/\lambda>4$ to minimize "near field" effects.

The chamber dimensions were selected in order to best satisfy the above contradicting constrains.

The small-strain constrained modulus M_{max} can be inferred from using the measured P-wave velocity V_p and the following equation:

$$M_{max} = \rho \cdot V_p{}^2 \qquad (1)$$

where ρ is the material density.

3.4 Experimental Results

3.4.1 Material and Test Procedure

The granular material tested in this study is GAB from the Griffin quarry in Georgia. The gradation of the specimen falls within the GDoT limits for GAB material (**figure3.3**). Stabilizing braces are bolted to the lateral loading plates to form a rigid box before compaction. Then, the GAB material is placed in the chamber and compacted in 5 lifts using a vibratory hammer. After compaction, the specimen is subjected to a preconditioning vertical stress of 650kPa for 200 cycles. Once preconditioning is completed braces are unfastened and the actual test sequence commences.

Five identical specimens are prepared and tested. Results presented next show the effects of stress, stress anisotropy and inherent fabric anisotropy. Tests are conducted under constant stress ratios $\frac{\sigma_z}{\sigma_y}$ = 1, 2.5, 5 and 10, and in increasing order of stress ratio to minimize sample disturbance (**figure 3.4**).

A typical cascade of signals recorded at the receiver is displayed in **figure 3.5**. The travel time reduces as the applied stress increases indicating the stress sensitivity of P-wave velocity.

3.4.2 Effect of Fabric Anisotropy

During specimen preparation and compaction elongated particles tend to align with the large dimension parallel to the horizontal direction causing inherent anisotropy (Cortes and Santamarina 2013). The effect of fabric anisotropy on stiffness is quantified with P-wave velocity measurements conducted under isotropic stress conditions. **Figure 3.6a** shows the effect of fabric anisotropy in the tested GAB. Vertical velocity is higher

than horizontal velocity at all stress levels. **Figure 3.6b** shows the ratio of small-strain constrained modulus M_{max} in the vertical and horizontal direction calculated with equation (1). The average of the results from the two horizontal directions is used. For most stress levels the anisotropy is around 1.3.

3.4.3 Stress Sensitivity

Figure 3.7 displays the effect of stress on P-wave velocity. Results are plotted against different stress variables to identify the governing parameters.

The mean stress $p = (\sigma_1 + \sigma_2 + \sigma_3)/3$ and the deviatoric stress q are used to describe the stress sensitivity of the resilient modulus M_r (Uzan 1985):

$$M_r = k_1 \cdot p^{k_2} \cdot q^{k_3} \quad (2)$$

Results in **figures 3.7a** and **3.7c** show that the deviatoric stress and mean pressure cannot describe the evolution of stiffness. Measured $V_p$values plotted versus the normal stress in the direction of wave propagation collapse onto a single curve for all levels of stress anisotropy (**figure 3.7b** and **3.7d**; see also Kopperman et al. 1982, Roesler 1979, Stokoe et al. 1985). The dependency of the longitudinal stiffness primarily on the normal stress in the same direction underlies the evolution of stress-induced anisotropy in granular materials (Oda et al. 1985). Hence, stiffness cannot be accurately modeled with a cross-anisotropic formulation.

The true triaxial apparatus allows independent control of the intermediate principal stress σ_2. This capability allows the verification of the above findings for different loading patterns. **Figure 3.8** shows P-wave velocity data plotted against normal stress for three extreme conditions: isotropic compression, triaxial compression-loading (TX) and triaxial extension loading (TE). Measurements gathered in both the horizontal (x) and

vertical (z) directions are shown. Again, longitudinal stiffness is controlled by the normal stress in that direction, and P-wave velocity exhibits only minor sensitivity to transverse loads. Small discrepancies appear at high stress ratios as the material approaches failure, possibly due to extensive particle rearrangement.

3.5 Large Strain Behavior of GAB

Stress-strain data gathered during triaxial compression loading are plotted in hyperbolic coordinates in **figure 3.9a**. The fitted hyperbolic model allows the calculation of the tangent Young's modulus $E_{tangent}$ along the stresss-strain curve. Using small-strain measurements from the same test the small-strain Young's modulus E_{max} is related to constrained modulus according to theory of elasticity:

$$E_{max} = M_{max} \cdot \frac{(1+\nu)\cdot(1-2\nu)}{(1-\nu)} \tag{3}$$

where ν is Poisson's ratio. In the small-strain regime, $\nu \approx 0.1$ and therefore $E_{max} \approx M_{max}$.

The small-strain E_{max} and tangent $E_{tangent}$ stiffnesses are normalized with their initial values and are plotted in **figure 3.9b**. Clearly, a small-strain measurement is not equal to the local tangent modulus $d\sigma / d\varepsilon$ of a large-strain phenomenon (Brown 1996). The deformation mechanisms are different: small-strain wave propagation causes elastic deformation solely at particle contacts, while large strain testing implies contact sliding and fabric change. Thus, the evolution of the small-strain stiffness must be carefully considered when making correlations to the stress-strain response, which is of practical interest in most applications. In essence, small-strain stiffness is a measure of the state at constant fabric while large-strain measurements assess the resistance to the fabric change.

3.6 Conclusions

A true triaxial device was designed and built to measure the stress-dependent small-strain stiffness of granular bases in all three principal directions. The device is rigid to allow compaction of the granular base inside the chamber, avoids edge effects and minimizes side friction, and it can be used to impose any arbitrary stress history. Salient conclusions from a preliminary set of tests follow:

- There is marked inherent stiffness anisotropy in unbound aggregate base materials: under isotropic stress conditions, the vertical small-strain stiffness is higher than the horizontal stiffness by an average factor of 1.3 for the laboratory conditions tested.
- The longitudinal normal stress best describes the stress sensitivity of the unbound aggregate base small-strain longitudinal stiffness. Transverse stresses seem to have a secondary effect.
- The stress dependency of small-strain Young's modulus E on the longitudinal normal stress adds to the inherent stiffness anisotropy due to fabric and can result in pronounced stiffness anisotropy.
- The tangent stiffness derived from the large deformation stress-strain response is not equal to the instantaneous small strain-stiffness calculated from wave propagation. Differences reflect the underlying deformation mechanisms: contact deformation in small-strain versus fabric change during large strain.

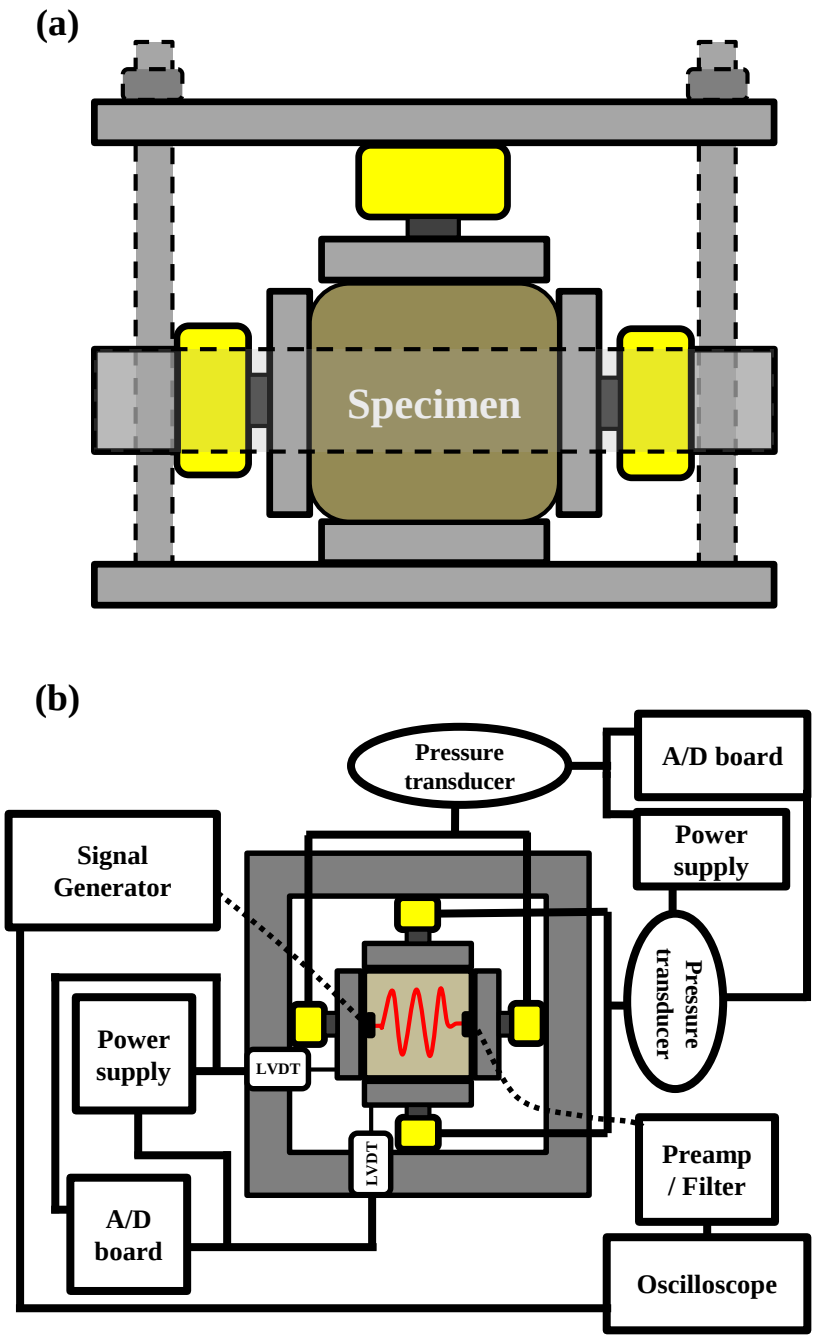

Figure 3.1. True triaxial chamber: (a) Side view and (b) top view and peripheral components.

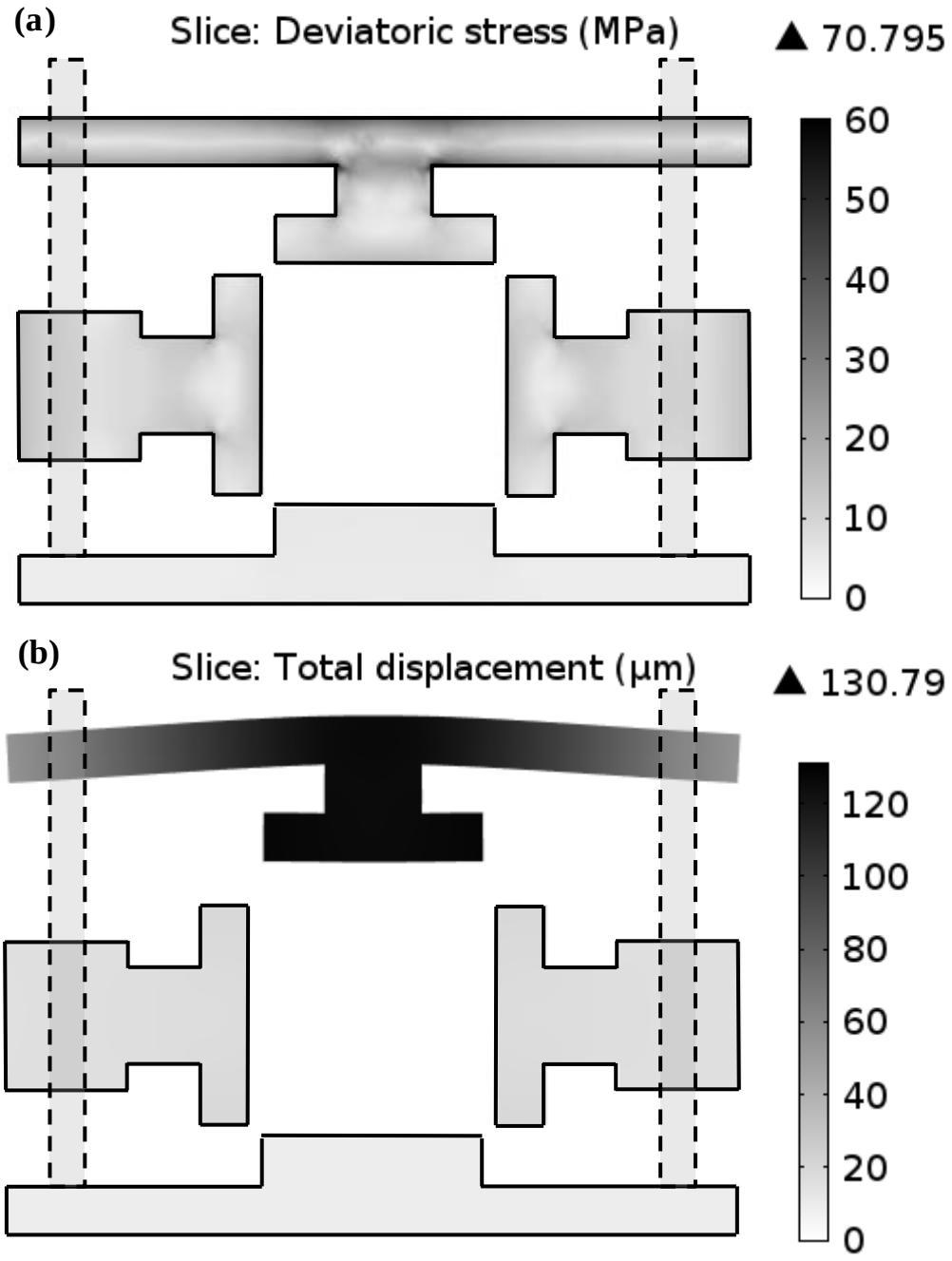

Figure 3.2. Results from stress analysis of the cubical triaxial frame; contours of (a) deviatoric stress and (b) displacement along the middle cross section.
Note: deformation is magnified by a factor of 100.

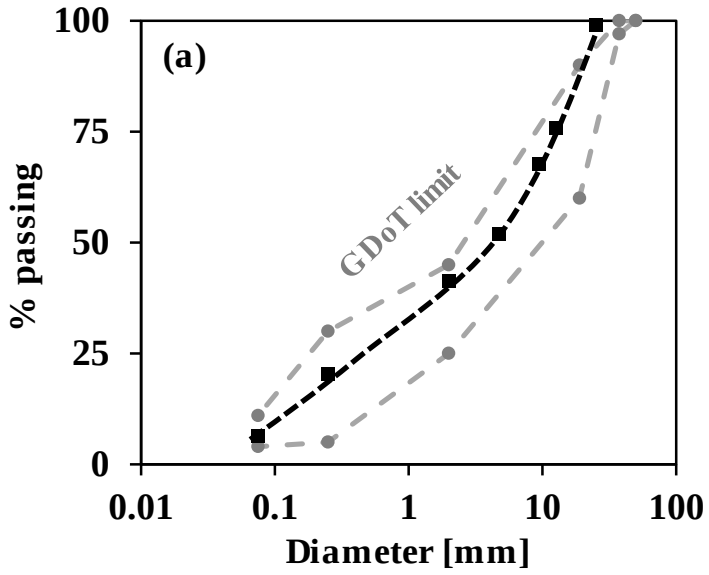

Figure 3.3. Grain size distribution for the tested GAB (Aggregate source: Griffin quarry, GA).

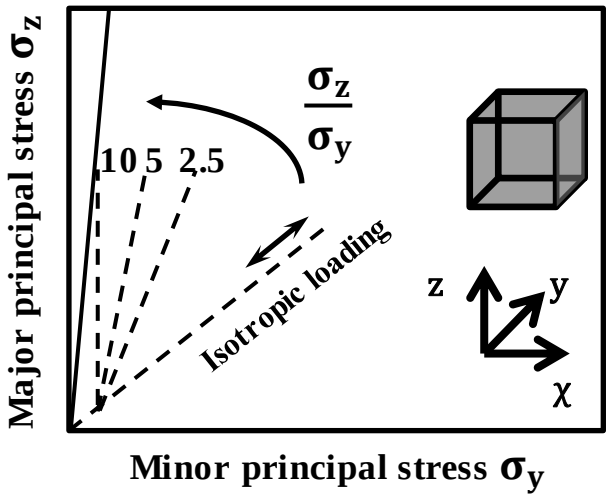

Figure 3.4. Loading sequence followed during constant stress path testing ($\sigma_y = \sigma_x$).

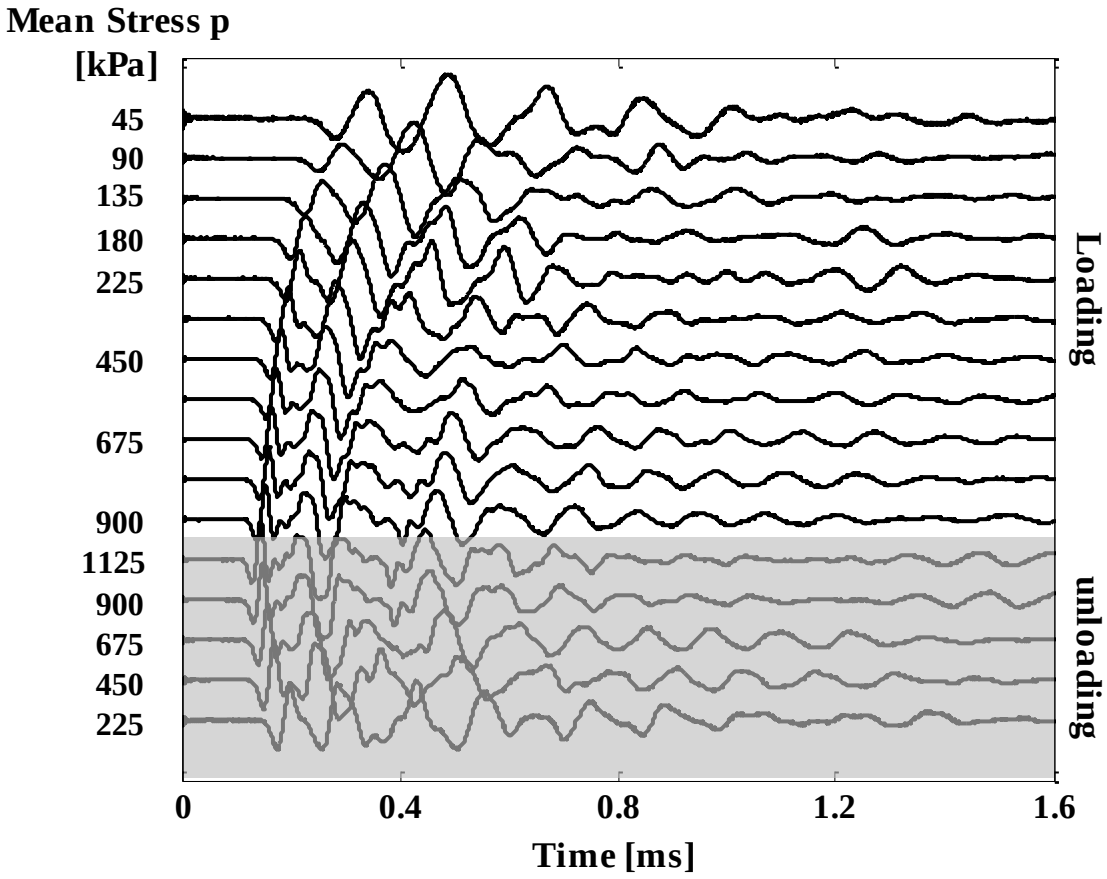

Figure 3.5. Cascade of waveforms captured in the vertical direction during isotropic loading and unloading.

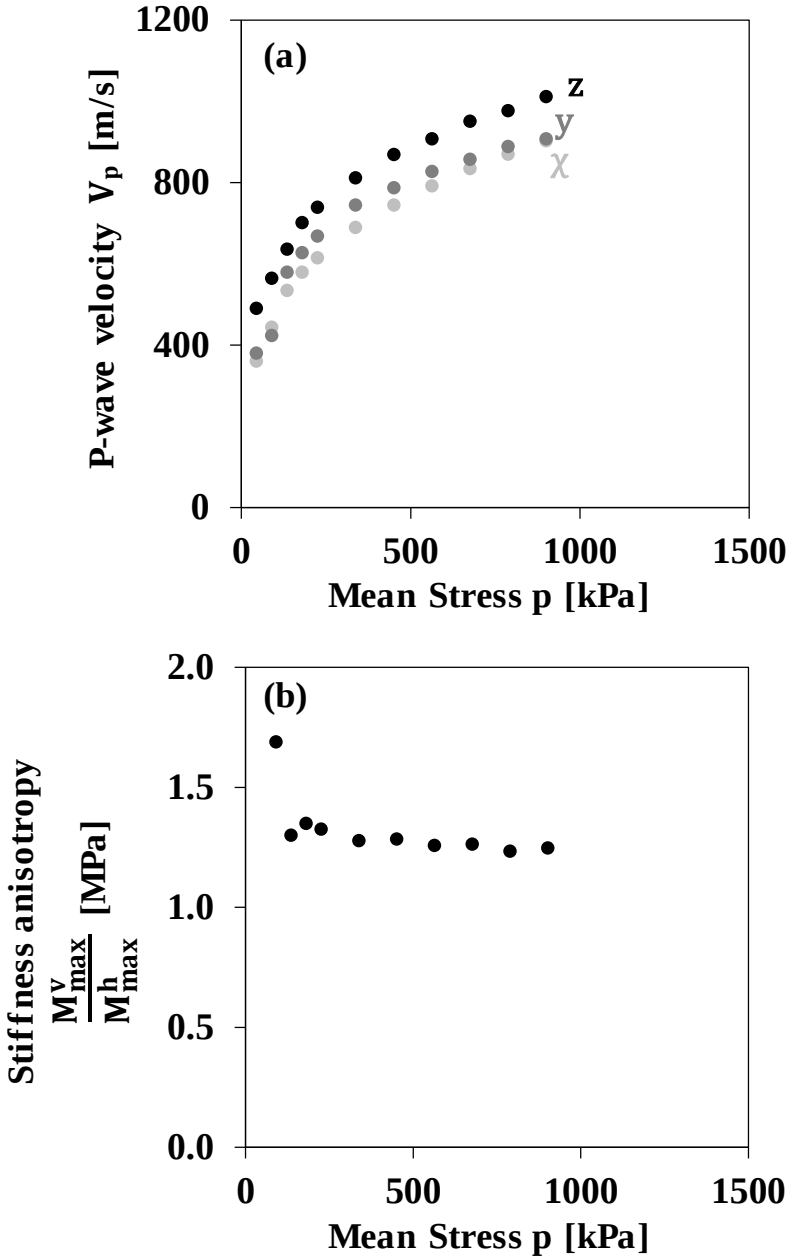

Figure 3.6. Variation of small-strain stiffness with stress under isotropic loading conditions: (a) wave velocity V_p for the three different directions and (b) ratio of vertical to horizontal small-strain constrained modulus M_{max} versus mean stress $p = (\sigma_1 + \sigma_2 + \sigma_3)/3$.

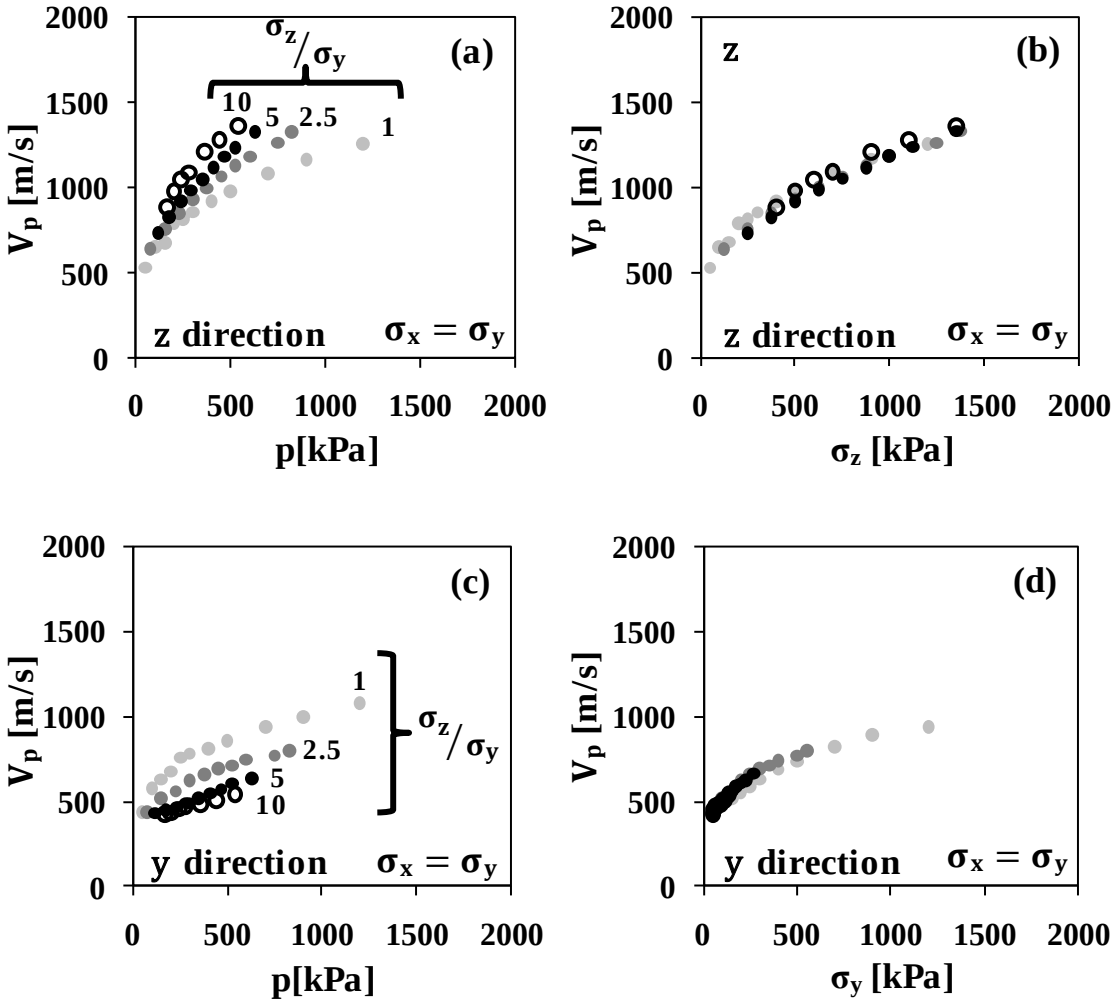

Figure 3.7. P-wave velocity V_p measured in the vertical direction z versus (a) mean stress p and (b) vertical stress σ_z . P-wave velocity in the horizontal direction y versus (c) mean stress and (d) horizontal stress σ_y. Different dots correspond to different stress ratios of vertical stress over horizontal stress σ_z/σ_y.

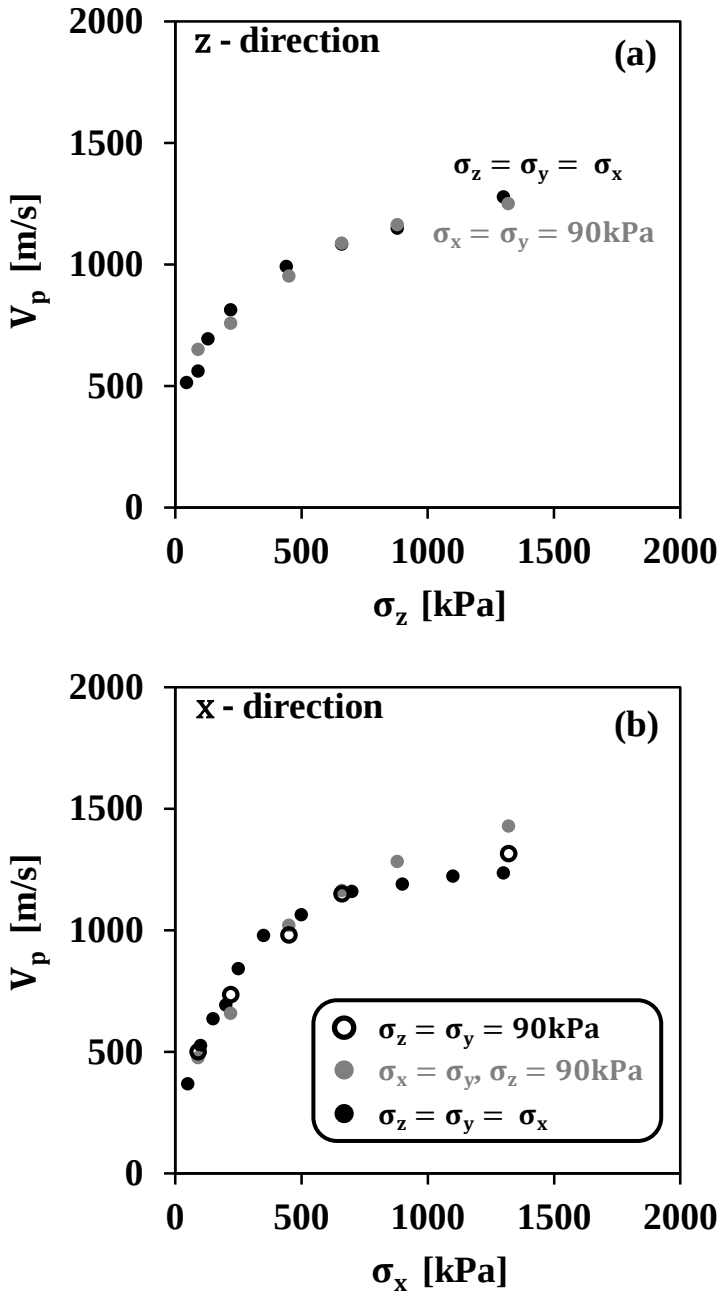

Figure 3.8. p-wave velocity v_p versus normal stress σ_x and σ_z for propagation in the (a) z and (b) x direction.

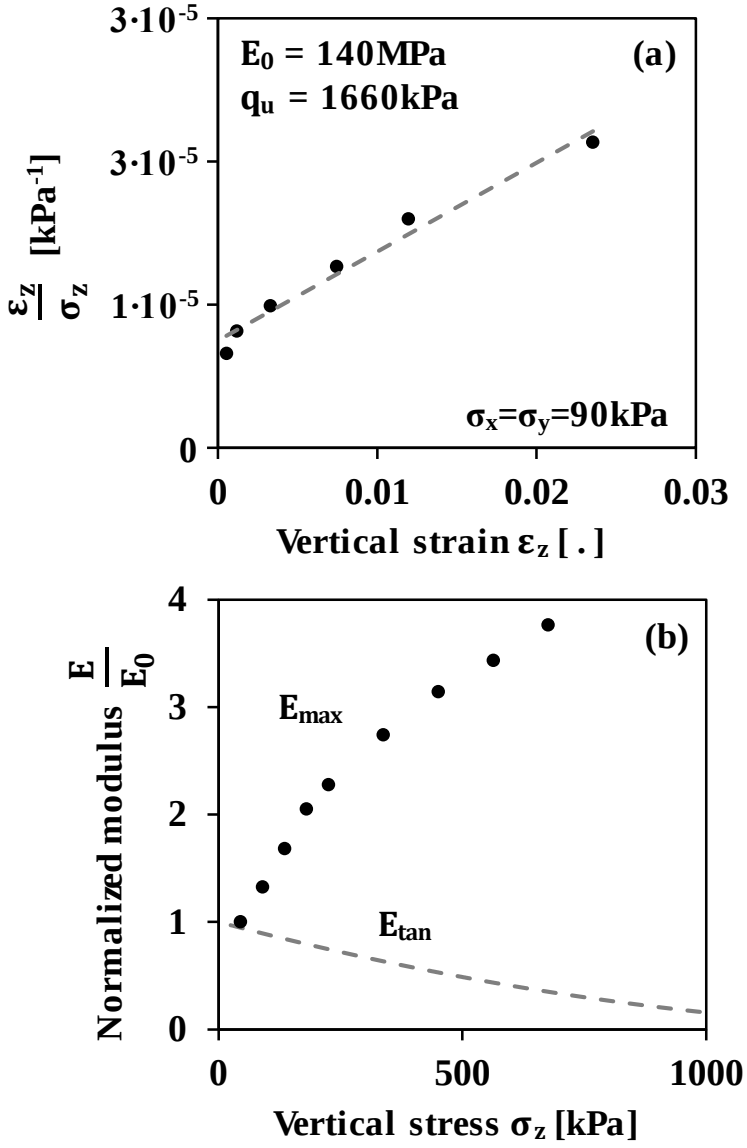

Figure 3.9. Comparison between tangent stiffness E_{tan} and small-strain stiffness E_{max} : (a) stress-strain response under triaxial compression in hyperbolic coordinates and fitted hyperbolic model. (b) Evolution of normalized tangent Young's modulus E_{tan} derived from the hyperbolic model and normalized small-strain vertical Young's modulus E_{max} from V_p measurements with vertical stress.

CHAPTER 4
THE USE OF SMALL-STRAIN STIFFNESS TO ASSESS THE COMPACTION OF GRANULAR BASES

4.1 Introduction

Compaction is the densification of a granular material through the application of mechanical energy. It is commonly implemented during the construction of embankments and dams, clay liners, pavement subgrades and bases (Seed 1959). Soil compaction is used to: (1) decrease compressibility; (2) increase strength; (3) decrease permeability and/or (4) mitigate volume changes due to shrinkage, swelling or freeze/thawing cycles (Holtz 1990). The work of R.R. Proctor was instrumental in providing the foundation for engineered compaction of geomaterials (Proctor 1933). Advances in compaction equipment have led to discrepancies between laboratory attainable densities and values realized in situ.

Compaction is evaluated in terms of dry density; however the goal of compaction in most applications is stiffness, strength or permeability and there is poor correlation between these properties and dry density (Kaya et al. 2012). For example, the addition of fines increases density but a high fines-fraction hinders performance; hence State agencies had to impose strict limitations on materials and gradations in addition to density requirements (Marek 1974).

Compaction defines the mechanical performance of unbound aggregate bases in pavements, both during a single load application (resilient response) as well as under long–term traffic loading (rutting); hence compaction plays a critical role in the overall

pavement performance. Indeed granular base stiffness is an essential input parameter in the FHWA Mechanistic-Empirical Pavement Design Guidelines (NCHRP 2004).

In this study, a set of laboratory experiments are conducted to assess the use of small-strain wave propagation in evaluating the compaction of granular bases. The small-strain stiffness is monitored throughout loading-unloading cycles to determine the stress sensitivity of the granular base stiffness. Parameters are compared against a database of natural and remolded soils. Finally the influence of boundary effects in laboratory measurements is discussed.

4.2 Previous Studies

Clayey Soils: There have been extensive studies on the effect of compaction parameters such as water content, applied energy and compaction method on the characteristics of compacted clays (Barden and Sides 1970; Mitchell 1981; Mitchell et al. 1965; Seed 1959). Water content determines the fabric of compacted clays and it controls the stiffness of compacted subgrade soils, primarily due to capillarity (Delage et al. 1996; Otani et al. 2013). The small-strain stiffness of silty sands compacted on the dry side of optimum is primarily affected by the compaction energy and fines content, while matric suction has a larger effect for specimens on the wet side of optimum (Heitor et al. 2012; Indraratna et al. 2012). However, differences in the small-strain stiffness response exhibited by specimens compacted dry or wet of optimum are inadequate for the robust assessment of compaction (Claria and Rinaldi 2007).

Granular bases: Data from both accelerated pavement tests and laboratory tests suggest that the stiffness of unbound aggregate layers is primarily affected by the degree

of compaction, the degree of saturation and the state of stress (Theyse 2002). Vibratory compaction yields higher values of shear strength, stiffness and CBR for the same material at the same degree of compaction (Kaya et al. 2012; Long et al. 2011). Small-strain wave propagation methods have been proposed to assess the stiffness of compacted granular bases as well (Cortes 2010; Kim and Park 1999; Kim et al. 2001; Lu et al. 2004). However, the effect of different compaction parameters on small-strain stiffness remains unclear. Furthermore, there is very limited information regarding the influence of compaction on the stress-dependent stiffness of granular bases.

4.3 Experimental Setup

4.3.1 Chamber Design – Procedure

An experimental study was designed to assess the stress-dependent post-compaction stiffness of granular bases using small-strain wave propagation. The device is based on a standard large diameter compaction mold (ID=152mm **Figure 4.1**). The specimen is compacted using the modified Proctor method, at several water contents. After compaction, a circular plate and pedestal are placed at the top and bottom of the specimen. A pair of MATEC 50 kHz piezocrystals is used to conduct wave propagation measurements. The vertical load is applied with a 30kN load frame and monitored with a load cell. The mold "floats" relative to the end plates to minimize wall friction. A quasi-static loading-unloading cycle is imposed (maximum vertical stress 1300 kPa). P-wave velocity measurements are conducted during loading and unloading.

4.3.2 Material Tested

Graded aggregate base from the Griffin Quarry in Georgia was used for these experiments. **Table 4.1** summarizes the aggregate properties. The pre-compaction gradation of the material tested falls within the Georgia DOT limits for GAB (**Figure 4.2a**). A total of 9 specimens each compacted with the same energy, were tested. The compaction curve is shown in **Figure 4.2b**. The maximum density is 2.19Mg/m^3.

4.4 Test Results

4.4.1 Small-Strain Stiffness

A typical cascade of P-wave signals recorded at the receiver is shown in **figure 4.3**. The small-strain constrained modulus M_{max} can be calculated from the measured P-wave velocity V_p:

$$M_{max} = \rho \cdot V_p{}^2 \quad (1)$$

where ρ is the specimen density. Small-strain moduli M_{max} for all specimens are plotted versus vertical stress in **figure 4.4**. Both loading and unloading response are shown. For all specimens, the stiffness is clearly increasing with stress following a power law. The stiffness response varies among specimens. Also, there is considerable hysteresis in the unloading response with the small-strain stiffness following a flatter curve. **Figure 4.5** shows the variation of small-strain constrained modulus with water content at different levels of vertical stress. For the same vertical stress, the discrepancy between specimens is small with the exception of the specimen compacted at 8.5% water content which shows an unusual increase in stiffness at high stress, potentially attributed to saturation.

Figure 4.6 shows the difference between the small-strain stiffness in loading and unloading ΔM_{max} calculated at different levels of vertical stress. Results are plotted both versus dry density and versus water content. There seems to be an increasing trend in the change in stiffness with water content. On the other hand, results do not seem to be affected by dry density.

The wave velocity stress-dependency in granular materials typically follows a power-law equation:

$$V_p = \alpha \cdot \left(\frac{\sigma}{kPa}\right)^{\beta} \quad (2)$$

where α is the P-wave velocity at σ=1kPa and the exponent β captures the stress sensitivity of V_p. **Figure 4.7** shows the calculated α and β parameters versus the water content for all tested specimens. The exponent β increases with water content while α shows no clean trend. P-waves are related to shear waves through the elasticity equations:

$$V_s^2 = V_p^2 \cdot \frac{(1-2v)}{(2-2v)} \quad (3)$$

Equations (3) allows the estimation of α and β values for S-wave propagation. **Figure 4.8** shows the equivalent S-wave coefficients plotted against each other along with data from numerous natural and remolded soils and jointed rocks (Cha et al. 2014) (assumed v=0.1). Compacted granular bases fall between jointed rocks and sands, having a higher α-factor for a given β-exponent compared to natural soils.

4.4.2 Repetitive Loading

Unbound aggregate bases experience a large number of load repetitions after compaction and may gradually accumulate permanent deformation. Eventually, unbound materials reach a resilient state (shakedown) or continue to accumulate deformation

indefinitely (ratcheting). An additional test was conducted to track the evolution of the small-strain stiffness during repetitive loading. The specimen was compacted at a water content of 2% resulting in a density of 2.08Mg/m^3. A permanent vertical load of 28kPa was imposed on the specimen to simulate at-rest conditions. Then, the specimen was subjected to a total of 128 load repetitions up to a maximum stress of 580kPa, representative of wheel loading. P-wave measurements and vertical deformation were recorded at both the maximum and minimum stress (see cascades in **Figure 4.9a**). Signals were analyzed using CODA wave methods.

The accumulated vertical deformation increases with the number of cycles; however the rate of accumulation decreases (**figure 4.9b**). The effective elastic stiffness of the specimen increases with the number of cycles (**Figure 4.10)**.

4.5 Analysis

4.5.1 Boundary Effects on Stiffness

The use of a zero-lateral strain cell permits specimens compaction and testing in the same chamber and minimizes sample disturbance. Furthermore, loading conditions in a K_0 chamber are similar to those experienced by a granular base element directly beneath the load. However there are inherent difficulties associated with the interpretation of a zero lateral strain test data due to wall friction.

Consider a soil element under axisymmetric zero radial strain conditions. For a given vertical stress σ_{vert} the horizontal stress σ_{hor} can be estimated as:

$$\sigma_{hor} = K_0 \cdot \sigma_{vert} \quad (4)$$

where K_0 is the coefficient of lateral earth pressure. A simple Coulomb friction law yields a first estimate of the resulting shear stress τ mobilized by the element:

$$\tau = \mu \cdot \sigma_{hor} \tag{5}$$

where μ is the friction coefficient. The difference between the vertical force at the top and bottom of a disk element of height dz is equal to the shear force against the wall:

$$-\frac{\pi D^2}{4} d\sigma_{vert} = \mu k_0 \sigma_{vert} \pi D dz \tag{6}$$

where D is the chamber diameter and z is the depth from the top. The solution of the differential equation yields an exponential decay of the vertical stress as a function of depth:

$$\sigma_{vert} = \sigma_{top} e^{-4\mu k_0 \frac{z}{D}} \tag{7}$$

where σ_{top} is the externally applied vertical contact stress. If the mold is "floating" and free to move vertically, the top and bottom contact stresses are equal and therefore the solution is symmetric with respect to the specimen mid-plane:

$$\sigma_z(z) = \sigma_z(H - z) \qquad \text{for } z > H/2 \tag{8}$$

Equation 7 shows that vertical stress reduces exponentially with depth, and a low aspect ratio H/D is necessary to minimize wall friction effects on measurements.

Wall friction and stress reduction affects the determination of the stress-dependent stiffness. The total travel t_T is the integral of differential travel times along the propagation path z:

$$t_T = 2 \int_0^{H/2} \frac{1}{V_p} \cdot dz \tag{9}$$

Consider a stress-dependent wave velocity in the form of:

$$V_p = \alpha \cdot \left(\frac{\sigma_{vert}}{kPa}\right)^{\beta} \quad (10)$$

Using equations (1) and (7), the closed form solution for the calculated wave velocity $V_p{}^{ap}$ is a function of the wave velocity for the actual state of stress $V_p{}^{real}$:

$$V_p{}^{ap} = V_p{}^{real} \cdot \frac{2\mu k_0 \beta \frac{H}{D}}{e^{(2\mu k_0 \beta \frac{H}{D})} - 1} \quad (11)$$

Note that the apparent wave velocity is always smaller than the true wave velocity at that state of stress. Nevertheless, this may not be the case during unloading due to the mobilization of negative friction. For the experimental study presented above, friction can lead to an underestimation of wave velocity by 25%.

4.6 Discussion

Results from the laboratory study show that the water content has a minor effect on the stiffness of unbound aggregate layers when compared to the effect of the state of stress. Indeed, **figure 4.5** shows that a change in water content from an almost dry (0.8%) to an almost saturated (8.2%) condition only has a 20-30% effect on stiffness primarily due to the effect of saturation on P-wave velocity. On the contrary, an increase in the vertical stress from the at-rest condition (55kPa) to the loaded condition (530kPa) increases stiffness by a factor of 80% to 120% (**figure 4.5**).

The effect of water content on the stiffness of unbound aggregates is often associated to the increase in interparticle forces due to matric suction. However, simplified analytical solutions contradict this finding. The pressure difference between air and water, or matric suction, can be calculated using Laplace's equation:

$$\Delta u = \frac{2T_s}{r} \tag{13}$$

where r is the radius of the curvature and T_s=72.7mN/m is the surface tension of the air-water interface (Cho and Santamarina 2001). The radius r is of the order of the minimum grain radius, i.e. $r = \frac{D_{10}}{2} = 0.05$mm for GAB material at the verge of air invasion. This radius yields an equivalent matric suction of $\Delta u = 3$kPa and can be disregarded in the stress analysis.

Matric suction can reach significantly higher values during drying as the remaining water concentrates at menisci at particle contacts (pendular regime). Terrell et al. (2003) reported matric suction around 80kPa for GAB material at water content w=2%. Nevertheless, in this case suction contributes to interparticle forces proportionally to the menisci area, as per Bishop's effective stress concept (Bishop and Blight 1963). Using the analytical equations derived by Cho and Santamarina (2001) for spherical particles of radius $R = D_{50} = 2$mm, a matric suction of 80kPa corresponds to an equivalent menisci radius of $r = 0.9\mu$m which increases the effective stress by 0.116kPa. This small effect of suction on effective stress explains the insensitivity of P-wave velocity to compaction water content in grade aggregate bases and other coarse-grained materials.

4.7 Conclusions

A series of laboratory tests were conducted to assess the effect of water content on the stress-dependent stiffness characteristics of compacted granular bases. Results show that:

- Unbound aggregate bases exhibit stress-dependent stiffness. The small-strain stiffness of all samples follows a power-law equation with stress.
- Water content and dry density have a secondary effect on the small-strain stiffness when compared to the effect of stress.
- The water content affects fabric changes during loading as evidenced by the residual change in wave velocity between loading and unloading.
- The small-strain stiffness M_{max} follows an exponential trend with the number of load cycles during repetitive loading.
- The α and β parameters that characterize the stress-dependent stiffness of unbound aggregate bases are similar to the upper bound of values for granular soils.
- Wall friction in rigid boundary chambers reduces the vertical stress in the specimen and results in underestimation of the small-strain stiffness.
- Suction has only a minor effect on the stiffness of unbound aggregate bases and can be disregarded with respect to the stiffening effect of externally applied stress.

Table 4.1. Aggregate properties. Specimens from Griffin Quarry, GA.

Aggregate Source	Griffin Quarry (Griffin ,GA)
Aggregate group	II
Class	A
Bulk Specific Gravity	2.634
Theoretical GAB Density	2.19 Mg/m^3
Optimum water content	6.1%
LA abrasion loss	49%
# of specimens Tested	9
Maximum dry density	2.19 Mg/m^3
Optimum water content	7.1%

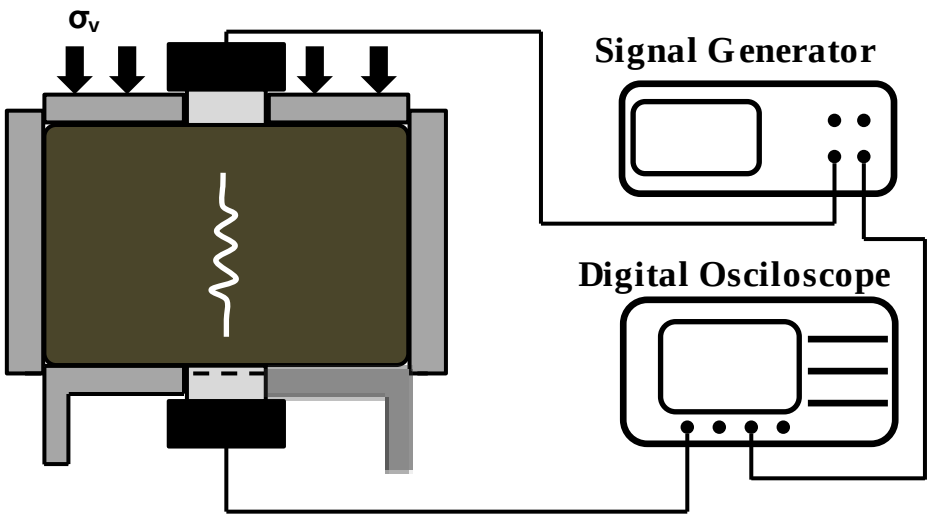

Figure 4.1. Instrumented compaction chamber and peripheral electronics.

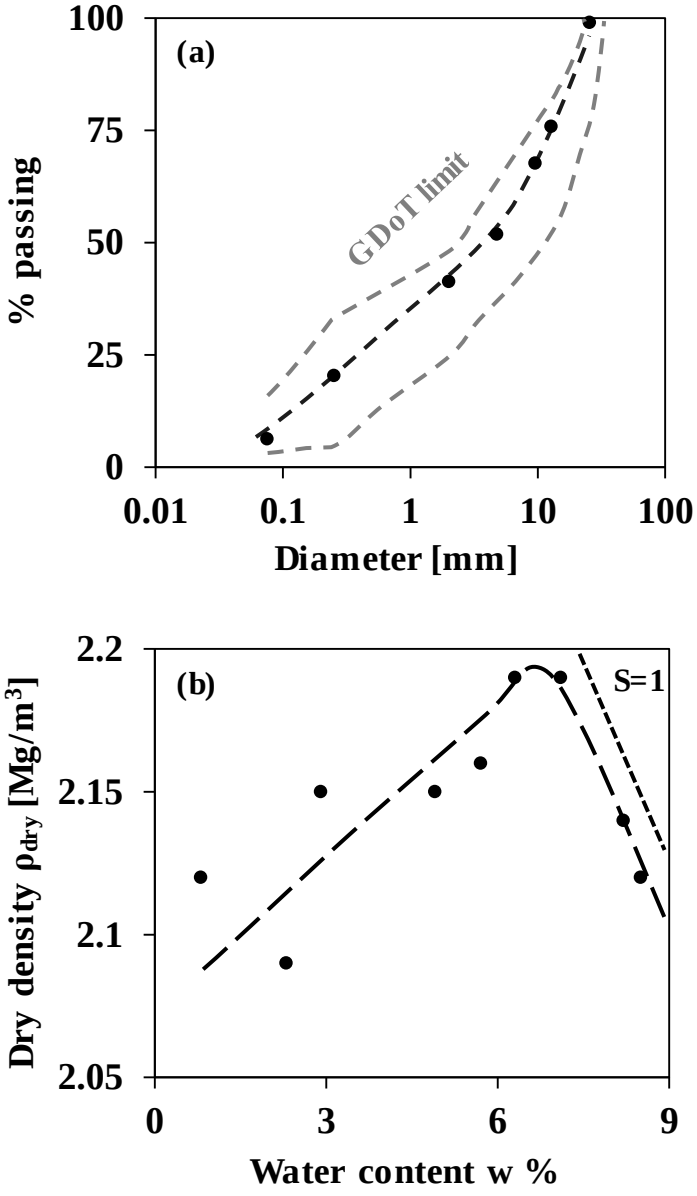

Figure 4.2. Aggregate characteristics. (a) Grain size distribution and (b) compaction curve obtained using the modified method. The S=1 line corresponds to the zero air voids line.

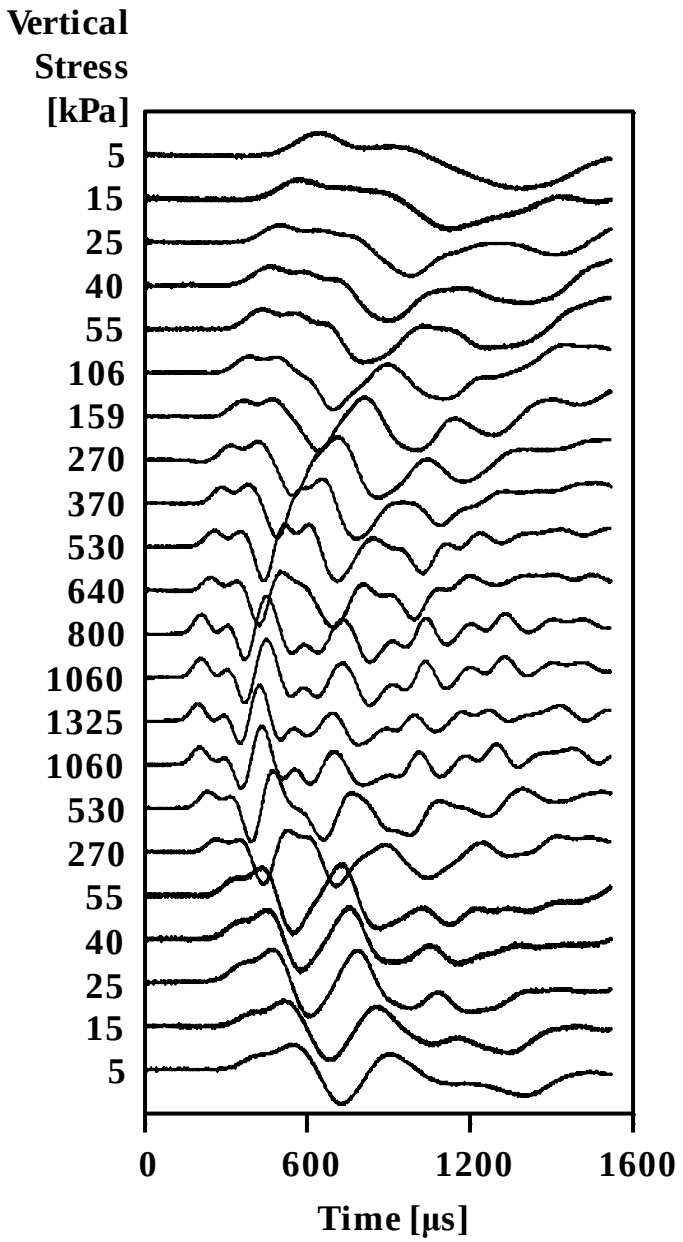

Figure 4.3. Typical cascade of P-wave signals captured during loading and unloading.

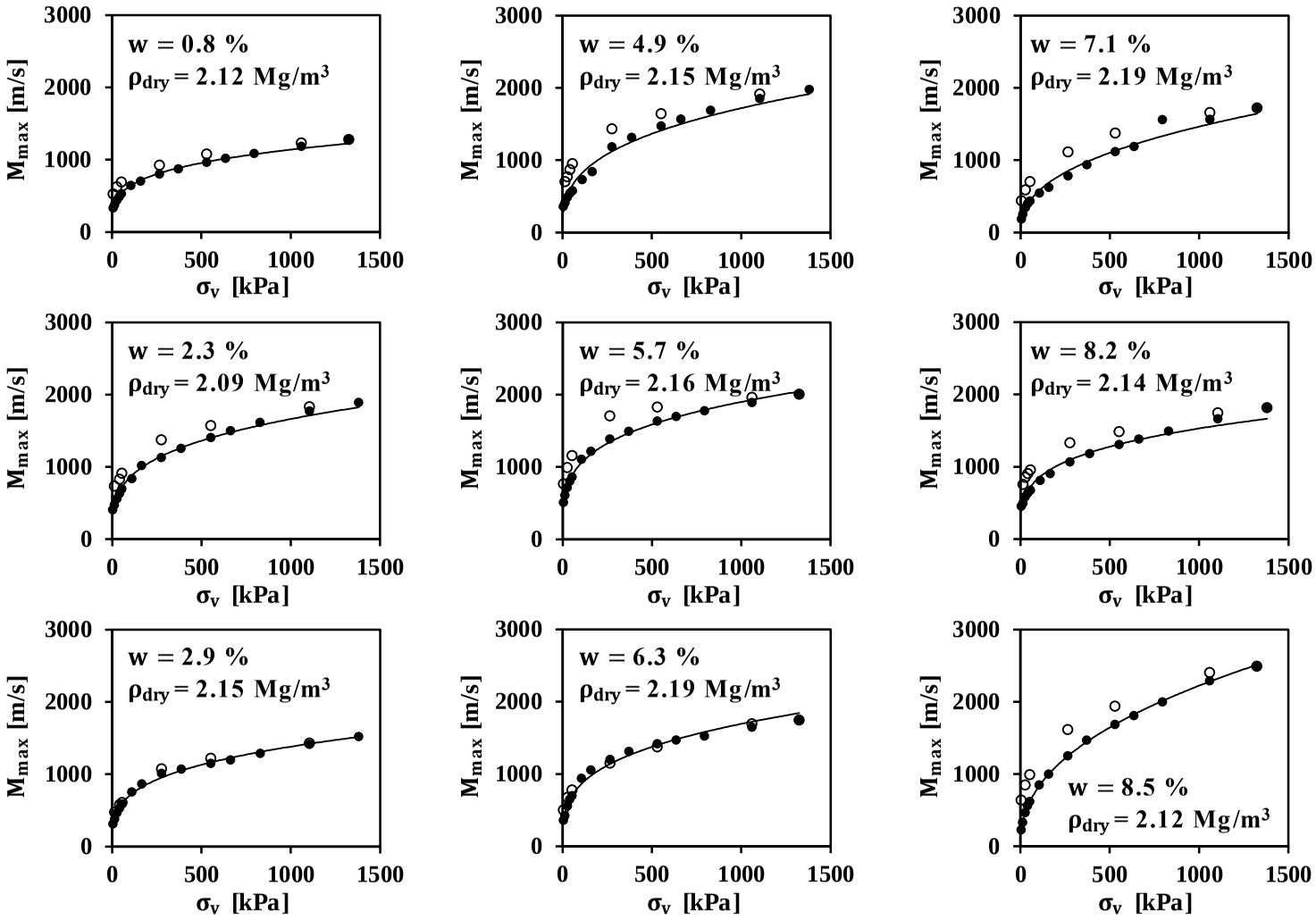

Figure 4.4. Small-strain constrained modulus M_{max} versus vertical stress σ_v. Specimens compacted at different water contents. Filled points: loading. Empty points: unloading.

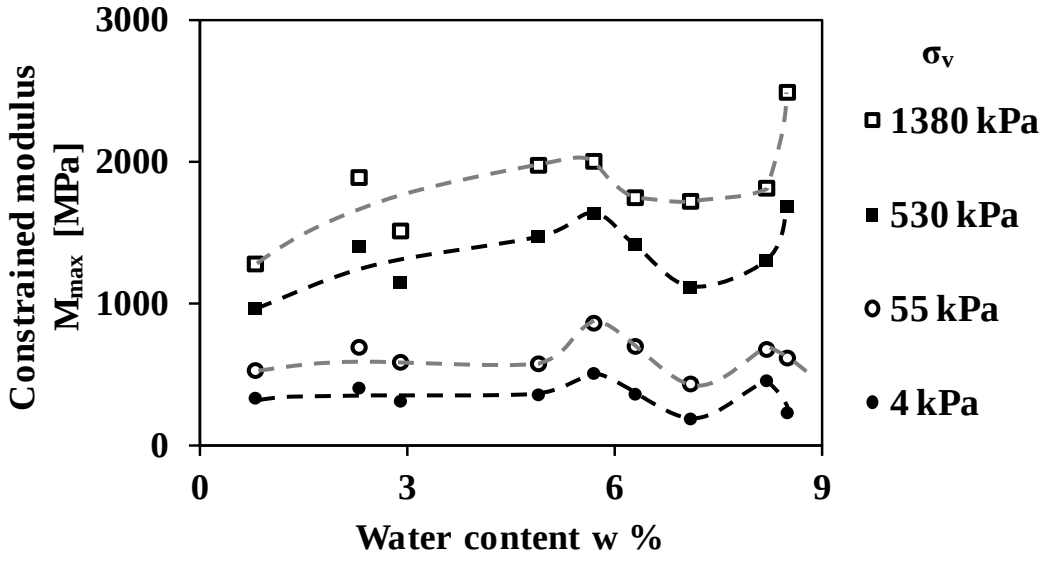

Figure 4.5. Variation of small-strain constrained modulus M_{max} with water content w at different vertical stress levels σ_v.

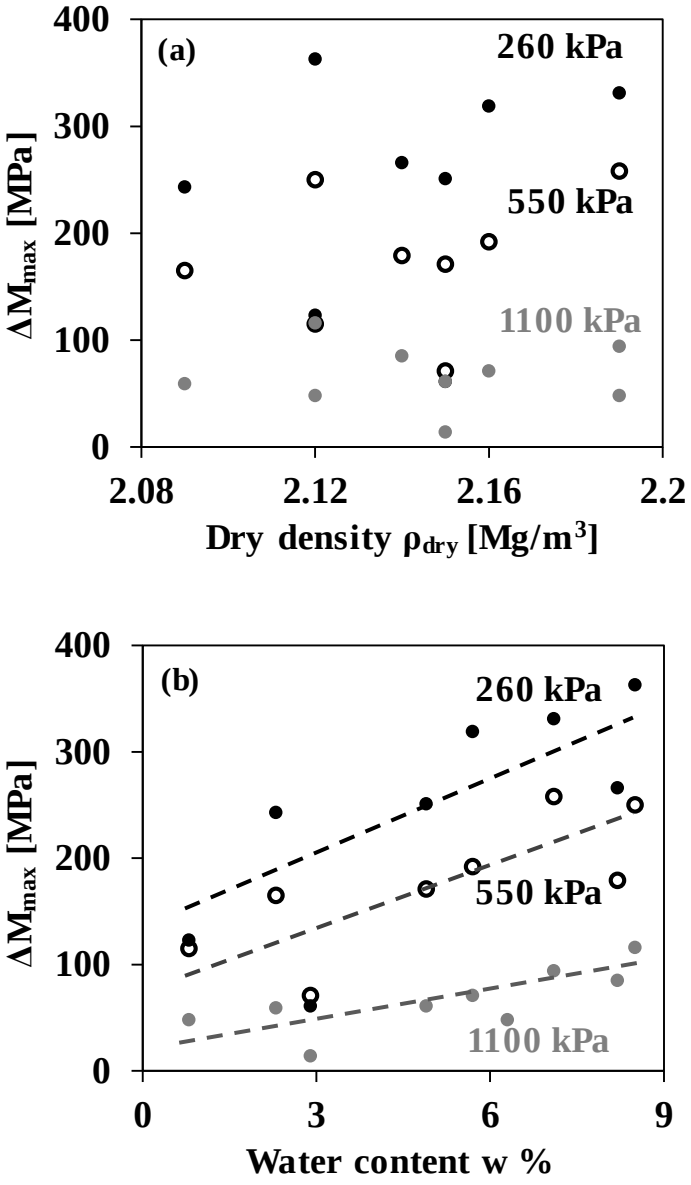

Figure 4.6. Difference in the small-strain constrained modulus between loading and unloading ΔM_{max} at different vertical stress levels plotted versus (a) dry density ρ_{dry} and (b) water content w. .

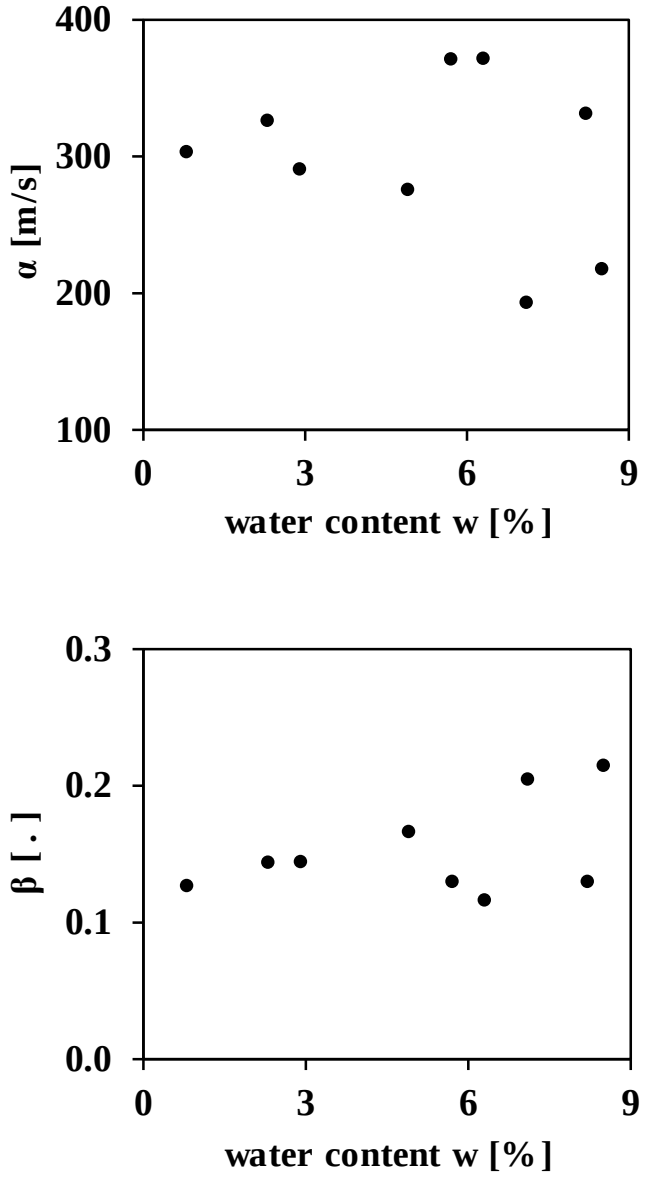

Figure 4.7. Variation of velocity parameters α-factor and β-exponent with water content.

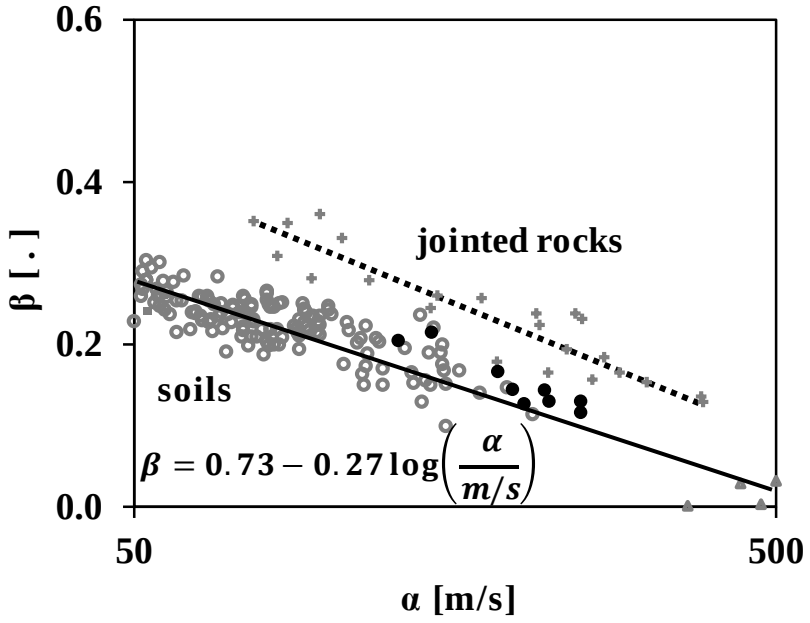

Figure 4.8. Velocity-stress parameters α versus β for the specimens tested (black points) **Note:** Grey points are data gathered from the literature (replotted from Cha and Santamarina 2014).

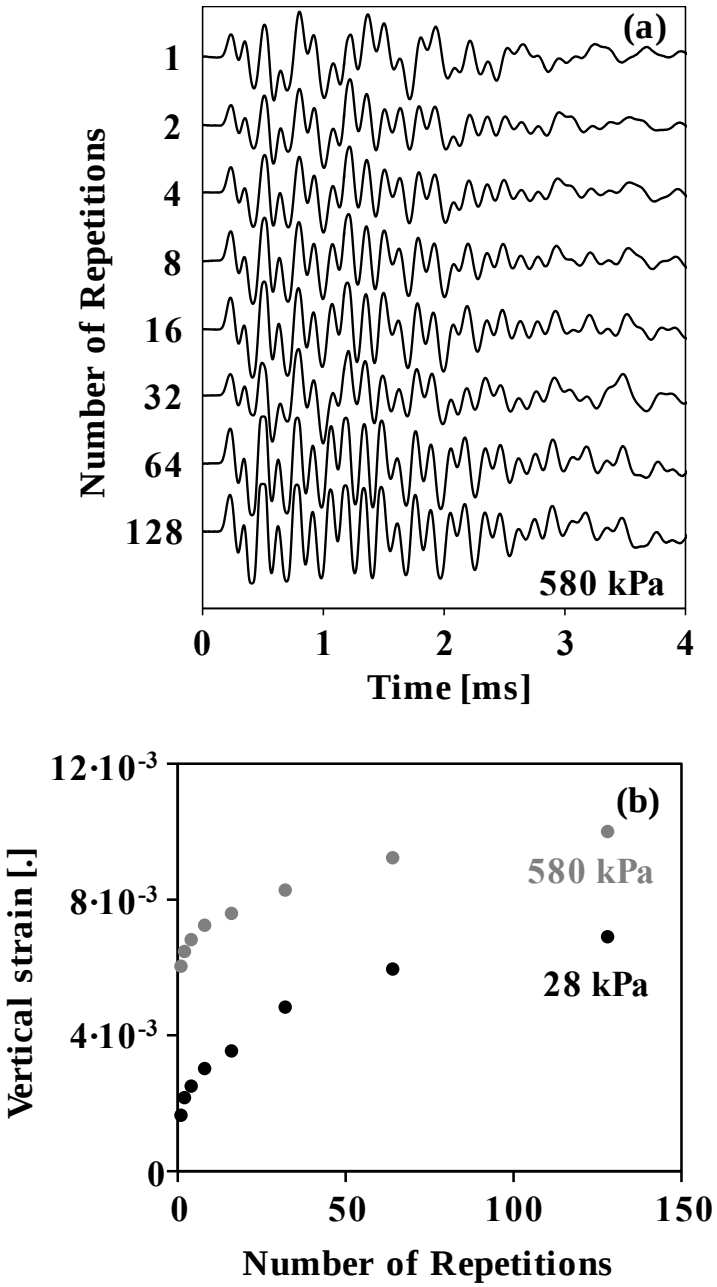

Figure 4.9. Repetitive loading. (a) Cascade of signals for vertical stress σ_v= 580 kPa and (b) vertical strain versus number of cycles at two levels of vertical stress σ_v in each cycle: no tire load (28kPa) and tire load (580kPa).

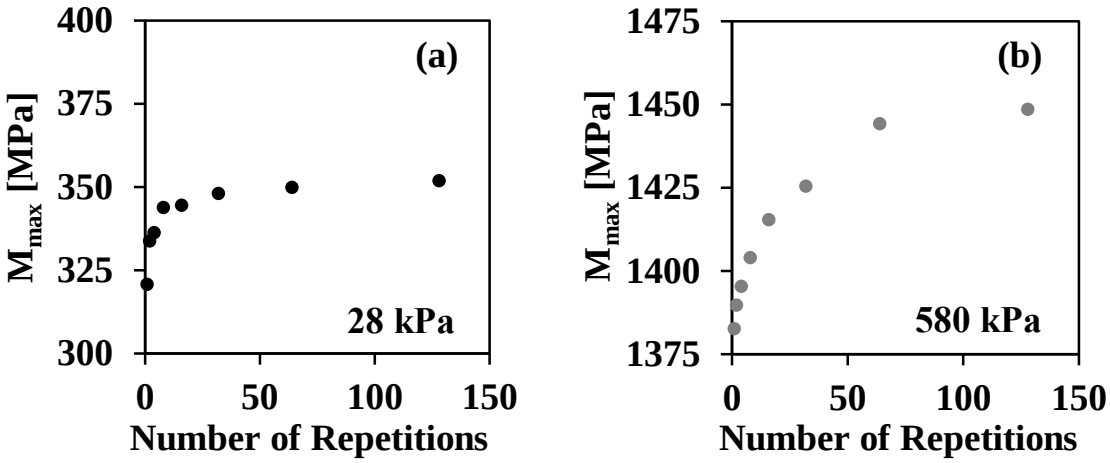

Figure 4.10. Small-strain constrained modulus M_{max} versus number of load repetitions measured at (a) σ_v= 28 kPa and (b) σ_v= 580 kPa.

CHAPTER 5
IN SITU ASSESSMENT OF THE STRESS-DEPENDENT STIFFNESS OF UNBOUND AGGREGATE BASES IN INVERTED BASE PAVEMENTS

5.1 Introduction

Stress redistribution within a pavement structure is determined by the relative flexural rigidity between successive pavement layers i.e. stiffness and thickness (Acum and Fox 1951; Burmister 1945; Burmister et al. 1943). Consequently layer stiffness is a governing parameter in the calculation of a pavement's structural capacity (AASHTO 1993; NCHRP 2004).

Granular bases support the surface asphalt concrete layers and protect the subgrade. A unique characteristic of granular bases is their anisotropic and stress-dependent stiffness (Adu-Osei et al. 2001; Rowshanzamir 1997; Tutumluer and Thompson 1997; Uzan 1985). There have been only a few attempts to measure the stress-dependent stiffness of granular bases insitu (Terrell et al. 2003), even though granular bases can be the primary load-bearing layer, as in inverted base pavements (Cortes and Santamarina 2013; Tutumluer 2013).

This chapter documents the development of an experimental procedure to assess the insitu stress-dependent small-strain anisotropic stiffness of granular bases through wave propagation techniques. Two test protocols are developed to measure the horizontal and vertical stiffness independently. The methodology is applied to two distinct cases of inverted base pavements.

5.2 Previous Studies

The resilient Modulus M_r is used in pavement engineering to describe layer stiffness (Hicks and Monismith 1971). Several laboratory tests have been developed to determine the resilient modulus of granular bases (FHWA 1996; NCHRP 2002; Puppala 2008; Tutumluer and Seyhan 1999). These tests simulate material compaction and loading history under field conditions. However, neither laboratory compaction is representative of roller compaction, nor do the stress conditions imposed during laboratory tests capture the complexity of the stress history and stress field experienced by the granular base under working conditions (Drnevich et al. 2007; Tutumluer 2013). Furthermore, most tests neglect the inherent as well as the stress-induced stiffness anisotropy of the granular base (Al-Qadi et al. 2010; Kopperman et al. 1982; Oda et al. 1985; Santamarina and Cascante 1996).

Several techniques have been devised for the insitu measurement of the stiffness of unbound aggregate bases (Fleming et al. 2000). Commercially available systems include the Falling Weight Deflectometer FWD, the Light Weight Deflectometer, and the Seismic Pavement Analyzer SPA (Fleming et al. 2007; Nazarian et al. 1993; NCHRP 2008). In all three cases a dynamic load is applied. The first two methods measure surface deformations under an impulse load, while the SPA uses wave propagation. P-wave velocity V_p is related to constrained modulus M_{max} and bulk density ρ:

$$M_{max} = \rho \cdot V_p{}^2 \tag{1}$$

Similarly, the shear wave velocity is related to shear modulus G_{max}:

$$G_{max} = \rho \cdot V_s^2 \quad (2)$$

Recent studies have attempted to relate laboratory and field-measured stiffness values using wave propagation to the resilient modulus of granular bases in the field (Schuettpelz et al. 2010; Williams and Nazarian 2007).

The primary limitation of conventional in-situ testing techniques is that the state of stress in the pavement during measurement is unknown. Furthermore, most conventional methods do not explore the anisotropic stiffness properties of the granular base (Adu-Osei et al. 2001; Arthur and Menzies 1972; Gazetas 1981; Roesler 1979; Tutumluer and Seyhan 1999; Wang and Al-Qadi 2012). Finally, the interpretation of boundary measurements at the pavement surface requires the simultaneous inversion of the stiffness for all layers; this procedure is mathematically complex and increases uncertainty of the inferred values.

Terrell et al. (2003) embedded several three dimensional accelerometers within the unbound aggregate base during pavement construction. They conducted wave propagation tests to measure the horizontal and vertical small-strain stiffness of the base, using a truck to apply the surface load. Most recently Cortes (2010) used a miniature crosshole test to measure the stiffness of existing pavements; this chapter documents further developments in this last methodology.

5.3 Experimental Configuration

Two test configurations are advanced to properly characterize the anisotropic stress-dependent stiffness in granular bases. In both cases, measurements are based on P-wave propagation.

Crosshole: The crosshole test configuration is selected to measure horizontal stiffness. A diamond core bit is used to advance two small (18mm) holes with minimal disturbance in the pavement structure (**figure 5.1a**). One piezocrystal is placed in each hole. High viscosity (cP= 320 mPa·s) oil is injected into the two holes to stabilize the perforations and to couple the crystals to the granular base. A 30cm diameter circular loading plate is placed on the pavement surface and load is applied with a hydraulic actuator that reacts against the frame of a loaded dump truck. The source crystal is connected to a signal generator while the receiver is connected to a preamplifier and a digital storage oscilloscope.

Uphole: The uphole configuration is used to determine the vertical stiffness of the base (Bang and Kim 2007; Borja et al. 1999). The vibration generated by a piezoelectric source is transmitted to the bottom of the empty hole (**figure 5.1b**). The rod is isolated from the perforation walls to prevent spurious signals. A piezoelectric accelerometer buried in the asphalt concrete is used as a receiver. The actuator is connected to a signal generator and power amplifier while the accelerometer is connected to a signal conditioner and finally to a digital storage oscilloscope.

5.4 Case Studies: Lagrange and Morgan County

Both tests configurations described above were used to characterize the graded aggregate base at the two inverted base pavements in Georgia (**figure 5.2**). The one in Lagrange, GA was tested on August 28 2013; its construction and material properties have been documented in Cortes and Santamarina (2013). The second case is a haul road

for the Morgan county quarry and was tested on September 27 2013; it is the same pavement tested by Terrell et al. (2003). Results from the two tests are summarized next.

5.4.1 Wave Signatures

Figure 5.3 shows a typical cascade of signals during a crosshole test. **Figure 5.4** shows the cascade of signals recorded during an uphole test. Travel time decreases with increasing contact stress, which implies an increase in stiffness. The change in the travel time for subsequent signals is very small and makes the determination of the first arrival challenging.

5.4.2 CODA Wave Analysis

Information contained in signal features after the first arrival can be used to accurately infer changes in travel time. CODA interferometry can be used to detect minute changes in signals such as during process monitoring (Dai et al. 2011; Snieder 2006; Snieder et al. 2002). CODA analysis assumes that the signal tails are products of indirect travel paths. The distance traveled along these paths is longer and therefore any change in the medium is magnified compared to the direct arrival. **Figure 5.5a** shows the superposition of two waveforms recorded during the Morgan county test at different stress levels. While the change in the first arrival is almost impossible to discern, there is an obvious shift in the signal tails.

The time-stretched cross correlation method is employed here. In this method, the time values of the "slow" signal are multiplied by a constant λ and the cross-correlation of the two signals is computed. This is repeated to identify the value of the stretching factor λ that produces the highest cross correlation (**figure 5.5b**). The optimal λ is the

ratio of travel times between two signals. The process is repeated for all subsequent signals to detect ratios of travel time. Finally the signal with the clearest first arrival is selected to determine the base travel time t_{base} while other travel times are inferred from the λ values as $t_i = \lambda_i \cdot t_{base}$. **Figure 5.5c** shows the evolution in the stretching coefficient λ with applied contact stress q for the crosshole test conducted in Morgan County. A more detailed description on the time-stretch method including the Matlab script used for signal processing is included in **Appendix I**.

5.4.3 Wave Velocity

Horizontal and vertical wave velocities are computed using travel times determined above. In the uphole test, the P-wave velocity in the graded aggregate base is calculated by subtracting the travel time in the asphalt concrete $\Delta x^{AC}/V^{AC}$:

$$V_p^{GAB} = \frac{\Delta x^{GAB}}{\left(\Delta t - \frac{\Delta x^{AC}}{V^{AC}}\right)} \tag{3}$$

It is assumed that the P-wave velocity of the asphalt concrete remains constant during the test.

Computed velocities are plotted versus the contact stress q during loading and unloading (**Figure 5.6**). The maximum contact stress at the Lagrange site was limited by the truck weight. In both cases, the P-wave velocity increases with increased contact stress. However, values are considerably larger at the Morgan county pavement, possibly due to more than 10 years of heavy traffic (Lewis et al. 2012). This argument is supported by the discrepancy in wave velocities obtained in this test and in the previous test on the same pavement conducted by Terrell et al. (2003). In contrast, the inverted base pavement section in Lagrange was constructed in 2009 and has been opened to relatively

low traffic for approximately 2 years. Nevertheless, both pavements show no hysteresis in stiffness between loading and unloading, which suggests that both pavements behave elastically.

5.5 Analyses

5.5.1 Determination of the State of Stress

The P-wave velocity in granular materials is primarily affected by the normal stress in the direction of wave propagation (See Chapter 3). Therefore, the determination of the stress-dependent stiffness for the as-built base to be used in constitutive models requires knowledge of the state of stress. Iterative numerical simulations are conducted on the two pavement structures to estimate the vertical and horizontal stress distribution in the GAB for each level of contact stress imposed. The effect of geostatic stress is taken into consideration. The measured p-wave velocity V_p is plotted versus the numerically inferred stress at the direction of propagation for both horizontally and vertically propagating waves (**figure 5.7**). The effect of stress-induced anisotropy is inherently considered; hence the difference between vertical and horizontal stiffness is related to inherent anisotropy. The ratio of vertical to horizontal stiffness varies between 2 and 4. This is considerably larger than results from previous laboratory tests (Chapter 3) and highlights the differences between field and laboratory compaction conditions.

5.5.2 Laboratory vs. Field Measurements – Discrepancies

The stiffness of granular materials is inherently stress-dependent due to contact phenomena and generally follows a power law:

$$V_p = \alpha \cdot \left(\frac{\sigma}{kPa}\right)^{\beta} \quad (4)$$

where σ is some stress variable such as the normal stress (Cascante and Santamarina 1996). The α-factor and β-exponent determined from the two tests are converted into equivalent shear wave coefficients and plotted against an extensive dataset of soils and jointed rocks (refer to chapter 4- also **figure 5.8**). In general, field-compacted GAB velocity parameters fall closer to jointed rocks as they exhibit very high stiffness.

The laboratory compacted samples tested in Chapter 4 have flatter curves (higher α, lower β) than the field-compacted granular bases. The power law formulation captures stiffness increase due to elastic contact deformation, fabric change and crushing. Field compacted granular bases have been subjected to high compaction loads as well as heavy traffic during its service life, which has resulted in asymptotically stabilizing contact crushing and particle rearrangement. The potential for further crushing or fabric during the test is small, thus the high α-factor and low β-exponent.

Matric suction can increase the equivalent effective stress in the GAB. For example matric suction as high as 80kPa has been reported for the base tested in Morgan county (Terrell et al. 2003). However, such values of matric suction occur when water remains only at small menisci between particles (pendular regime). In that case, the additional interparticle contact forces due to suction are small as intuitively predicted by Bishop's effective stress (Bishop 1968). Near saturation, a representative value for soil suction is the air-entry value. According to the soil-water characteristic curve reported by Terrell et al. (2003) the air entry value cannot be more than 5kPa, which has a very small effect in the calculations. In both cases, either semi-dry or saturated, suction has a minor effect on

the stiffness measured for this granular base; indeed, the applied load controls the stiffness of the graded aggregate base in inverted base pavements.

5.6 Conclusions

Two field testing configurations were developed to test as-built granular bases. The methodology was applied to the two inverted base pavements built in Georgia. Salient observations follow:

- The stiffness of field-compacted granular bases is anisotropic and stress-dependent.
- Robust signal processing allows the accurate determination of the stiffness-stress response even when changes in first arrivals are difficult to discern.
- The two granular bases tested were in the resilient regime.
- Field wave velocity values were considerably higher than values measured on laboratory compacted GAB. In fact, field-compacted granular base has higher initial stiffness (α-factor) and lower stress sensitivity (β-exponent) due to the extended loading history.
- Suction has a minor effect on granular base stiffness when the base material is crushed rock with limited fines content.

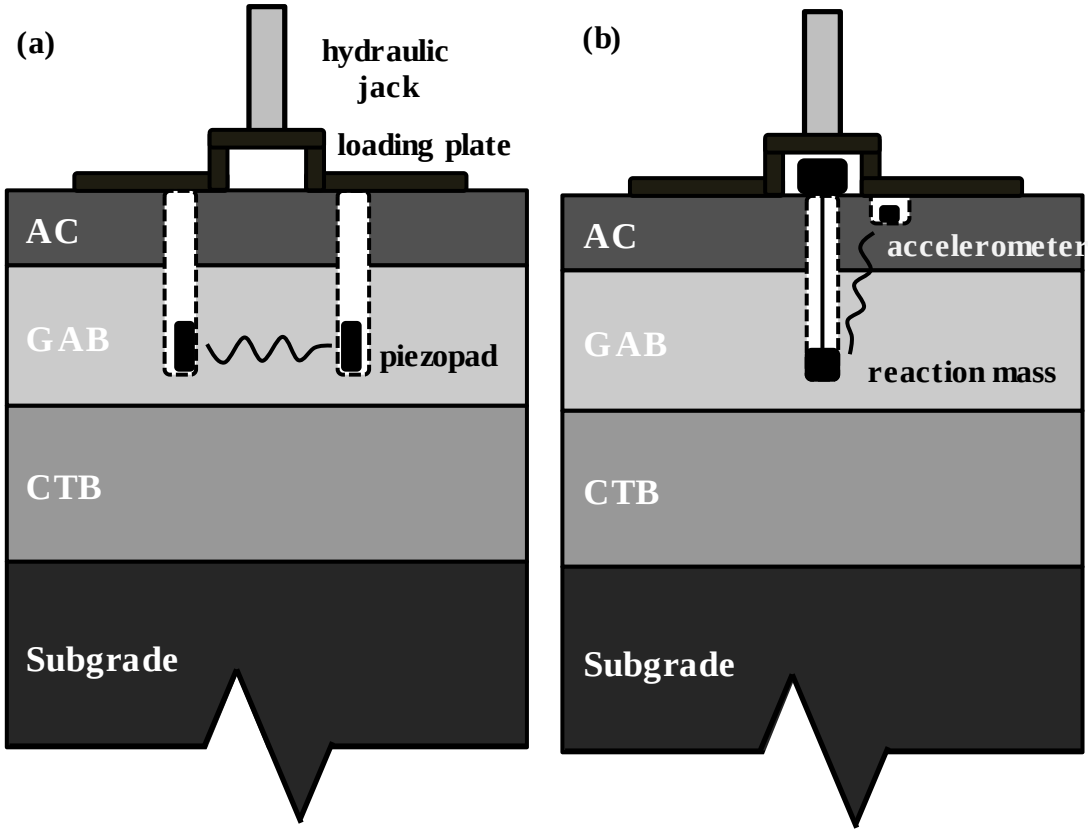

Figure 5.1 Schematic representation (not to scale) of (a) the crosshole and (b) the uphole test designed to measure the directional stress-dependent stiffness of the granular base. The contact stress was applied using a hydraulic jack acting on a circular plate.

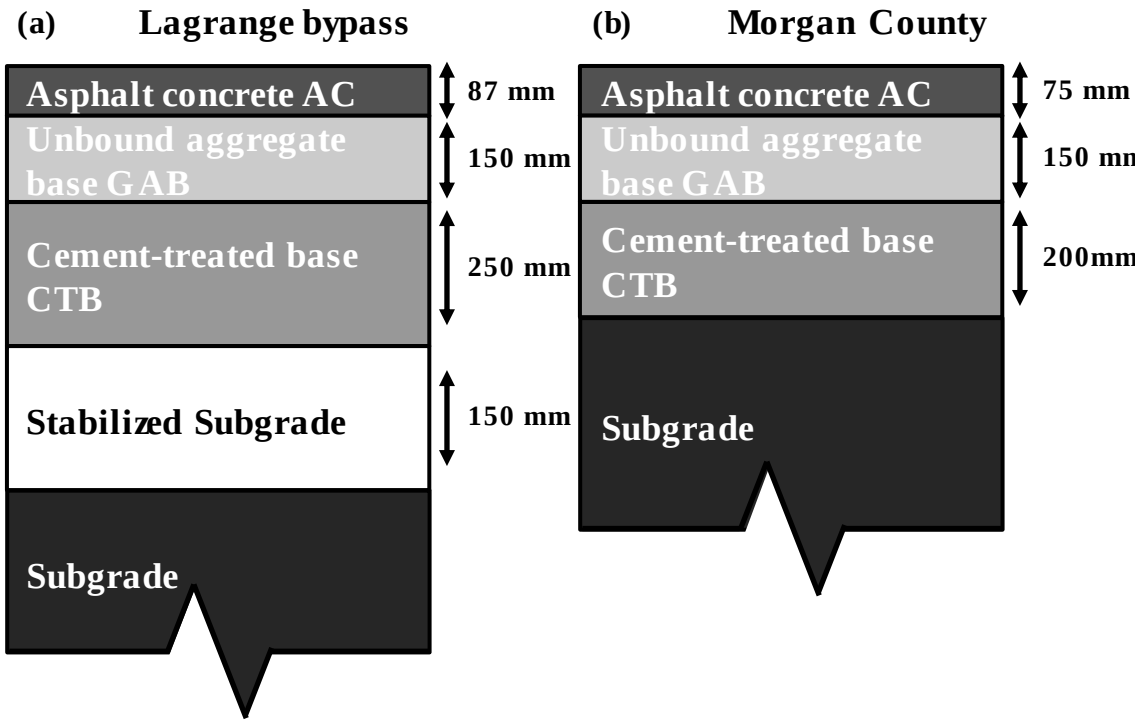

Figure 5.2 Inverted base pavement structures tested in this study: (a) Lagrange, GA and (b) Morgan county haul road in Buckhead, GA.

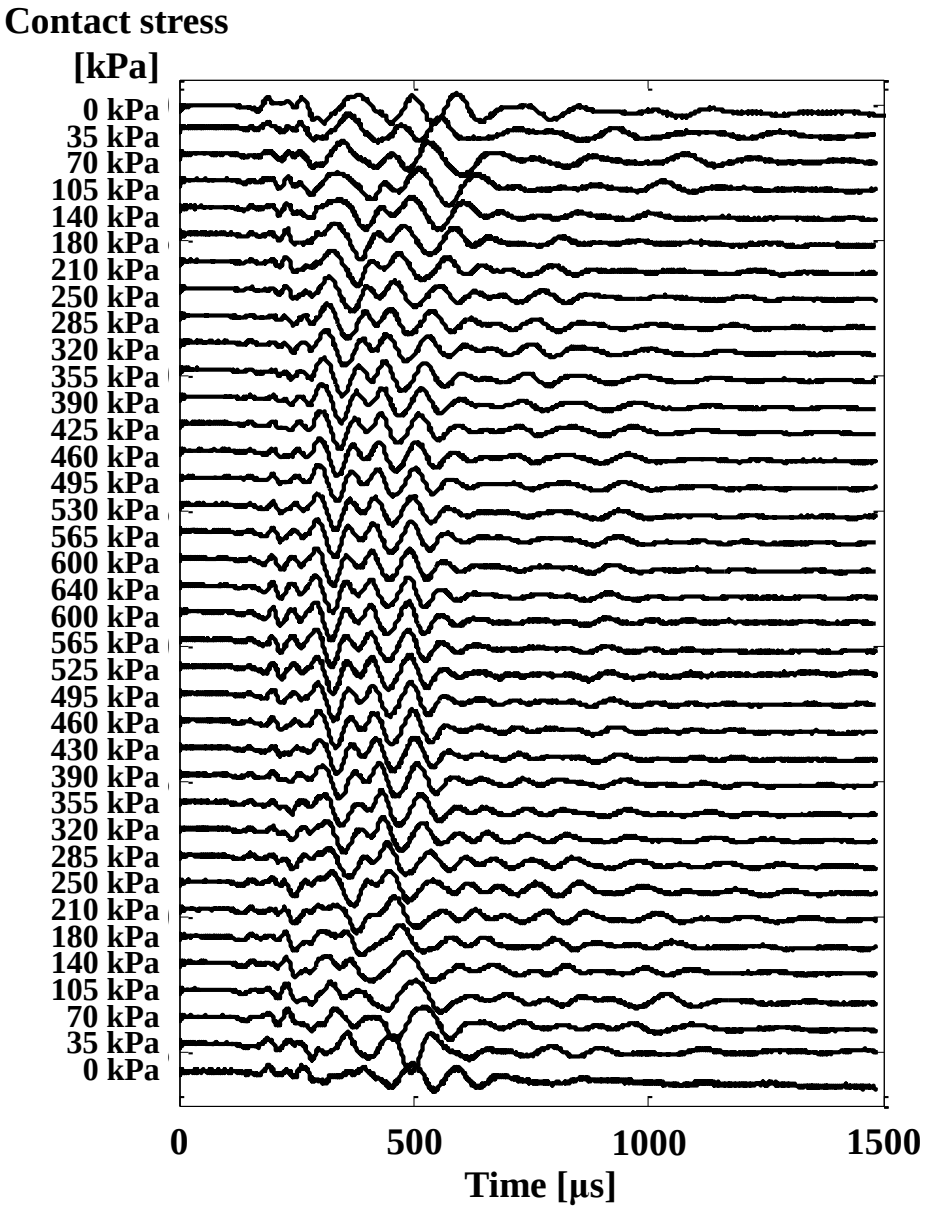

Figure 5.3. Typical signal cascades for the crosshole test (Morgan County test). The applied contact stress is noted on the left.

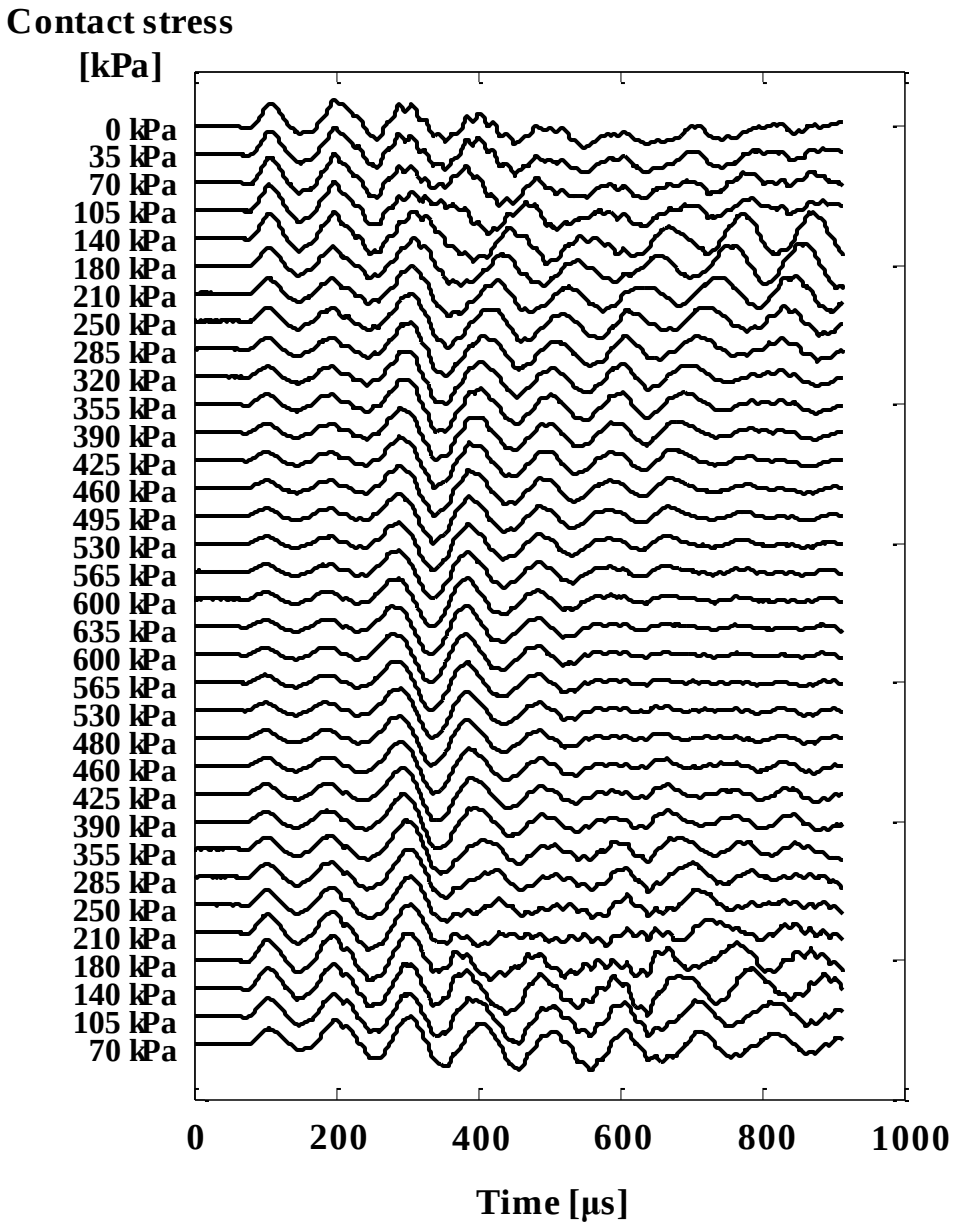

Figure 5.4. Typical signal cascades for the uphole test (Lagrange Test). The applied contact stress is noted on the left.

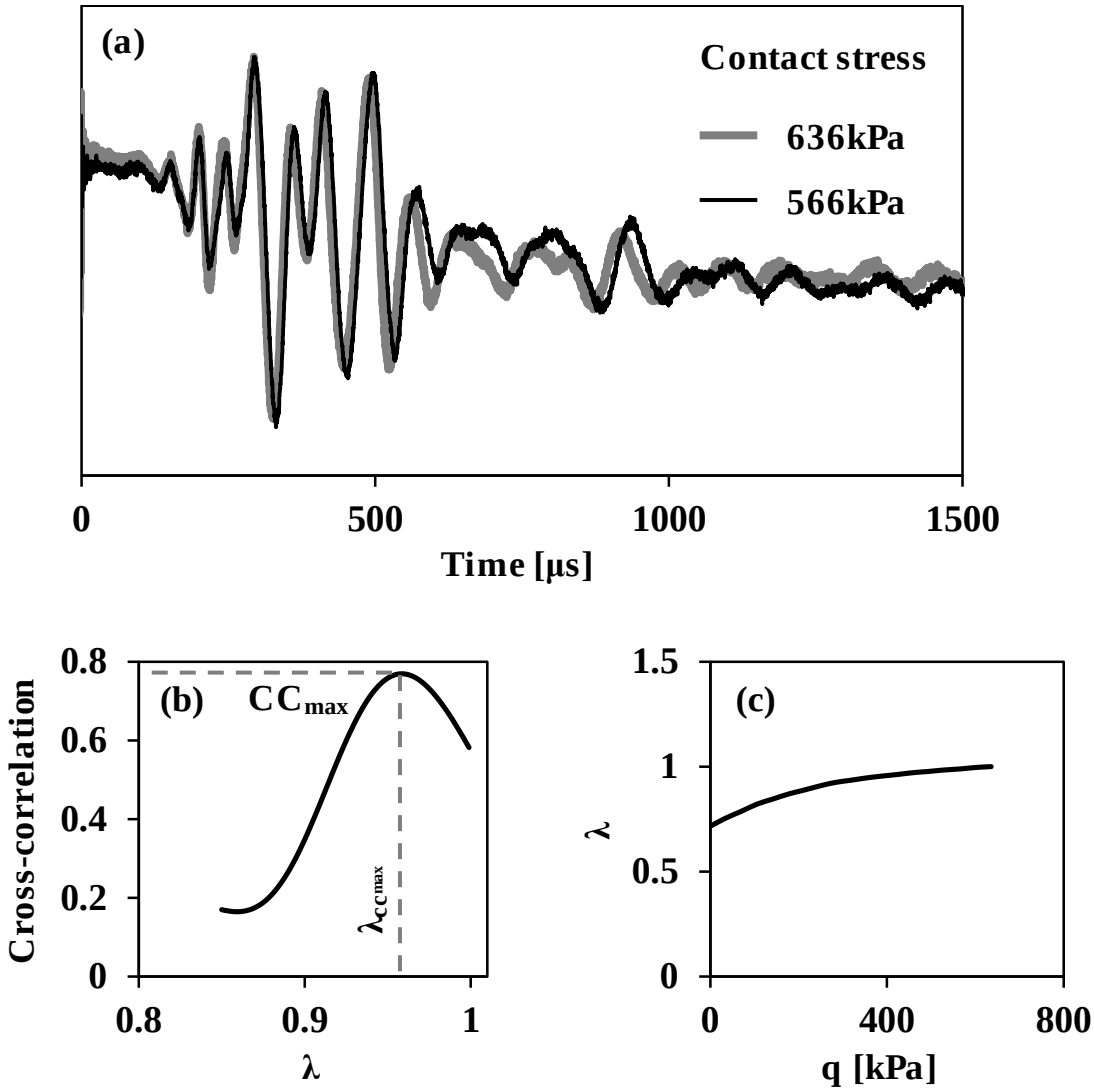

Figure 5.5. CODA analysis: determination of the stretch coefficient. (a) Comparison between two signals (crosshole-Morgan county dataset). (b) cross correlation CC versus the stretching coefficient λ for the two signals shown above and (c) stretching coefficient values for the crosshole signal in the Morgan county test versus applied contact stress q.

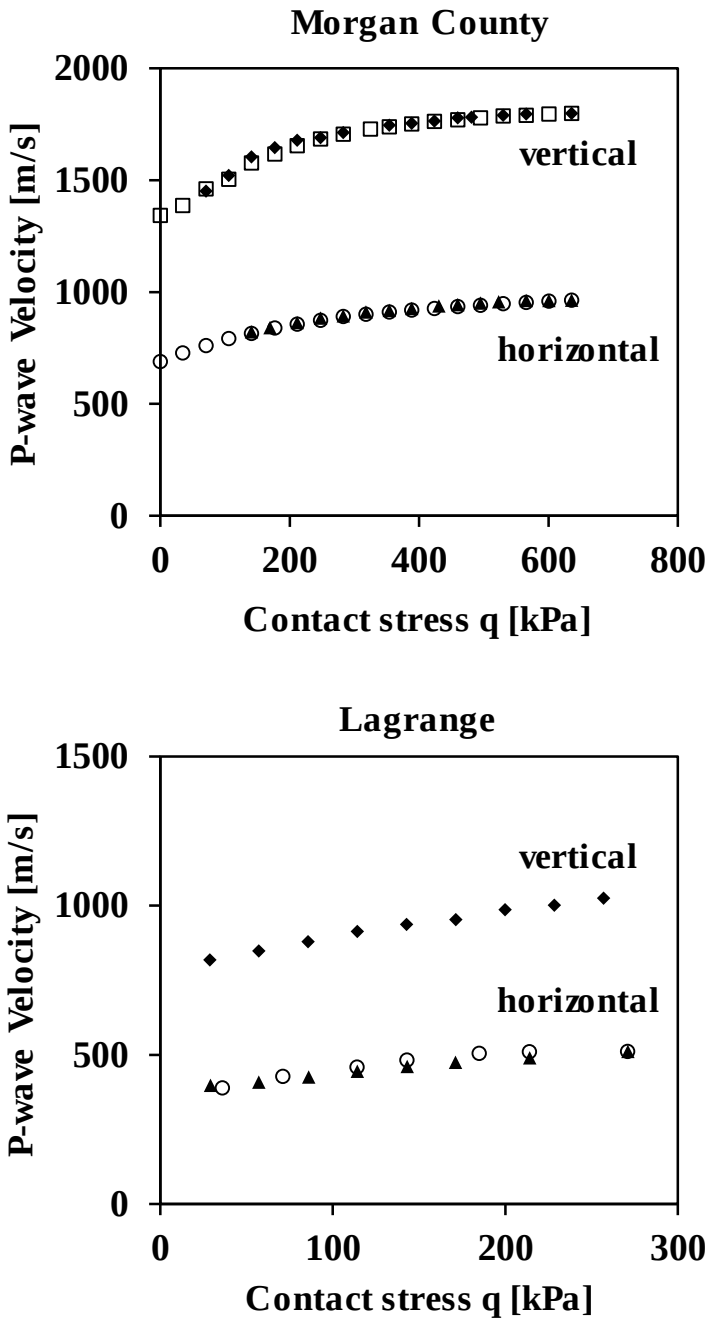

Figure 5.6. Vertical and horizontal P-wave velocity versus contact stress q at the two test sites. Filled and empty points display loading and unloading respectively.

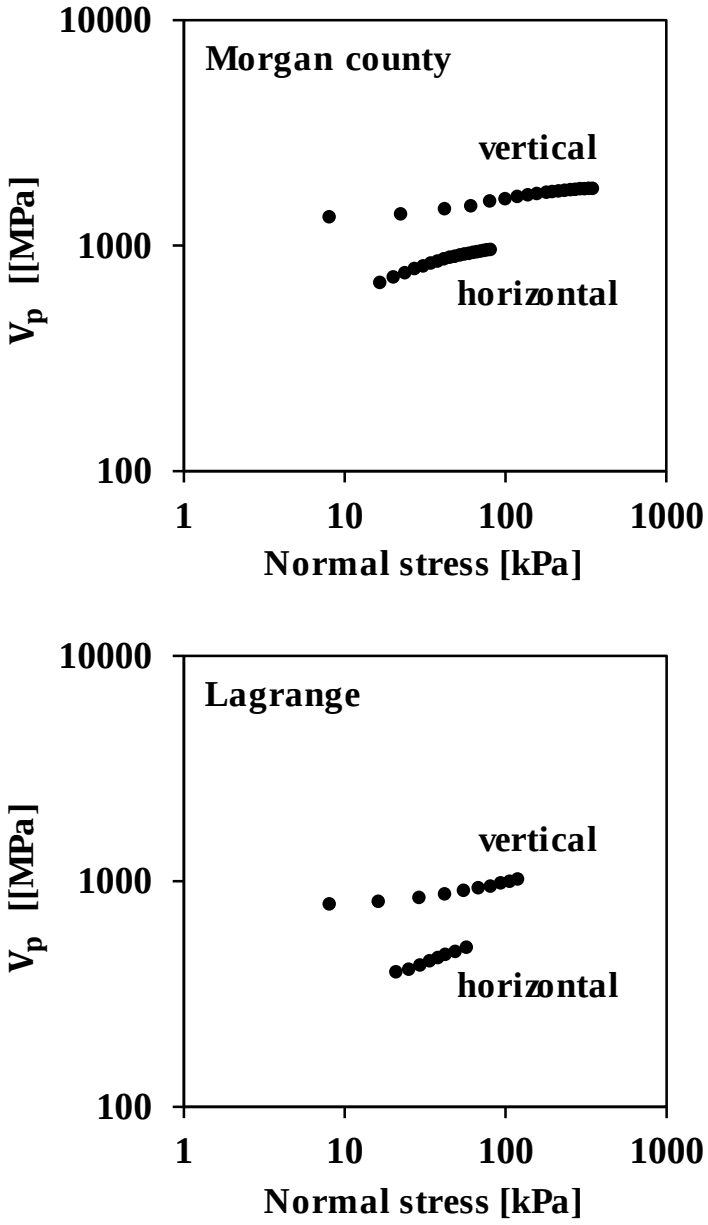

Figure 5.7. Vertical and horizontal P-wave velocity V_p versus calculated normal stress in the direction of wave propagation for the two field tests.

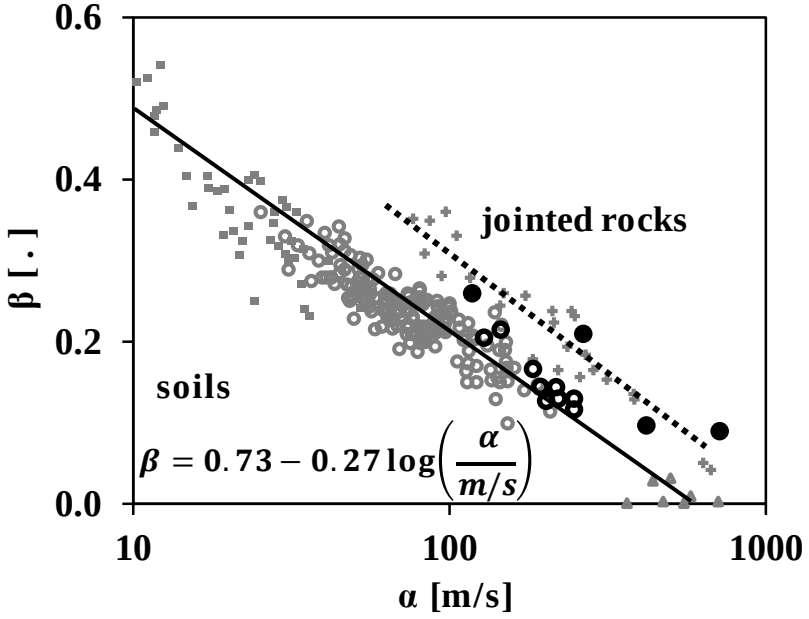

Figure 5.8. Velocity parameters: β-exponent versus α-factor for the two tests shown as solid black points. Hollow black circles are laboratory compacted GAB samples (Chapter 4). Grey data points are data from the literature (replotted from Cha and Santamarina 2014).

CHAPTER 6
PERFORMANCE OF INVERTED BASE PAVEMENTS WITH THIN ASPHALT SURFACE LAYERS

6.1 Introduction

Inverted base pavements are flexible pavements where the graded aggregate base GAB is placed between a cement-treated base CTB and an asphalt concrete surface layer AC. Inverted base pavements have been used in other countries, particularly South Africa (Jooste and Sampson 2005). Experience with full-scale inverted base pavements in the US remains limited to a few cases (Cortes and Santamarina 2013; Terrell et al. 2003).

Mechanistic-empirical design methods can accommodate all types of pavements (NCHRP 2004). Mechanistic analyses can provide insight related to the capacity of a pavement structure as well as its response to traffic loads. Such capabilities are needed for the analysis of unconventional pavement designs, such as inverted base pavements. However, state DOTs have been slow to adopt new design methods due to lack of experience and calibration issues (Li et al. 2010; Li et al. 2012; Tarefder and Rodriguez-Ruiz 2013).

In this study, the behavior of inverted base pavements is analyzed through a mechanistic pavement response model built on the FE code ABAQUS. A robust nonlinear anisotropic constitutive model is used to model the behavior of the granular base. Different inverted pavement designs are simulated to investigate the interaction between different layers and the effect of combined normal and shear contact forces.

6.2 Previous Studies

Early mechanistic analyses of pavement structures made use of closed-form solutions for multi-layer elastic systems (Burmister 1945; Burmister et al. 1943). Computers allowed more complex material models (Kenis 1978; Wardle 1977), while the first finite-element codes for pavement analysis also emerged (Duncan et al. 1968). Several computer programs have been created since (Barksdale et al. 1989; Brown and Pappin 1981; Park and Lytton 2004; Raad and Figueroa 1980; Tutumluer and Barksdale 1995). Recent advances in pavement modeling include anisotropic models of granular bases, stress-dependent stiffness of the subgrade and the granular base and simulation of realistic tire-pavement contact stress (Al-Qadi et al. 2010; Liu and Shalaby 2013).

In this study, the finite-element code ABAQUS is used together with user-defined material model subroutines (Cortes et al. 2012; Kim et al. 2009; Yoo et al. 2006).

6.3 Constitutive Model

Most numerical simulations capture the behavior of the granular layers and subgrade through the resilient modulus M_r (Al-Qadi et al. 2010; Tutumluer and Barksdale 1995; Yoo et al. 2006). Several models have been developed to predict resilient modulus as a function of the state of stress during traffic loading (Brown 1996; Hicks and Monismith 1971; Uzan 1985). In this work a tangent stiffness formulation is used to model the resilient stress-dependent stiffness of granular bases. The constitutive model used for the GAB captures the small to intermediate strain deformational behavior of granular bases using a hyperbolic formulation that accounts for stress-hardening, shear-softening and both fabric and stress-induced anisotropy.

6.3.1 Stress-Dependent Stiffness

The stress-strain behavior of granular materials under traffic loading generally follows a hyperbolic trend. Thus it can be characterized by two parameters, namely the initial small-strain stiffness E_0, and the ultimate load capacity q_u. The initial stiffness E_0 is herein calculated from P-wave propagation and depends on the stress in the direction of propagation, as shown in Chapter 3 (Kopperman et al. 1982).

Granular bases exhibit inherent anisotropy due to grain shape and compaction as well as stress-induced anisotropy in response to external loads (Chapter 3). Inspired by Hertzian behavior, a simple model to predict E_0 in direction i is:

$$E_0^x = c_1^x \cdot \left(\frac{\sigma_{xx}}{kPa}\right)^{c_2} \quad (1)$$

$$E_0^y = c_1^y \cdot \left(\frac{\sigma_{yy}}{kPa}\right)^{c_2} \quad (2)$$

$$E_0^z = c_1^z \cdot \left(\frac{\sigma_{zz}}{kPa}\right)^{c_2} \quad (3)$$

where σ_{ii} is the normal stress in the direction i and c_1^i, c_2 are regression coefficients. This model can capture both inherent and stress-induced anisotropy.

An orthotropic linear elastic formulation requires 9 independent parameters; however the model can be simplified by making behavior-guided assumptions that do not diminish accuracy. Following elasticity, the shear stiffness G_{ij} is given by the following formula:

$$G_{ij} = \frac{0.5(E_i + E_j)}{2.2} \quad (4)$$

Equation 4 implies that Poisson's ratio at very small strains is v=0.1.

6.3.2 Strain-dependent Modulus Degradation

The small-strain stiffness accounts for elastic deformation at grain contacts and is a constant fabric parameter (Hardin 1978). Deformation due to contact sliding, particle crushing and rearrangement above the elastic threshold strain are not captured in E_0 (Jang and Frost 2000; Rothenburg and Kruyt 2004). On the other hand, the tangent stiffness E_{tan} required for the incremental finite-element formulation must track fabric evolution and it is estimated from the small-strain stiffness E_0 using a hyperbolic model (Duncan and Chang 1970):

$$\frac{E_{tan}}{E_0} = \frac{1}{(1+\frac{\varepsilon}{\varepsilon_r})^2} \tag{5}$$

where E_{tan} is the slope of the stress-strain trend, ε is the strain at the current stress and the reference strain $\varepsilon_r = q_u/E_0$. Equation (2) can be written in terms of stress as:

$$\frac{E_{tan}}{E_0} = (1-\frac{q}{q_u})^2 \tag{6}$$

where q is the deviatoric stress:

$$q = \frac{1}{\sqrt{2}} \cdot \sqrt{(\sigma_1-\sigma_2)^2+(\sigma_1-\sigma_3)^2+(\sigma_2-\sigma_3)^2} \tag{7}$$

Materials exhibit different rates of softening during shear. Thus, the hyperbolic model is modified as (van Niekerk et al. 2002):

$$\frac{E_{tan}}{E_0} = 1-\left(\frac{q}{q_u}\right)^{c_3} \tag{8}$$

where c_3 is a fitting coefficient. High values of c_3 correspond to brittle materials which exhibit sudden failure while low values correspond to materials that fail gradually. The

shear strength q_u is assumed to follow a Coulomb friction law; for numerical stability the conical Drucker-Prager failure criterion is adopted:

$$q_u = D + M \cdot q \tag{9}$$

where D and M are functions of the cohesion c and friction angle φ:

$$D = c \cdot \frac{6 \cdot \cos\varphi}{3 - \sin\varphi} \tag{10}$$

$$M = \frac{6 \cdot \sin\varphi}{3 - \sin\varphi} \tag{11}$$

The following mechanical constraint applies to the ratios between Young's moduli and Poisson's ratios:

$$\frac{E_i}{E_j} = \frac{v_{ij}}{v_{ji}} \tag{12}$$

where Poisson's ratio $v_{xy} = v_{zy} = v_{zx} = 0.35$.

6.3.3 Numerical Implementation

The constitutive model defined by equations (1) through (12) was implemented in an explicit formulation using a user-defined subroutine in ABAQUS. The flowchart of the subroutine is shown in **Figure 6.1**.

6.3.4 Calibration – Verification

True triaxial tests results reported in Chapter 3 are used to calibrate the model (**figure 6.2a**). The small-strain stiffness is measured using wave propagation in both the horizontal and vertical directions. After calibrating the small-strain stiffness-stress evolution (equations 1, 2 and 3), the modulus reduction curve can be calibrated from triaxial test data (Equation 8). Data gathered at strain rates similar to traffic loading are

preferred; Results show that granular materials exhibit higher strength at large strain rates (Garg and Thompson 1997; Tutumluer 2013).

Calibrated material parameters are shown in **Table 6.1**. Following calibration, the constitutive model is verified by comparing the measured behavior to the one predicted by a 1-element model built in ABAQUS. Numerical results agree with experimental data (**figure 6.2b**).

6.4 Finite Element Model

6.4.1 Geometry – Finite Element Mesh

The geometry of a typical inverted base pavement is shown in **figure 6.3**. Several inverted base pavement designs are generated by varying the thickness of different layers. The circular loaded area at the top has a diameter of 300mm to simulate an ESAL. The model boundaries are placed far away to minimize their effect on the model response (Cortes et al. 2012).

6.4.2 Material Behavior

Asphalt concrete: The behavior of the asphalt concrete layer is influenced by temperature, rate and duration of loading, and load amplitude (Abbas et al. 2004). In this analysis a simple linear elastic isotropic behavior of the asphalt concrete is assumed, which is a reasonable approximation for quasi-static analyses at constant temperature (stiffness selected for 25C°).

Cement-treated base: The cement-treated base behavior evolves during the life of the pavement. Initially, the material behaves as a high stiffness elastoplastic medium (Lim

and Zollinger 2003). The effective stiffness is reduced as cracking takes place; eventually the CTB behaves as a granular medium. Assuming that strains remain within the elastic range, which is the purpose of this design, a linear elastic model can be adopted for the CTB.

Subgrade: Typically, fine-grained soils exhibit softening behavior at increasing stress levels (Uzan 1985). However, one of the objectives of the pavement structure is to minimize stresses transferred to the subgrade. Thus the subgrade behavior is approximated using a secant linear elastic model for a certain strain level.

Table 6.1 summarizes the material parameters used for all pavement layers.

6.4.3 Compaction-Induced Residual Stresses

During compaction, the graded aggregate base is subjected to large vertical stress which in turn produces comparable horizontal stresses (Uzan 1985). Upon removal of the compaction load, part of the horizontal stress remains locked in. The effect of compaction-induced residual stresses can be quite significant on the stress-dependent stiffness at small applied loads while it prevents numerical instabilities. Compaction-induced stresses are taken into consideration by assuming that the granular base reaches active failure during compaction while it moves towards passive failure after removal of the compaction load (Duncan and Seed 1986; Filz 1996). The geostatic horizontal stress σ_{h0} in the GAB is a function of the vertical geostatic stress σ_{v0}:

$$\sigma_{h0} = K_c \cdot \sigma_{v0} \tag{13}$$

where the coefficient $K_c = 6$ assumes a mobilized friction angle of 45°. The vertical geostatic stress σ_{v0} is:

$$\sigma_{v0} = \int_0^z \gamma dz \tag{14}$$

where γ is the unit weight. In inverted base pavements, the granular layer is placed close to the surface and residual compaction stress is small.

6.5 Results

6.5.1 Stress Distribution

Figure 6.4 shows vertical and horizontal stress distributions along the load centerline for pavements of different layer thicknesses. The stiff and thick AC and CTB layers deform in bending and develop tensile horizontal stress at the bottom of the layer. The frictional GAB cannot mobilize tension; thus, horizontal stress in the graded aggregate base is compressive everywhere as a result of the lateral constrain excited by the CTB. The stress change caused in the subgrade is minimal compared to the applied stress in all cases. Changing the layer thicknesses results in the following changes in the stress distribution:

- *CTB*: decreasing the CTB thickness increases bending in the CTB and both compressive stress at the top and tensile stress at the bottom. Other layers are not largely affected.
- *GAB*: Increasing the thickness of the GAB exacerbates the bending of the AC and increases the bending stresses. On the other hand, the GAB acts as a cushion for the CTB and decreases bending stresses in that layer.
- *AC*: Decreasing the thickness of the AC relieves most tensile stress in the asphalt concrete under the load centerline. Bending action is minimized and

the asphalt layer transitions from a beam to a membrane-like deformation. Furthermore, the GAB sustains greater horizontal and vertical stress.

6.5.2 Effect of AC Thickness: Beam to Membrane Transformation

Figure 6.5 shows the horizontal stress along the top and bottom of the asphalt concrete layer, under the wheel load and for different asphalt concrete thickness. The graded aggregate base thickness is 200mm and the cement treated base thickness is 300mm in both cases. The maximum tensile stress is roughly the same even though the AC layer thickness is reduced by a factor of four. The horizontal stress in the 100mm AC pavement is typical of a layer that deforms in bending as a double-fixed beam. The maximum tensile stress occurs at the bottom of the layer directly below the load centerline. Some tensile stress also develops at the top of the layer near the load edges. Horizontal stress for the 25mm AC layer follows a different pattern. The maximum tensile stress occurs very close to the edge of the load and suggests strong shear at the edges. This effect is aggravated by the uniform load assumption. The transition from compression to tension takes place near the load edge.

6.5.3 Effect of GAB Thickness

The mobilized stiffness of the graded aggregate base reflects the external load. Stiffness contours for different layer thicknesses beneath a 650kPa vertical load are shown in **Figure 6.6**. In all cases the asphalt concrete thickness is 250mm and the cement-treated base thickness is 300mm. Vertical stiffness is considerably higher under the wheel load than in the far field. The proximity of the graded aggregate base to the

load, along with the stiff reaction provided by the cement-treated base, create an effective confinement that increases stiffness.

6.5.4 GAB Stiffness Anisotropy

The extent of stiffness anisotropy that develops in the GAB is shown in **figure 6.7**. Contours of stiffness anisotropy E_v/E_h are plotted for asphalt concrete thickness equal to 25mm, 50mm and 100mm. In all cases, t_{GAB}=250mm and t_{CTB}=300mm. The stress sensitivity of the GAB has a large effect on the evolution of anisotropy. When the AC thickness is small, the granular base is exposed to greater vertical stress and develops a higher vertical stiffness. On the other hand, the asphalt layer distributes the vertical stress over a larger area in deep AC pavements, the GAB experiences lower vertical stress and mobilizes lower stiffness.

These results have important implications for characterization and modeling. Deformations are underestimated and critical responses can be unconservative when isotropic stiffness is assumed together with vertically measured stiffness. The opposite will be true when the horizontal stiffness is in combination with an isotropic model.

6.6 Analyses

6.6.1 Stress Along the Wheel Path

The state of stress is different for elements at different points along the wheel path. For granular materials such as the GAB, permanent deformations result from stress rotation and changes in the stress ratio. The stress ratio q/p as well as the intermediate stress ratio $b = (\sigma_2 - \sigma_3)/(\sigma_1 - \sigma_3)$ are plotted along the wheel path in **figure 6.8**. With

the exception of the 25mm AC pavement, the highest stress ratio occurs at the top of the GAB beneath the wheel centerline. Furthermore, the stress conditions change from triaxial extension ($\sigma_2 = \sigma_1 = \sigma_{hor}$) in the far field to triaxial compression under the load centerline ($\sigma_2 = \sigma_3 = \sigma_{hor}$).

6.6.2 Shear Contact Stress

Shear loading along the tire pavement interface develops under rolling conditions, during acceleration and along curves (Wang 2011). The maximum stress that can be mobilized is estimated using a Coulomb friction law:

$$\tau = \mu \cdot \sigma_v \quad (15)$$

where μ is the tire-pavement friction coefficient. The effect of shear stress on the response of inverted base pavements is examined by adding shear stress computed for a friction coefficient μ=1 which is the upper bound for dry asphalt-tire contact (Gustafsson 1997; Muller et al. 2003; Ray 1997).

Figure 6.9 shows the tensile strain along the AC layer for the cases of only vertical load and combined vertical and shear load for two pavements with different AC thicknesses. Contact shear increases tension at the rear end of the load imprint, at the top of the asphalt concrete layer. Under shear load, the benefits of a membrane response in thin AC layers are overruled by the increased tensile strain caused by shear.

6.6.3 Optimization

Figure 6.10 shows the critical pavement response indicators as a function of the AC thickness for different GAB thicknesses. The response of the asphalt concrete layer is not affected by the thickness of the GAB. Both tensile and compressive strains in the AC are

maximized when the thickness of the AC is 50mm (**figure 6.10a and b**); this suggests a transition from beam to membrane deformation pattern. Nevertheless, results for tensile strain cannot be directly related to fatigue cracking. According to the Mechanistic-Empirical Pavement Design Guidelines (MEPDG) fatigue cracking correlations used are a function of layer thickness as well as tensile strain; for the same tensile strain, a 25mm AC layer can withstand almost 10 times the amount of load repetitions compared to a 100mm layer. The potential for economic savings of thin AC layers include lower construction and maintenance costs.

According to the MEDPG, rutting in the GAB is a function of the elastic vertical strain. However, this correlation does not take into consideration fundamental aspects of the behavior of geomaterials under repetitive loading such as the effect of the stress ratio q/p (Pasten et al. 2013). The stress ratio q/p in the GAB is determined by the AC thickness (**figure 6.10c**): thicker AC layers decrease the stress ratio in the GAB considerably as the asphalt surface layer spreads the load over a larger area of the GAB. Also, thick GAB layers tend to develop higher stress ratios when covered by very thin asphalt layers.

The maximum tensile strain in the CTB decreases with an increase in either the GAB or the AC thickness (**figure 6.10e)**. A 25mm asphalt concrete on top of a 300mm GAB is equivalent to a 100mm asphalt concrete layer over a 150mm thick GAB.

The subgrade compressive strain decreases with AC thickness (**figure 6.10d**) but is mostly affected by the thickness of the GAB and CTB (not shown). This is attributed to their ability to redistribute the load.

6.7 Conclusions

A numerical 3D finite-element model is used to study inverted base pavements using a stress-dependent constitutive model to adequately describe the behavior of the graded aggregate base. The main conclusions from this study follow:

- Stress redistribution in inverted base pavements is markedly different from conventional pavements due to the stiffness contrast between subsequent layers.
- Thin asphalt concrete layers deform as membranes rather than beam elements. The tensile strain decreases at the bottom of the layer, but it increases at the edges of the load, which signifies the development of shear.
- There are marked changes in the stiffness of the GAB layer during the application of traffic loading due to its proximity to the load.
- The state of stress in the GAB changes noticeably along the wheel path. The stress ratio is higher for elements directly below the load and stress rotation takes place along the wheel path.
- Shear contact stresses due to braking or cornering can have detrimental effects to the condition of the asphalt concrete surface layer, particularly for thin AC layers.
- While the interaction between different layers requires a thorough mechanistic analysis, it is clear that thin asphalt layers can perform as well as thicker layers as long as proper adjustments in the thickness of the GAB are implemented.

Table 6.1. Material parameters used for the finite-element model.

GAB		
Stiffness Parameters	c_1^z (MPa)	130
	c_1^x (MPa)	90
	c_1^y (MPa)	90
	c_2	0.45
	c_3	0.15
Poisson's ratio	ν_{xy}	0.35
	ν_{zy}	0.35
	ν_{zx}	0.35
Strength parameters	c (kPa)	15
	φ	57°

	AC	CTB	SG
Young's Modulus E	2 GPa	10 GPa	50 MPa
Poisson's Ratio	0.35	0.2	0.2

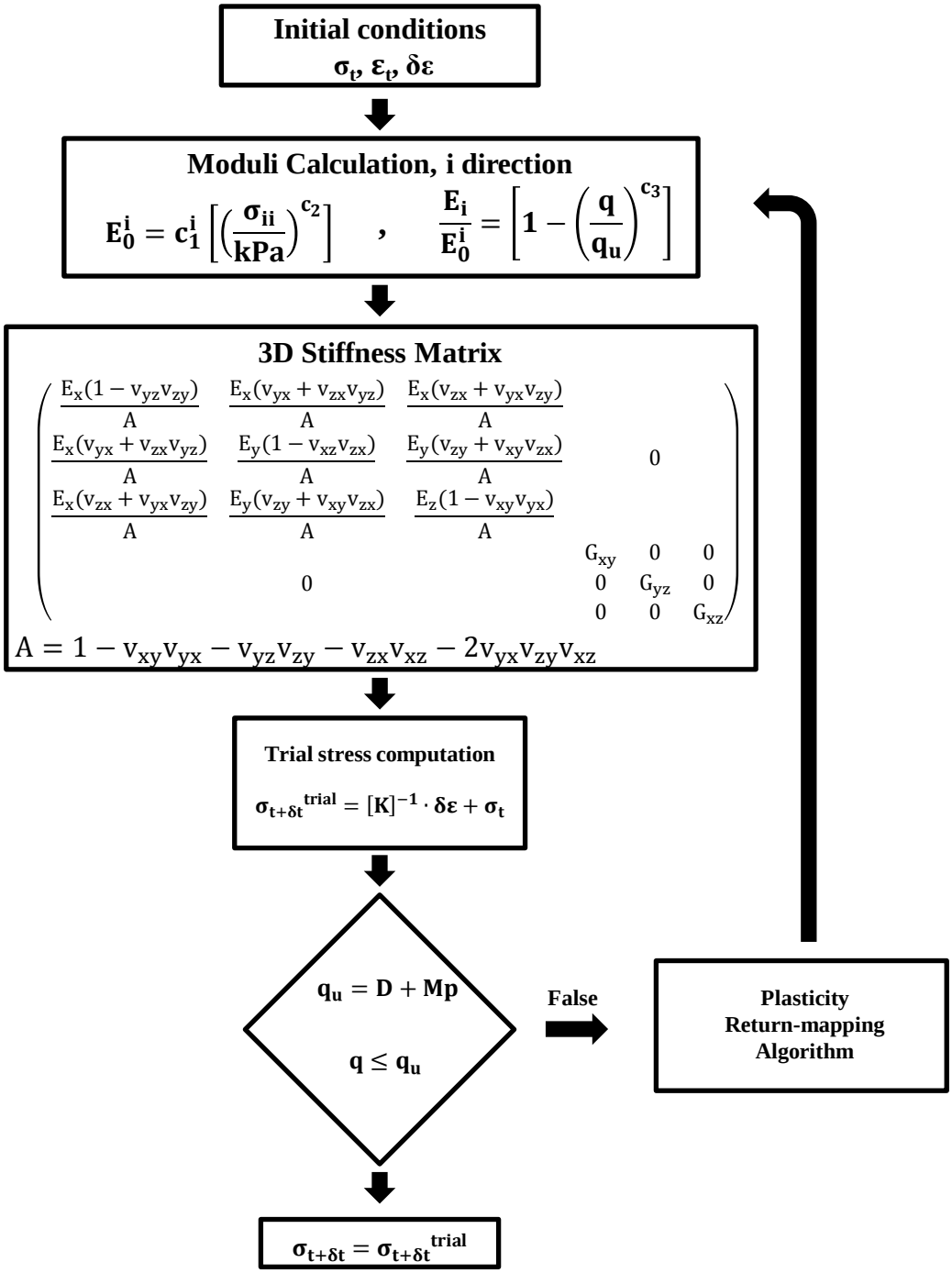

Figure 6.1. Flowchart for the user subroutine implemented in ABAQUS to model the behavior of unbound aggregate base layer.

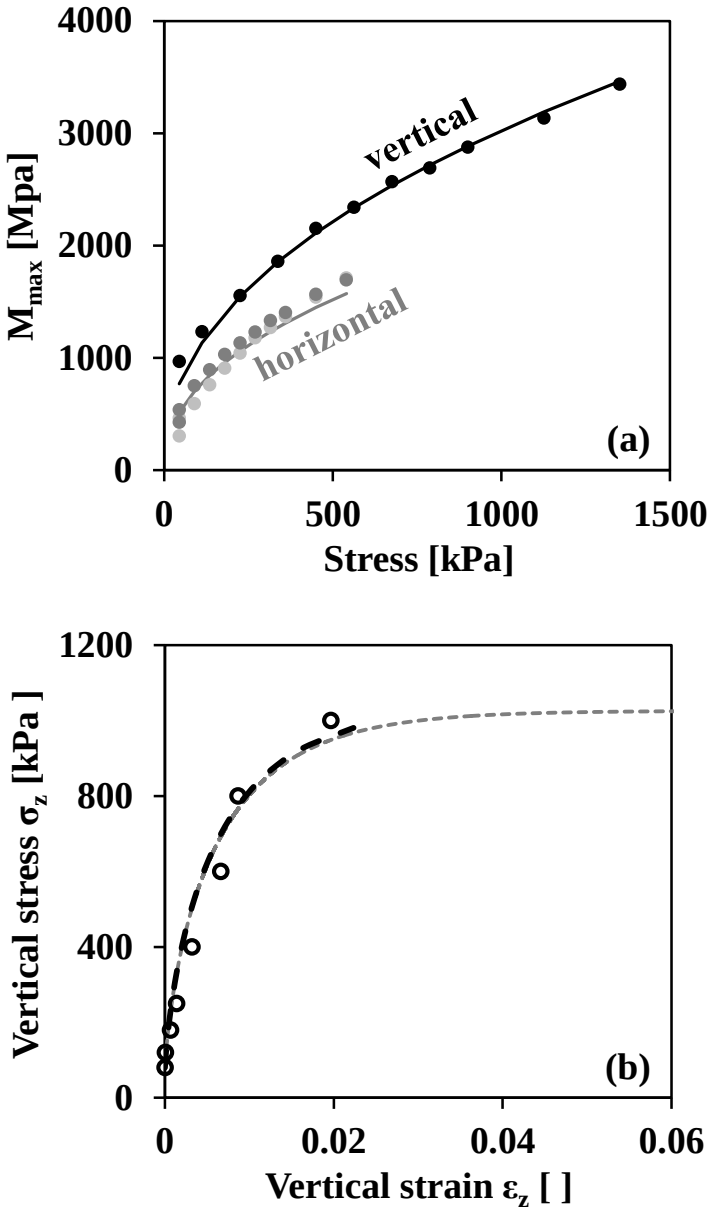

Figure 6.2. Calibration procedure. (a) small-strain constrained modulus M_{max} versus stress inthe direction of P-wave propagation for horizontal and vertical wave propagation. Dots are recorded data while the line is fitted power equation. (b) Stress-strain response; dots are data from triaxial test, the grey line is the stress-strain curve resulting from calibration and the black line is the stress-strain from the 1-element verification model simulated in ABAQUS.

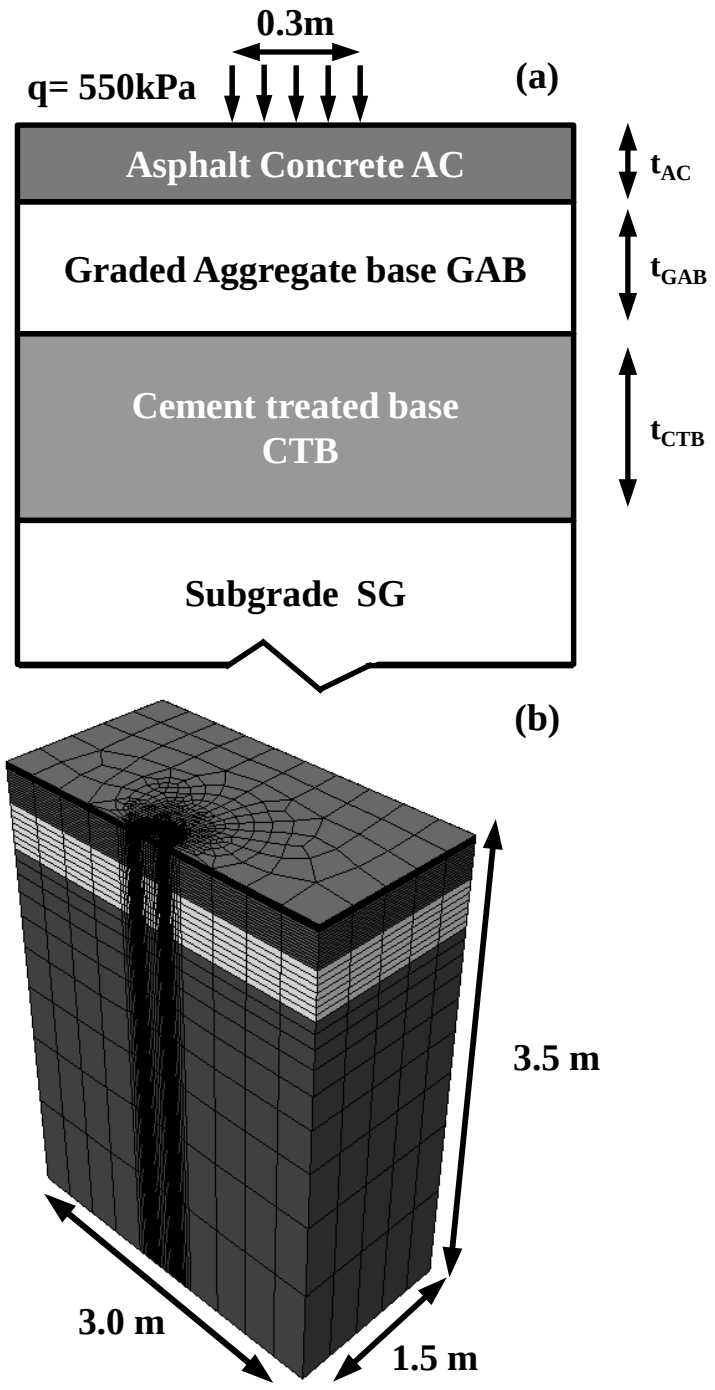

Figure 6.3. Numerical model. (a) Illustration a typical inverted base pavement analyzed in this study. (b) Finite-element model used for numerical simulations.

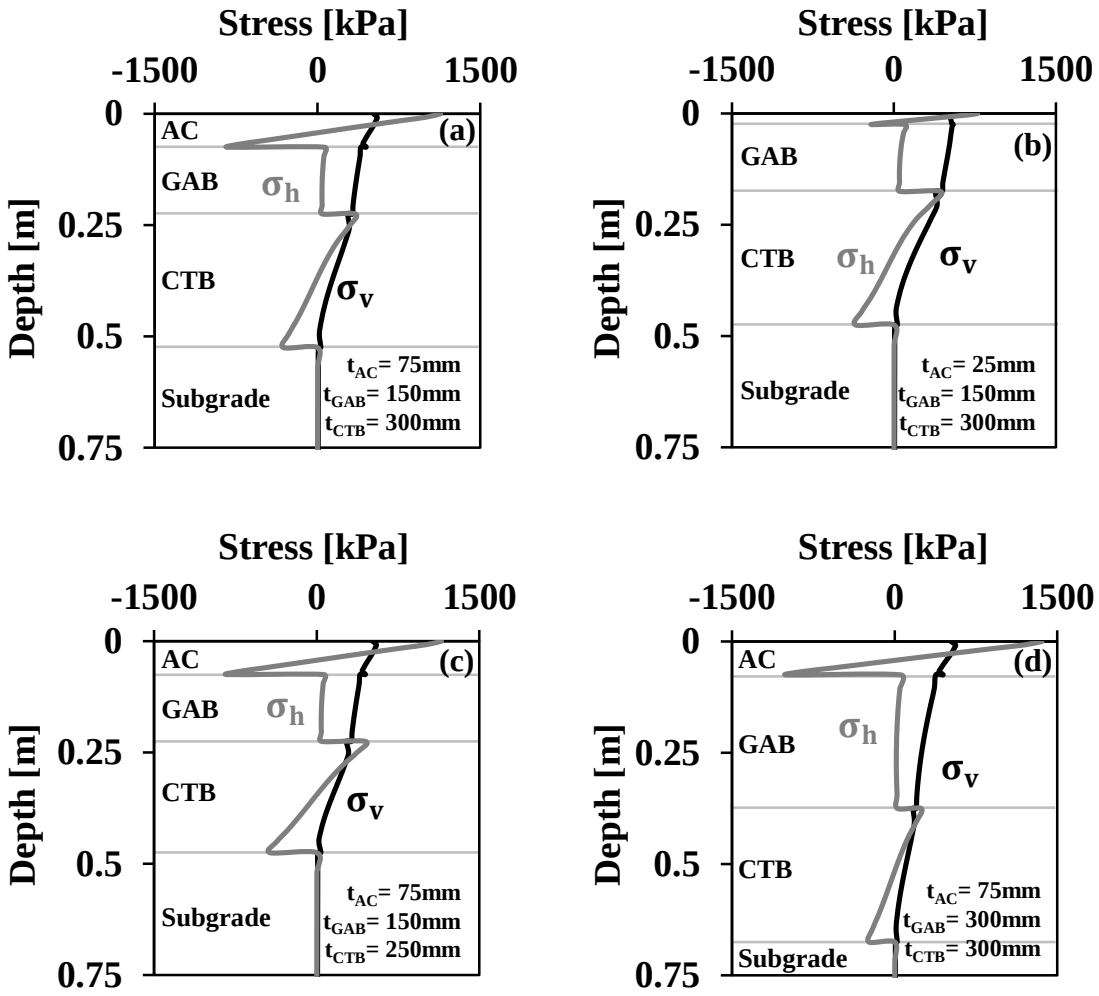

Figure 6.4. Vertical stress σ_v and horizontal stress σ_h distribution versus depth under the load centerline for different layer thicknesses.

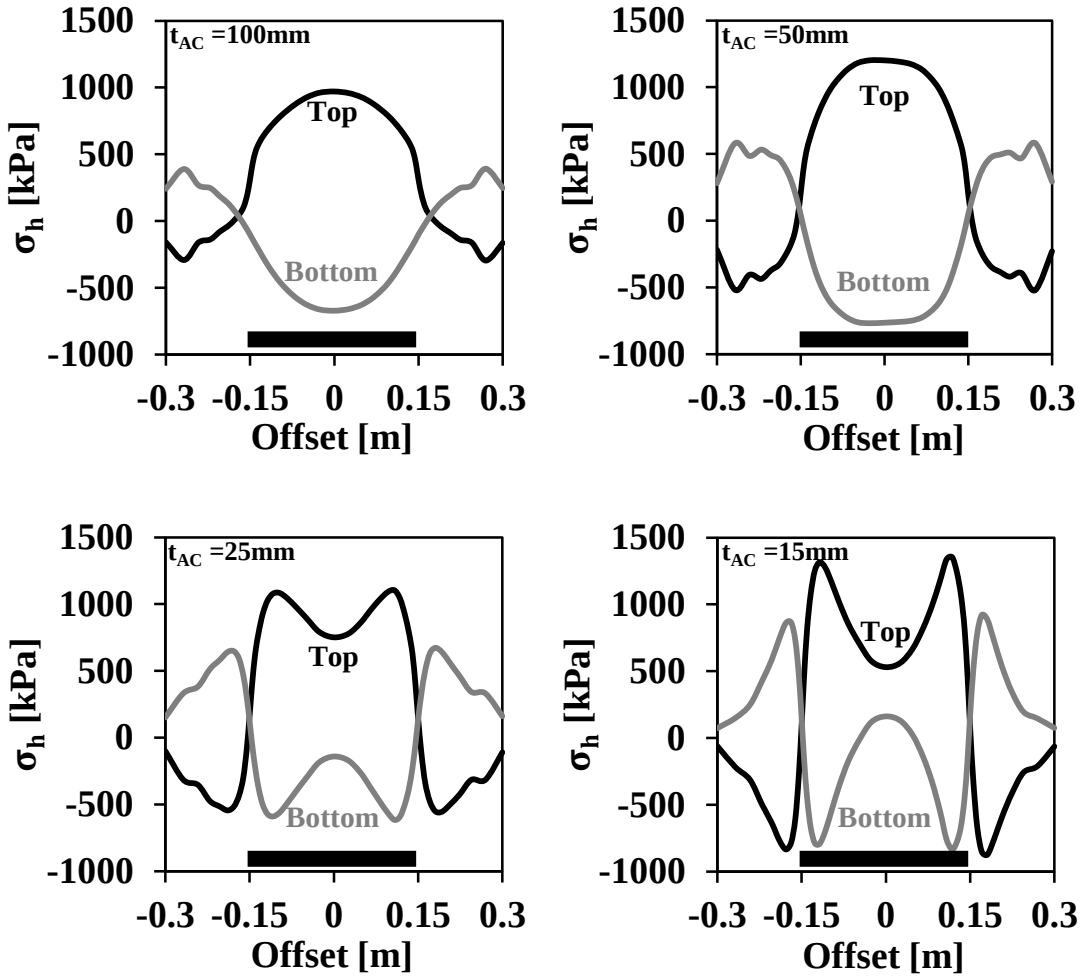

Figure 6.5. Horizontal stress σ_h along the top and bottom of the asphalt concrete layer under the wheel load and for different asphalt concrete thickness.
Note: The graded aggregate base thickness is 150mm and cement treated base thickness is 250mm in all cases. The black horizontal line shows the width of the tire imprint.

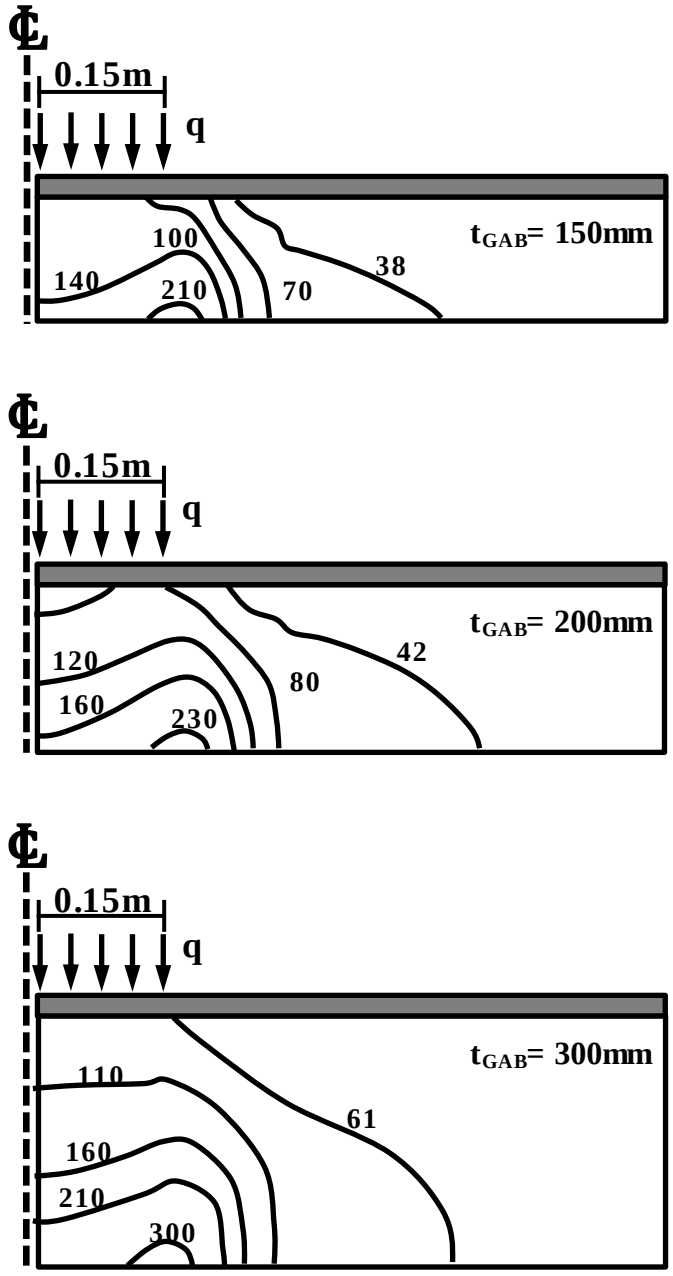

Figure 6.6. Graded aggregate base stiffness contours [MPa] under the wheel load, for different graded aggregate base thickness.
Note: t_{AC}= 50mm and t_{CTB}= 300mm. The applied load is q= 550kPa.

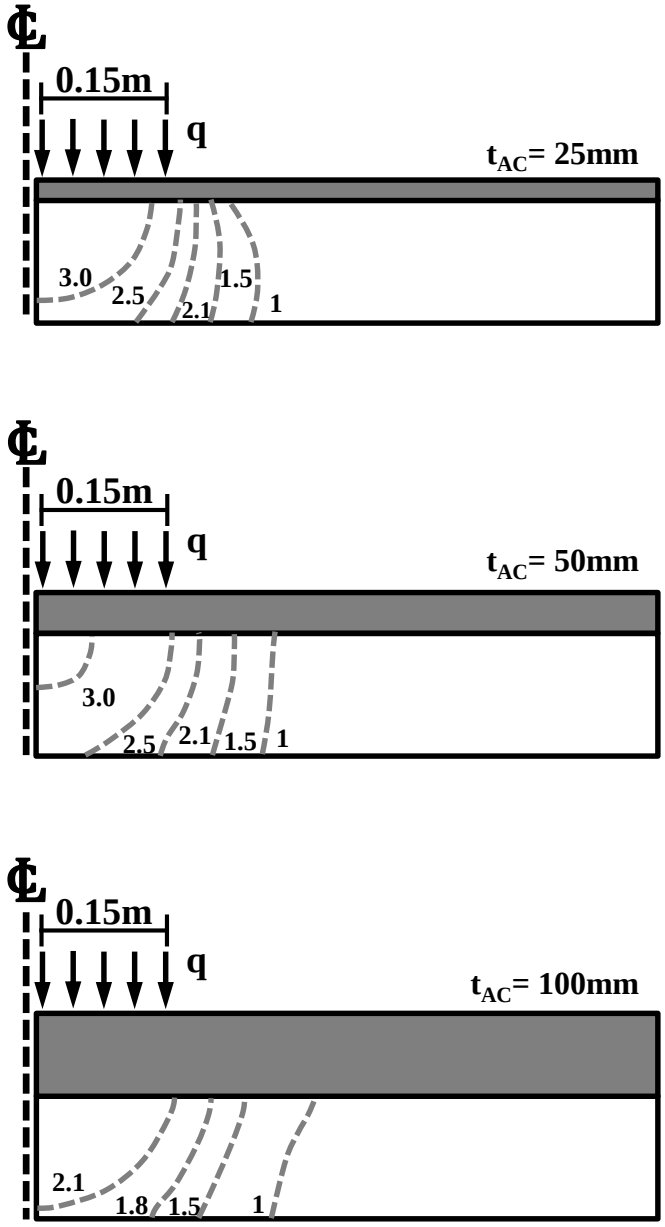

Figure 6.7. GAB stiffness anisotropy E_{vert}/E_{hor} contours under wheel loading for different asphalt concrete thickness.
Note: t_{GAB}= 150mm and t_{CTB}= 300mm. The applied load is q= 550kPa.

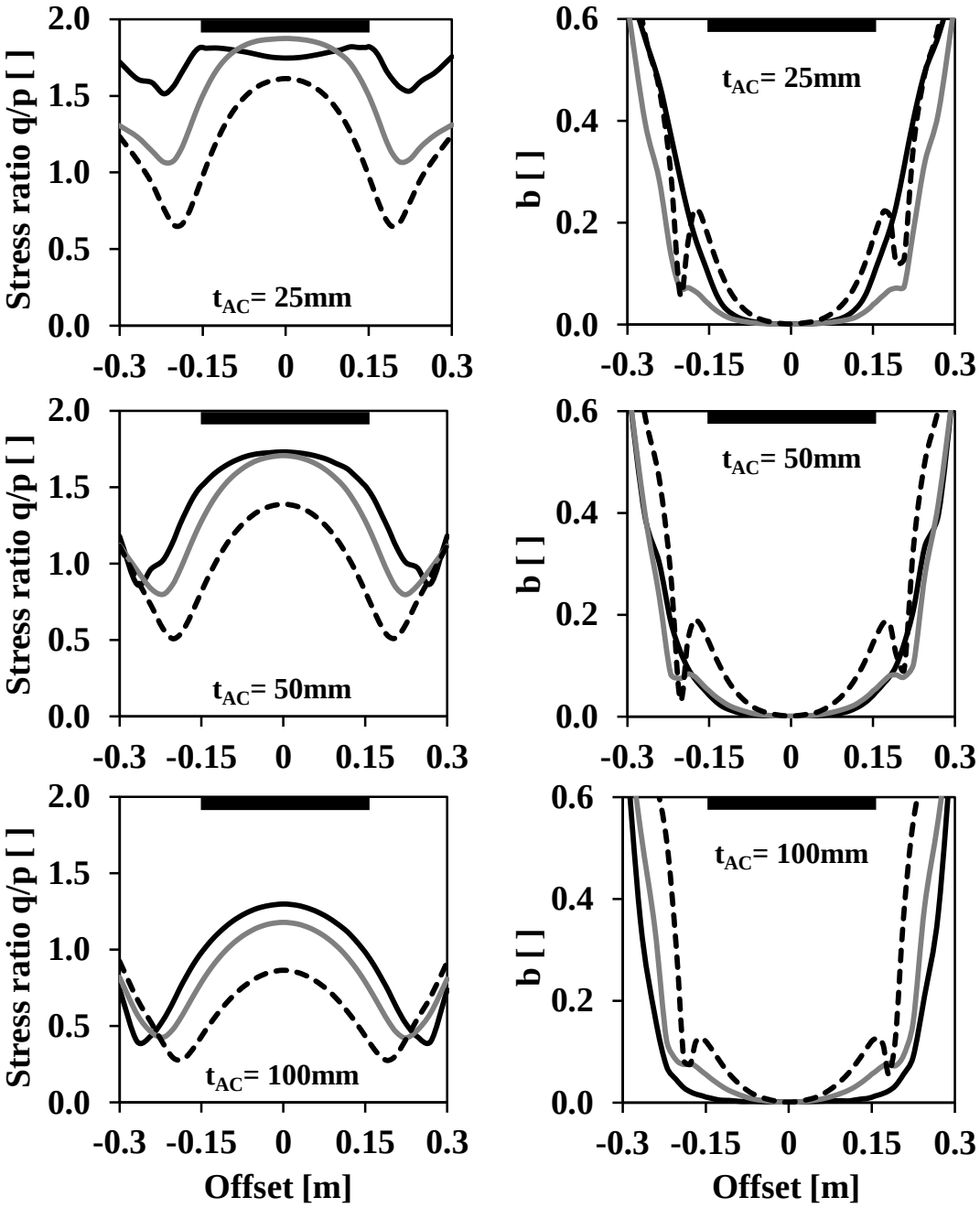

Figure 6.8. Stress along the wheel path. (a) Stress ratio q/p and (b) intermediate stress ratio b in the GAB plotted against offset from the centerline for different asphalt thickness. The black, grey and dashed lines correspond to the top, half-depth and bottom of the GAB respectively. **Note:** t_{GAB}= 150mm and t_{CTB}= 300mm. The applied load is q= 550kPa.

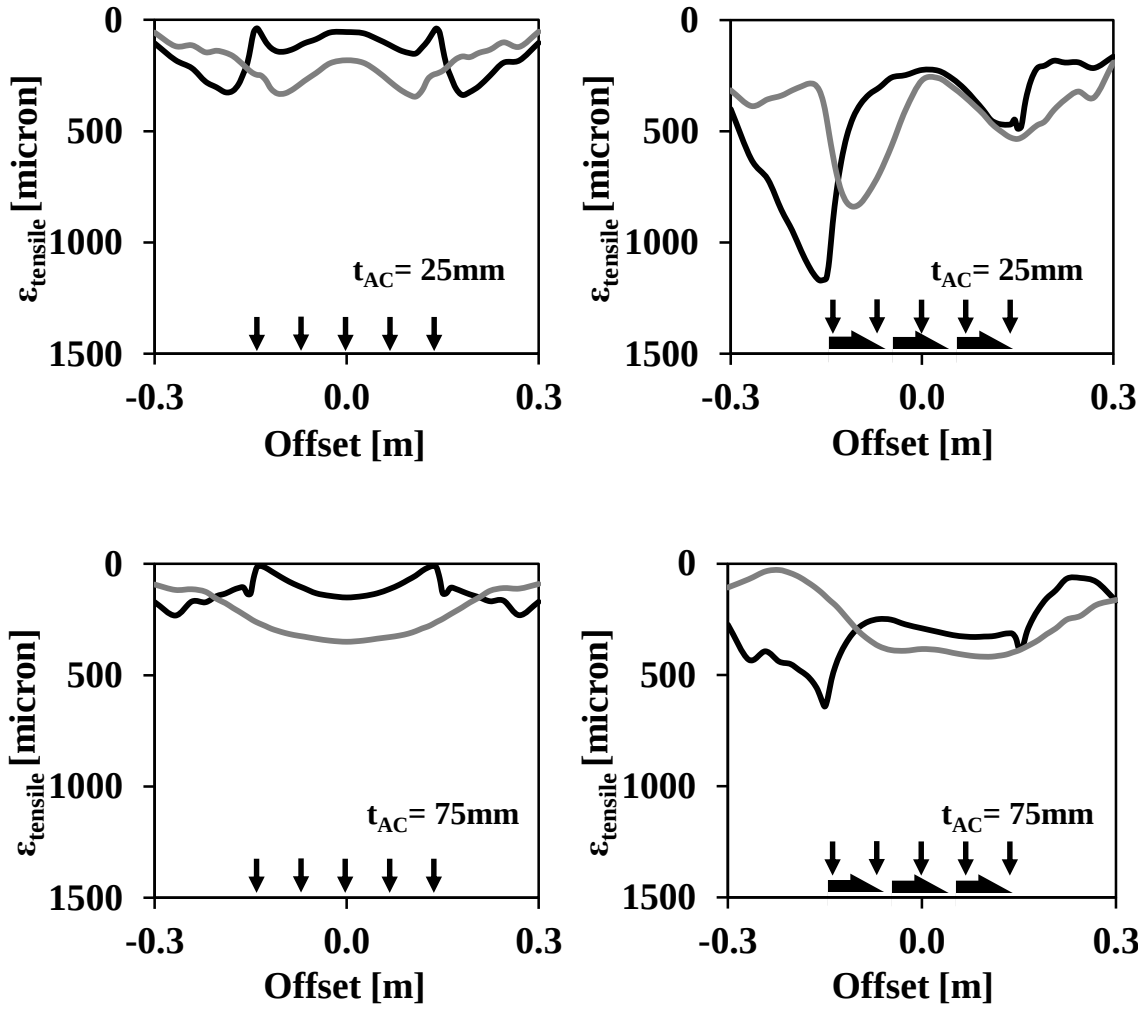

Figure 6.9. Tensile strain along the top (black line) and bottom (grey line) of the asphalt concrete layer for purely vertical loading and combined vertical and shear contact loading. The loading type is illustrated by the arrows.
Note: t_{GAB}= 150mm and t_{CTB}= 300mm. The vertical and shear contact loads are 550kPa.

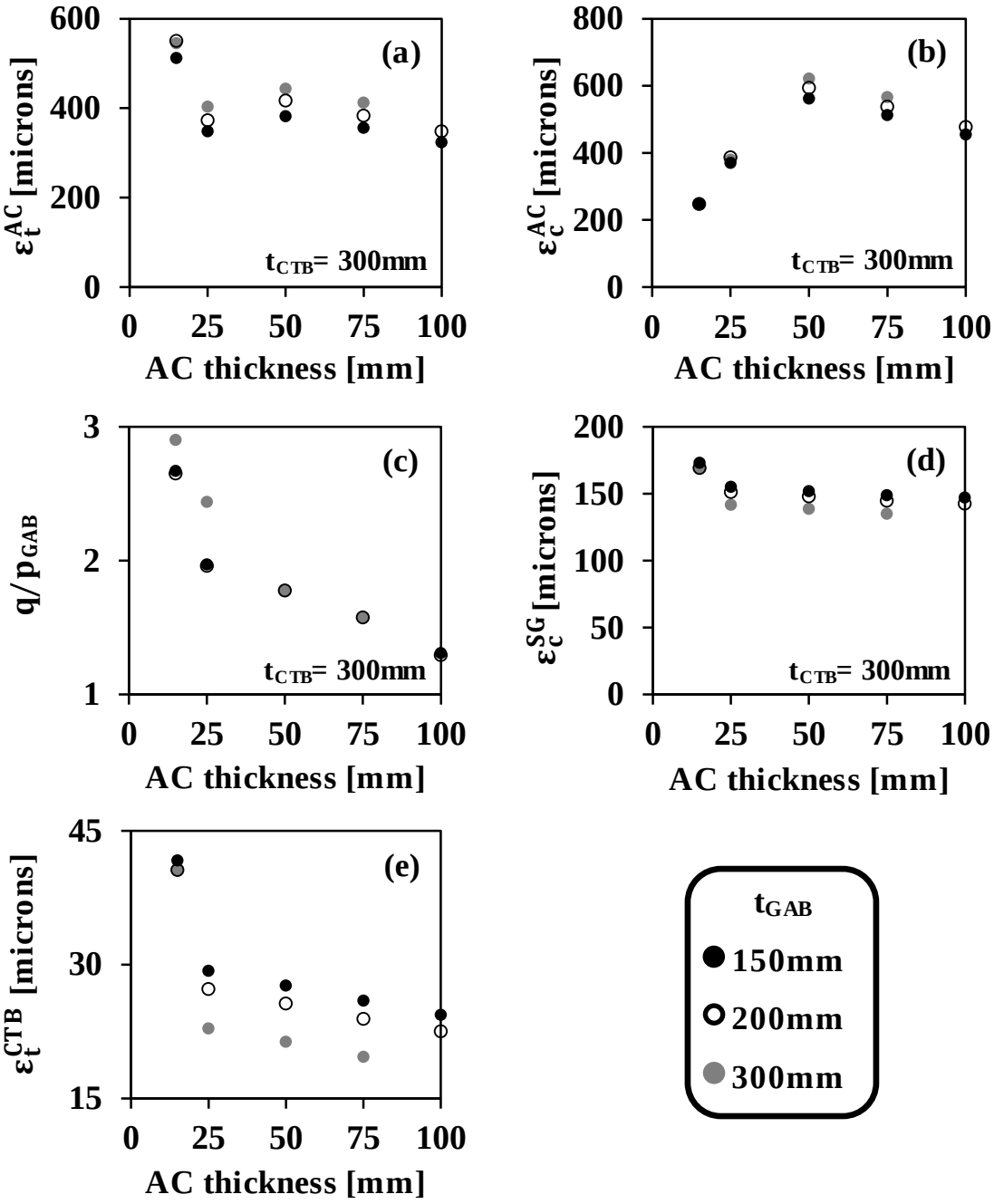

Figure 6.10. Maximum values of (a) AC tensile strain, (b) AC compressive strain and (c) stress ratio q/p in the GAB (d) subgrade compressive strain and (e) CTB tensile strain versus asphalt layer thickness for different inverted base pavements. CTB thickness is 300mm.

CHAPTER 7
INVERTED BASE PAVEMENTS: EQUIVALENT DESIGN ALTERNATIVES TO CONVENTIONAL FLEXIBLE PAVEMENTS

7.1 Introduction

Inverted base pavements are flexible pavements where the graded aggregate base layer GAB is placed above a cement-treated base CTB and immediately below a thin asphalt concrete surface layer AC (Cortes 2010; Tutumluer 2013). Such a structural design makes the unbound aggregate base an integral part of the pavement structure. Inverted base pavements use less asphalt and cement than alternative conventional asphalt pavements or rigid pavements. The combination of low-cost materials and evidence of excellent performance makes inverted base pavements a promising cost-efficient alternative to accommodate high traffic loads.

Several pavement design methodologies have been developed (AASHTO 1993; NCHRP 2004). The most recent mechanistic pavement design methodology can analyze any pavement structure to determine its response to traffic loads. The advantage of mechanistic procedures is that they are not limited by empirical data and can be applied to pavement structures with limited field data such as inverted base pavements.

The model developed in the finite element code ABAQUS presented in previous chapters is used to assess the performance of inverted pavements relative to conventional asphalt pavements (ABAQUS 2010). The numerical model accounts for the nonlinear and anisotropic behavior of the GAB through a user-defined subroutine. The response of the interface between layers in conventional pavements is considered to assess its effect

on the pavement response. Finally, conventional and inverted pavement structures are compared in terms of critical response parameters.

7.2 Pavement Design Guidelines

7.2.1 The AASHTO Pavement Design Guidelines

The AASHTO pavement design guidelines are based on the concept of serviceability developed during the original ASSHO Road Test (AASHO 1962). Initially, serviceability was a qualitative measure, i.e. the ability of the pavement structure to provide a smooth and safe ride. Today's present serviceability index PSI was developed to quantify the ride quality a pavement provides. PSI has been correlated to several distress modes such as rutting, fatigue cracking and ride smoothness. Serviceability has also been correlated to structural characteristics of the pavement structure such as layer thickness or the quality of the subgrade through the Structural Number (SN) and the Soil Support Value (SSV) concepts.

7.2.2 Mechanistic-Empirical Pavement Design Guidelines

The Mechanistic-Empirical Pavement Design Guidelines MEPDG relate the pavement mechanical response (stress, strain) to known types of pavement distress through the use of damage functions (NCHRP 2004). The estimated life is a function of the critical responses of the structure being analyzed, while the damage functions depend on material properties. The material response is assessed through laboratory tests, thus any pavement structure can be analyzed using the Mechanistic-Empirical Pavement Design Guidelines. This approach requires extensive input on material parameters and

traffic characteristics. Inconsistency between MEPDG results and empirically-validated solutions exacerbated by lack of adequate training and experience with the MEPDG have led to continued delays in its implementation into state guidelines (Li et al. 2012).

7.2.3 GDoT Design Catalogue

The Georgia Department of Transportation uses a modified version of the original AASHTO pavement design guidelines for the design of new pavement structures (GDOT 2005). In addition, GDoT has developed a catalogue of "Standard Pavement Sections for Use in Minor Projects". Inverted base pavements structures analyzed in this study are compared to conventional sections chosen from this catalogue.

7.3 Numerical Study

The analysis is conducted in the finite-element code ABAQUS. A three dimensional model is developed for the purpose of this study. The typical inverted base pavement is shown in **figure 7.1a**. Pavements of different thicknesses are analyzed to explore the best alternative designs. Conventional flexible pavements consist of three layers of asphalt concrete at the top, followed by a GAB subbase that rests on the natural subgrade (**figure 7.1b**). All conventional pavements analyzed in this study are shown in **figure 7.2**.

The finite element mesh used in these simulations is shown in **figure 7.1c**. A static circular uniform load of q=550kPa and radius r=150mm is applied on the surface of the pavement structure. This load is a convenient approximation for this comparative study (Liu and Shalaby 2013).

7.3.1 Material Parameters

Material parameters used in the numerical simulations are discussed in Chapter 6 and are summarized in **Table 7.1** for all pavements.

7.3.2 Interfacial Bonding Between Cohesive Layers

The bonding between successive asphalt concrete layers can vary dramatically depending on the stiffness and strength characteristics of the applied tack coat (Kruntcheva et al. 2005; West et al. 2005). Two conditions, full bonding and no bonding are modeled herein (**figure 7.3**). In the first case, the combined layer behaves as a monolithic beam; in the second case, it behaves as a laminated structure with interface behavior as described in **figure 7.3** i.e. an elastic stiffness with a maximum cohesive strength followed by a purely frictional residual strength (Romanoschi and Metcalf 2001). Selected model parameters are based on data from Romanoschi and Metcalf (2001). Unless noted, all simulations assume full bonding between the asphalt concrete layers in conventional pavements.

7.4 Results

Two conventional pavements and two inverted base pavements are compared first to highlight discrepancies between the two designs; the four pavement structures are shown in **figure 7.4**.

7.4.1 Stress Distributions

The distribution of vertical and horizontal stresses with depth below the centerline of the load is shown in **figure 7.5**. In conventional pavements, the vertical stress decreases

with depth mostly in the asphalt concrete layer. The asphalt concrete layers deform uniformly and develop compressive horizontal stress at the top and tensile stress at the bottom, typical of bending deformation. The vertical stress in the GAB and subgrade is quite low as the load has been redistributed within the AC layer. The horizontal stress is smaller than the vertical stress. Thicker AC layers result in lower stress both in the asphalt concrete as well as the GAB and subgrade (**figure 7.5a** and **b**). In other words, the larger total thickness of the asphalt concrete layers increases the effective beam "height" and reduces bending stresses while it provides better protection for the underlying layers.

The asphalt concrete layer in the high-structural capacity inverted base pavement deforms as a beam, similar to conventional pavements (**Figure 7.5d**). Contrary to conventional pavements, the GAB also contributes to load redistribution as shown by the gradient in vertical stress. In the low-volume inverted base pavement, the thin asphalt concrete surface layer tends to deform as a membrane structure rather than as a beam, and the tensile stress below the centerline is greatly reduced (**figure 7.5c**). Very little stress redistribution takes place in the asphalt concrete and so higher stresses develop in both the granular base and cement-treated base. The cement-treated base deforms in bending with tension at the bottom and compression at the top of the layer in both inverted base pavements. The magnitude of stresses that develop in the CTB is smaller than in the asphalt concrete primarily because the vertical stress has been redistributed in upper layers.

7.4.2 GAB Stiffness

Contours of vertical Young's modulus E_v within the GAB layer under the load are shown in **figure 7.6**. The maximum stiffness attained in inverted base pavements is considerably higher than that of conventional pavements despite identical material parameters (**figure 7.6**). The cement-treated base creates increased confinement for the GAB, as shown by the increased GAB stiffness close to the CTB interface. The proximity of the GAB to the external load exposes the GAB to higher levels of stress in inverted base pavements. While higher stress leads to higher GAB stiffness, shear softening may prevail in some areas when the AC thickness is very small (**figure 7.6c**).

As noted above the GAB stiffness in conventional pavements is considerably lower than in inverted base pavements. The stiffness contours for the thick-AC conventional pavement are quasi-horizontal which implies that the effect of the external load on the GAB is small (**figure 7.6b**). The GAB stiffness is higher away from the load in the low-volume conventional pavement, which implies considerable shear softening (**figure 7.6a**).

7.4.3 Asphalt Concrete

Figure 7.7 shows the tensile strain beneath the load imprint at the top and bottom of the asphalt concrete. Asphalt concrete layers in conventional pavements deform like a beam and develop large tensile strain at the bottom of the layer and some tensile strain at the edges of the load. (**figure 7.7a &7.7b**). The response of the inverted base pavement with the thick AC layer is similar to that of conventional pavements (**figure 7.7d**). In the thin-AC inverted base pavement, considerable tensile strain also develops at the edges of the load at the top of the layer (**figure 7.7c**). This response is indicative of the membrane-

like deformation. In general, the tensile strain that develops in thin AC layers is higher than in other pavements.

7.4.4 Critical Responses

The key structural responses related to major pavement distress types (fatigue cracking, rutting) are the tensile stress in the asphalt concrete and the cement-treated base and the compressive strain in all pavement layers and the subgrade. The critical responses for all conventional pavements simulated in this study are summarized in **table 7.2** (refer to **figure 7.2** for the associated structural designs). Results for the inverted base pavements are included in **table 7.3**. The AC tensile strain in conventional pavements is a declining function of the total thickness of asphalt concrete. AC layer deforms as a beam, and thicker beams are expected to develop lower tensile strains for the same external load. By contrast, the tensile strain in inverted base pavements is initially low for small values of AC thickness, gradually increases for intermediate thickness and falls again for large AC thicknesses. In general, inverted base pavements exhibit higher tensile strain than conventional pavements.

The subgrade compressive strain is considerably smaller for all the modeled inverted base pavements than in conventional pavements. Inverted base pavements redistribute traffic load more effectively due to the increased stiffness of the GAB and CTB layer (**figure 7.6**). Note that the gradual deterioration of the CTB in inverted base pavements is minimized by the stress relief provided by the GAB.

7.4.5 Effect of Interface Behavior

All conventional pavements are simulated using the not-bounded interface model described in **figure 7.3** to assess the effect of interface bonding. The stress distribution below the centerline of the load for the two cases of interface behavior is shown in **figure 7.8**. **Table 7.4** summarizes the critical responses of the conventional pavements when the no-bonding interface model is used. The pavements simulated using no-bonding (**figure 7.8a &7.8b**) behave like laminated beams with limited horizontal contact stiffness. This response decreases the overall stiffness of the beam structure and increases the maximum tensile stress at the bottom AC layer. Compressive stress at the top AC layer also decreases by a small amount. In general, most conventional pavements perform similar to or worse than inverted base pavements if the interface is accounted for.

7.4.6 Equivalent Designs

Numerical simulation results obtained in this study are used to compile a "pictorial manual" of equivalent inverted base pavement designs, whereby every conventional pavement analyzed is matched with an inverted base pavement of comparable performance in terms of critical responses. This pictorial manual is included at the end of the chapter.

7.5 Implication for Design Guidelines

7.5.1 Structural Number-Based Methods

According to the AASHTO pavement design guidelines, the structural capacity of a pavement is the sum of the structural numbers of all layers (AASHTO 1993). This

methodology does not consider the interaction between layers and cannot capture the capacity of an inverted structure. Layer coefficients are fixed irrespective of position in the pavement structure, with the exception of asphalt concrete. Specifically for the case of the GAB, the structural layer coefficient has been correlated very well to the resilient modulus of the material. However, the modulus of the GAB can vary considerably among different pavement structures as seen from the contours in **figure 7.6**. This is not taken into account in the SN-based design guidelines.

7.5.2 Mechanistic Methods

Pavement simulation programs used for mechanistic design guidelines often assume linear elastic behavior of the GAB which is unrealistic and leads to tensile stresses within the GAB layer (Tutumluer and Barksdale 1995). The stress-dependent stiffness of the (Thompson et al. 1998; Tutumluer and Barksdale 1995; Uzan 1985) as well as the inherent and stress-induced anisotropy of the GAB need to be taken into consideration since they can have a large effect on stresses and deformations (Adu-Osei et al. 2001; Al-Qadi et al. 2010; Tutumluer and Thompson 1997). Only a few studies have considered the effect of anisotropy, but without accounting separately for inherent and stress-induced anisotropy (Al-Qadi et al. 2010; Wang and Al-Qadi 2012).

7.5.3 Thick AC Layers

Previous observations suggest that a thin asphalt layer follows a membrane-like deformations and does not experience an increase in tension (**table 7.3**); in fact intermediate-thickness layers perform worse than thin layers. Furthermore, damage functions used in the MEPDG suggest that lower asphalt thickness results in less distress

for the same tensile strain (NCHRP 2004). Finally, thin asphalt layers develop top-down cracking, which can be relieved by surface treatment, contrary to the typical bottom-down cracking prevailing in most flexible pavements. Observations imply a potential reduction in the initial construction and operation costs.

7.6 Conclusions

This study analyzed and compared the behavior of several conventional flexible pavements to inverted base pavements. The main conclusions that come from this study are:

- Inverted base pavements respond different from conventional flexible pavements. The load transmission mechanism relies on the top-quality GAB and CTB layers while the asphalt surface layer is typically thin and does not significantly contribute to the load redistribution.
- Inverted base pavements perform on par with most conventional pavements analyzed in this study.
- The mobilized stiffness of the GAB in inverted base pavements is higher than in conventional pavements, due to confinement provided by the CTB layer and the proximity of the GAB to the load.
- When the behavior of the interface between AC layers is represented with a realistic model rather than full bonding, the behavior of inverted base pavements in terms of critical responses is consistently better than that of conventional pavements. Subgrade strain is also considerably smaller in inverted base pavements.

- Pavement design guidelines, especially those based on structural number experience limitations in the analysis of inverted base pavements. For mechanistic methods, the GAB stress sensitivity and anisotropy need to be properly modeled for a realistic prediction.
- Inverted base pavements can be a viable and cost-efficient pavement alternative.

Table 7.1. Material parameters used in the finite-element model.

GAB			
Stiffness Parameters		c_1^z **(MPa)**	**130**
		c_1^x **(MPa)**	**90**
		c_1^y **(MPa)**	**90**
		c_2	**0.45**
		c_3	**0.15**
Poisson's ratio		ν_{xy}	**0.35**
		ν_{zy}	**0.35**
		ν_{zx}	**0.35**
Strength parameters		**c (kPa)**	**15**
		φ	**57°**
	AC	**CTB**	**SG**
Young's Modulus E	**2 GPa**	**10 GPa**	**50 MPa**
Poisson's Ratio	**0.35**	**0.2**	**0.2**

Table 7.2. Critical responses and structural number for the conventional pavements analyzed in this study (refer to Figure 7.2).

	D-12	C-12	B-14	C-10	B-12	B-10	B-8	A8
ε_t^{AC}	180	210	290	210	300	310	310	380
ε_c^{AC}	210	250	340	250	350	360	360	440
ε_c^{GAB}	410	500	850	480	800	780	770	1000
ε_c^{SG}	330	380	350	410	510	560	620	750
Structural Number	5.63	5.33	5.05	5.01	4.73	4.41	4.09	3.79

Note: strains are in micron. Structural number calculated through the GDOT pavement design guidelines.

Table 7.3. Layer thicknesses, critical responses and structural number for the inverted base pavements analyzed in this study.

t_{AC} [mm]	25	25	75	100
t_{GAB} [mm]	150	300	200	150
t_{CTB} [mm]	250	300	300	300
ε_t^{AC}	350	400	380	310
ε_c^{AC}	360	380	540	440
ε_c^{SG}	200	140	150	140
ε_t^{CTB}	41	23	24	15
Structural Number	3.54	4.9	5.16	5.28

Note: strains are in microns. Structural number calculated through the GDOT pavement design guidelines.

Table 7.4. Critical responses and structural number for the conventional pavements analyzed using the interface constitutive model shown in figure 3.

	D-12	C-12	B-14	C-10	B-12	B-10	B-8	A8
$\boldsymbol{\varepsilon_t^{AC}}$	250	290	380	300	390	400	410	460
$\boldsymbol{\varepsilon_c^{AC}}$	300	350	450	360	470	480	480	540
$\boldsymbol{\varepsilon_c^{GAB}}$	400	520	950	540	900	940	1000	1400
$\boldsymbol{\varepsilon_c^{SG}}$	550	650	600	710	910	1000	1100	1400
Structural Number	5.63	5.33	5.05	5.01	4.73	4.41	4.09	3.79

Note: strains are in microns. Structural number calculated through the GDOT pavement design guidelines.

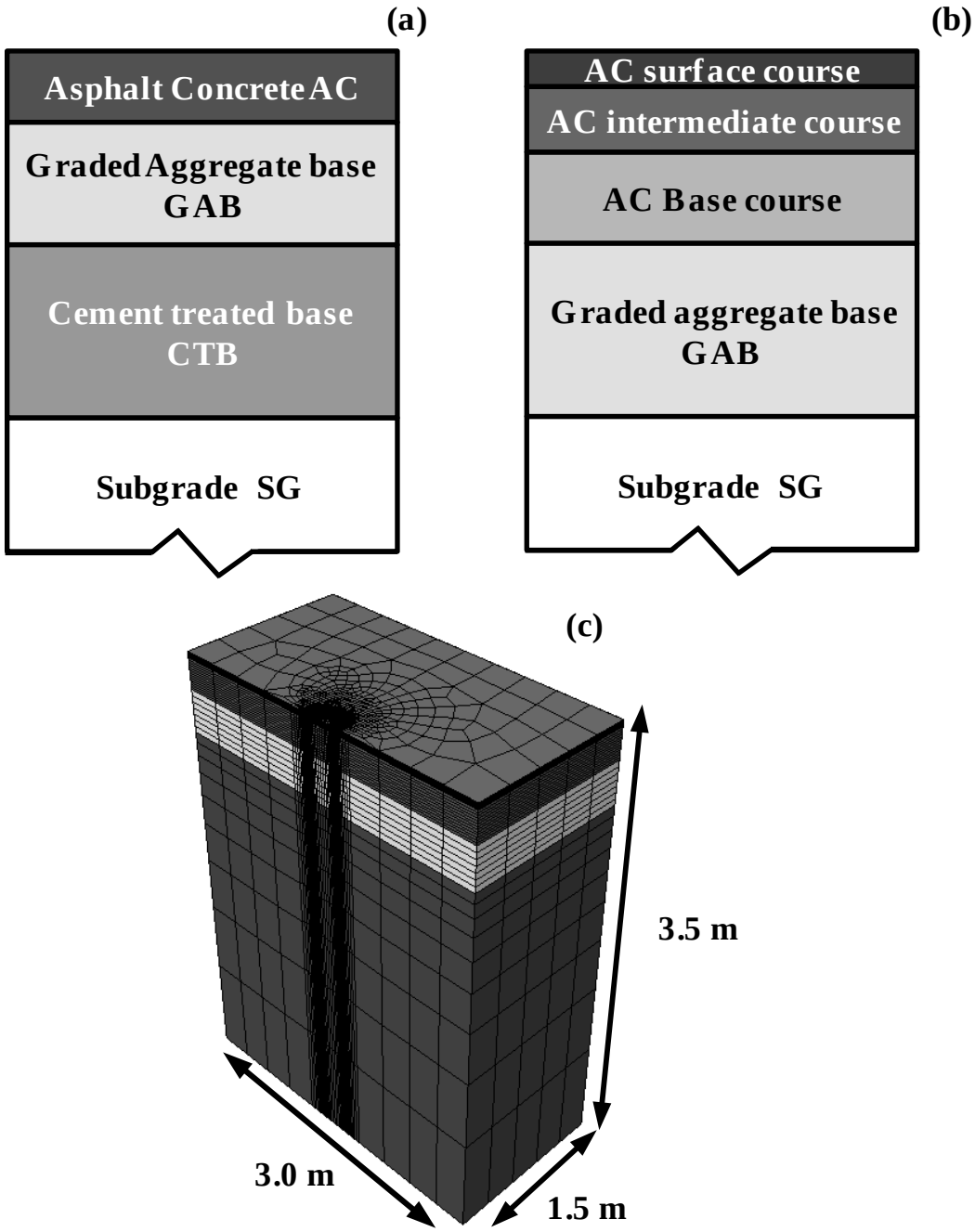

Figure 7.1. Illustration of (a) a typical inverted base pavement and (b) a conventional asphalt base pavement. (c) Finite-element model geometry and mesh used for numerical simulations.

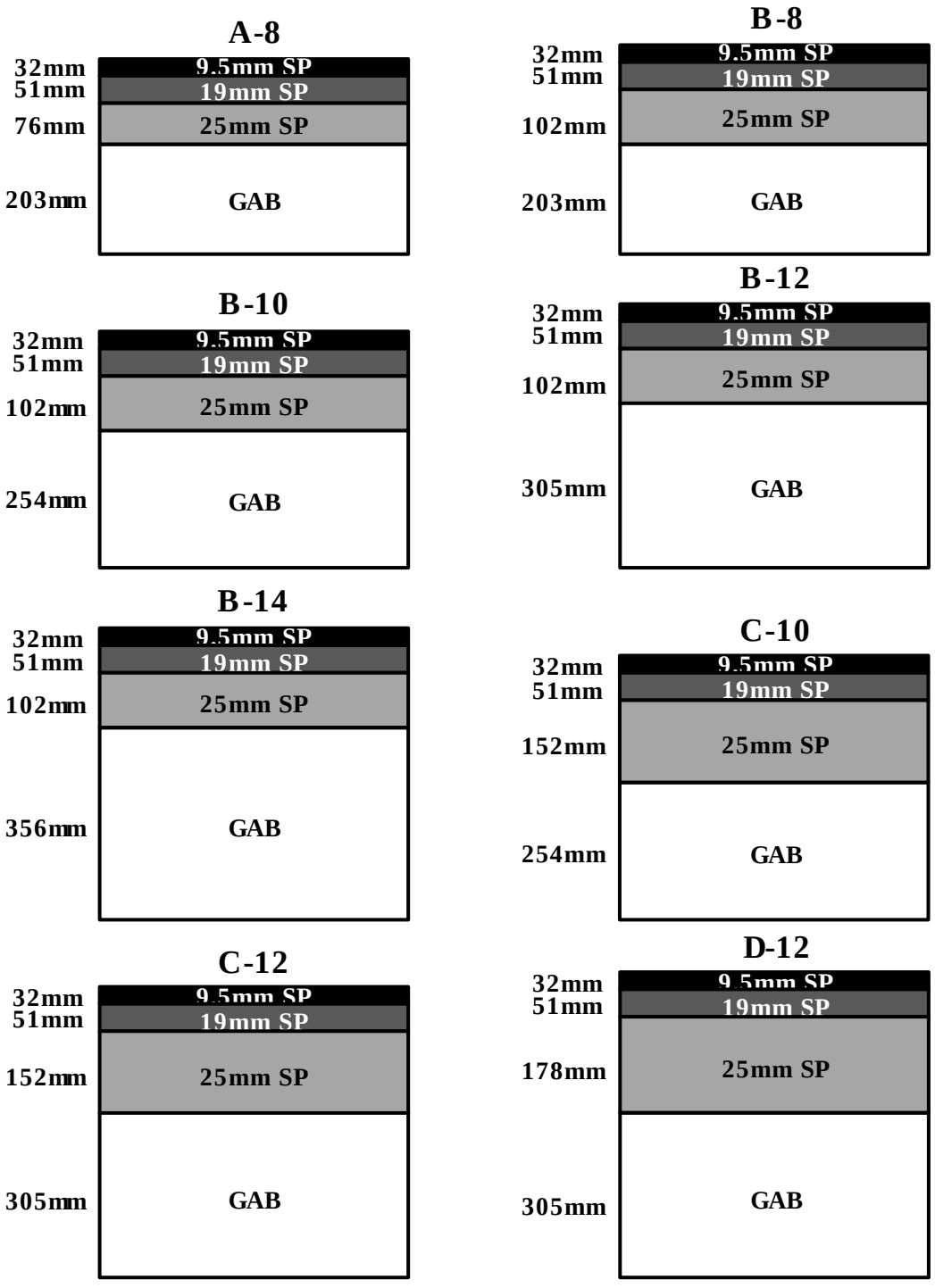

Figure 7.2. Conventional asphalt pavements from the GDoT catalogue selected for this study.

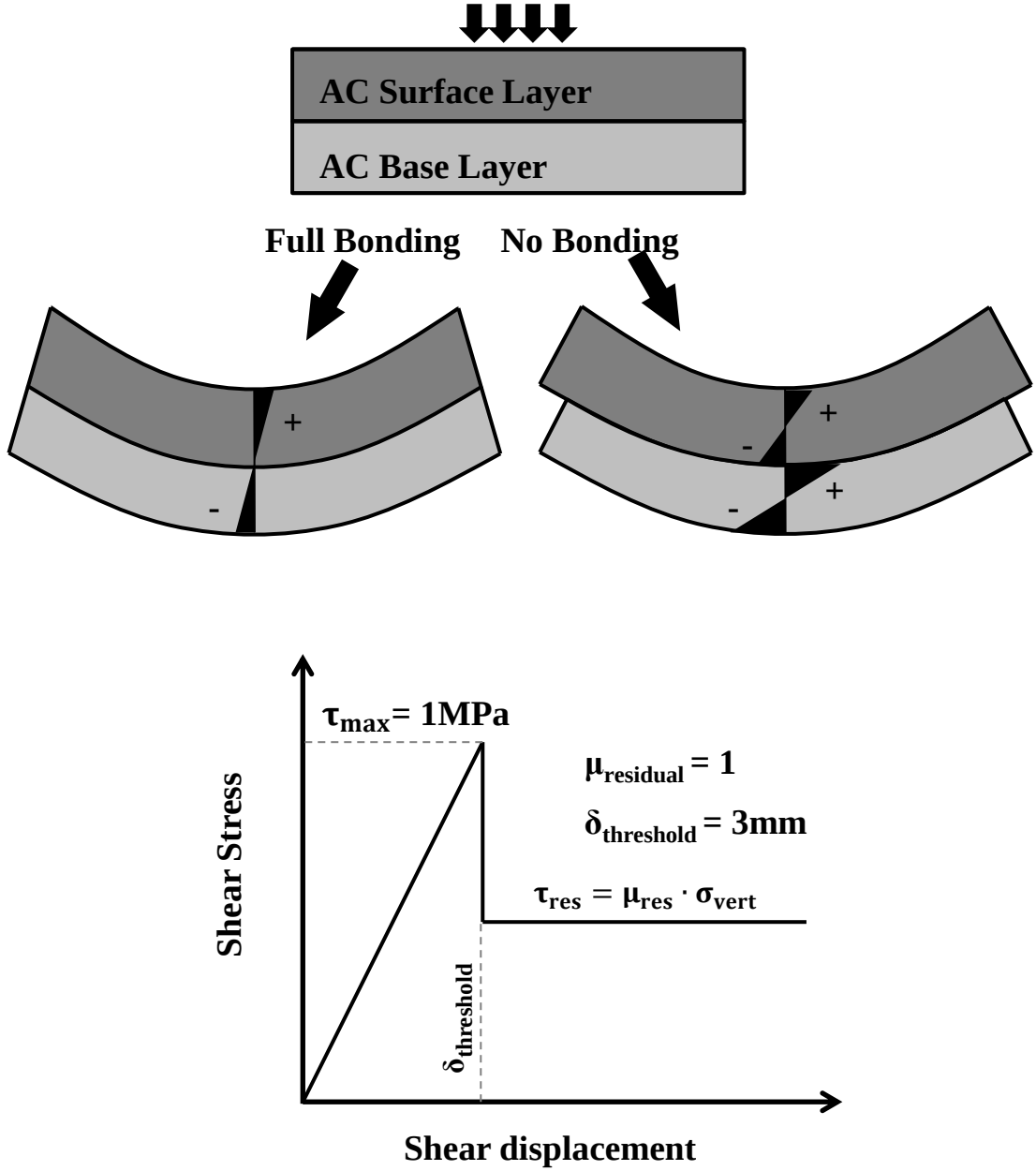

Figure 7.3. Interface bonding. (a) Difference in structural response when full bonding is assumed between layers and when relative interface displacement is allowed. (b) Stress displacement behavior of the interface model assumed in no-bonding simulations.

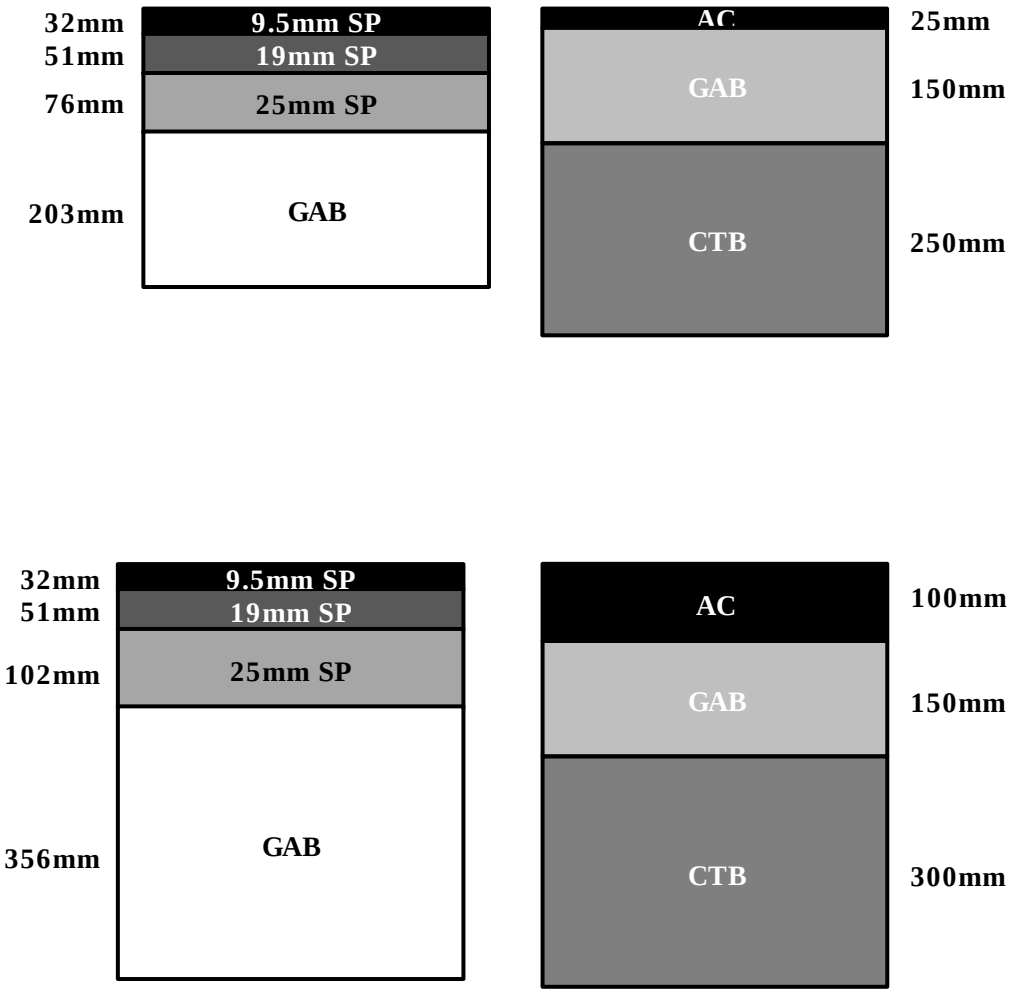

Figure 7.4. Conventional pavements and inverted base pavements. Selected cases for preliminary comparison.

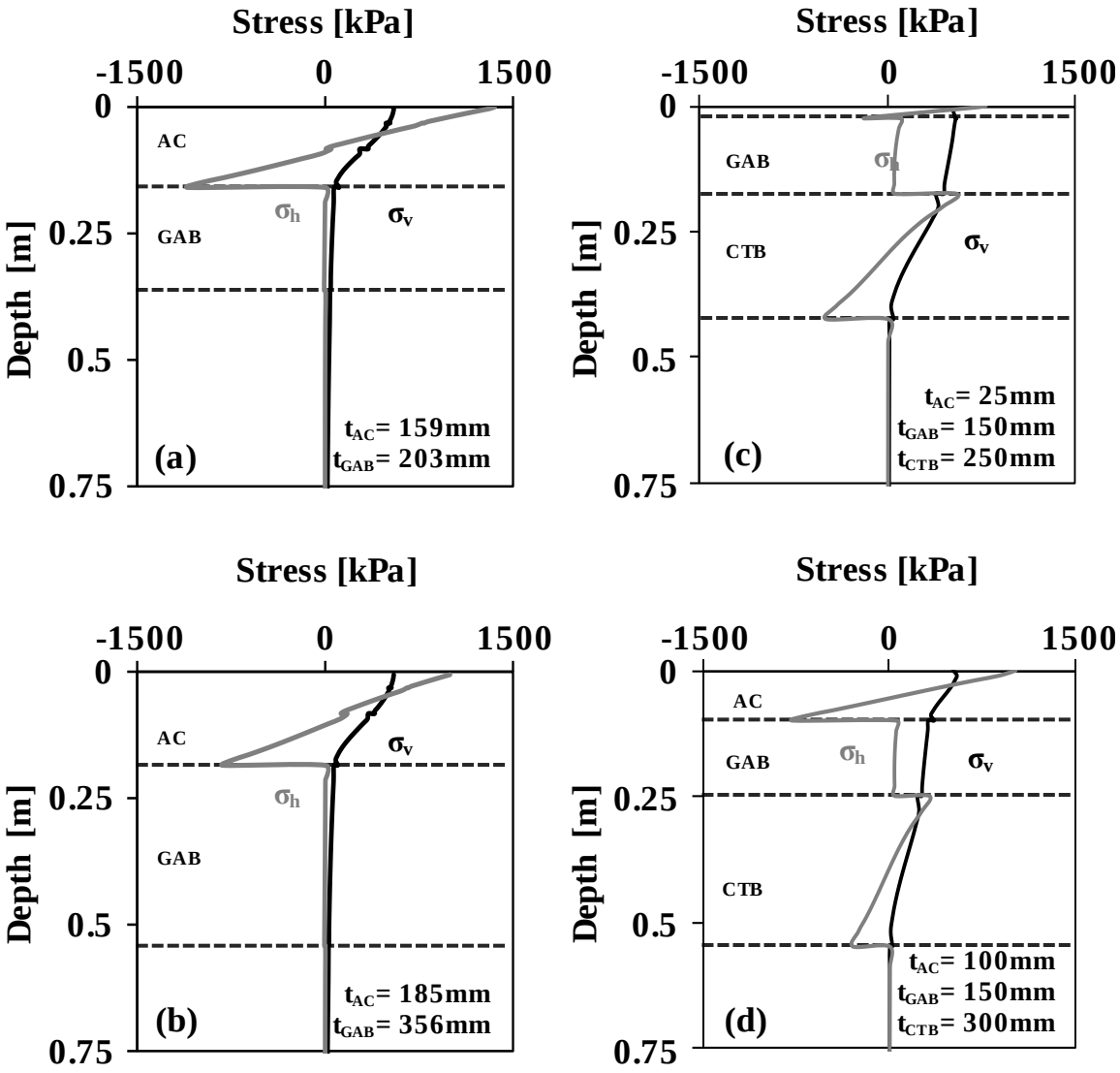

Figure 7.5. Vertical stress σ_v and horizontal stress σ_h distribution versus depth under the load centerline for the 4 pavements described in figure 7.4.

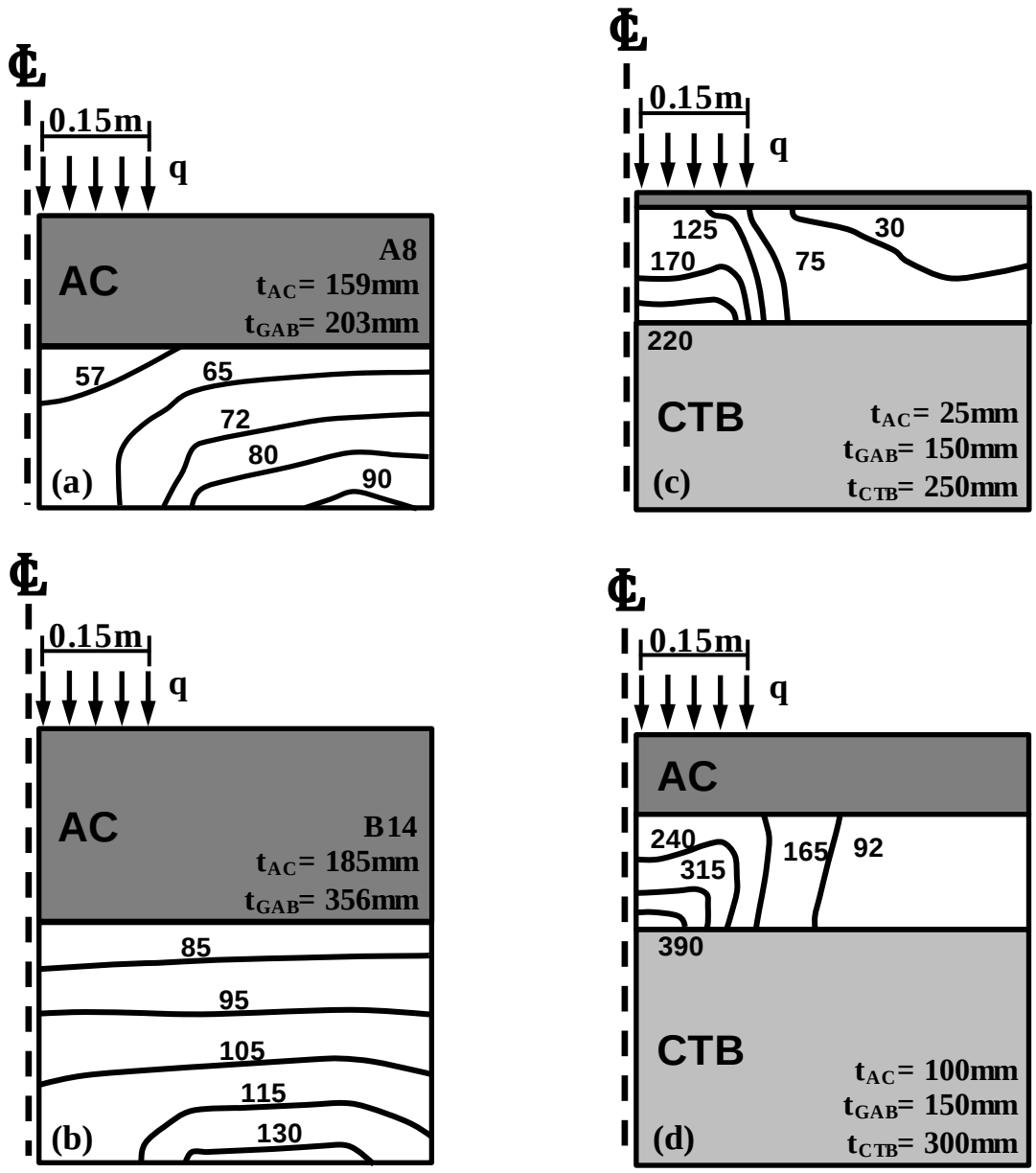

Figure 7.6. Contours of vertical Young's modulus E_v [MPa] for the GAB for the conventional and inverted base pavements described in figure 7.4. The applied load is q=550kPa.

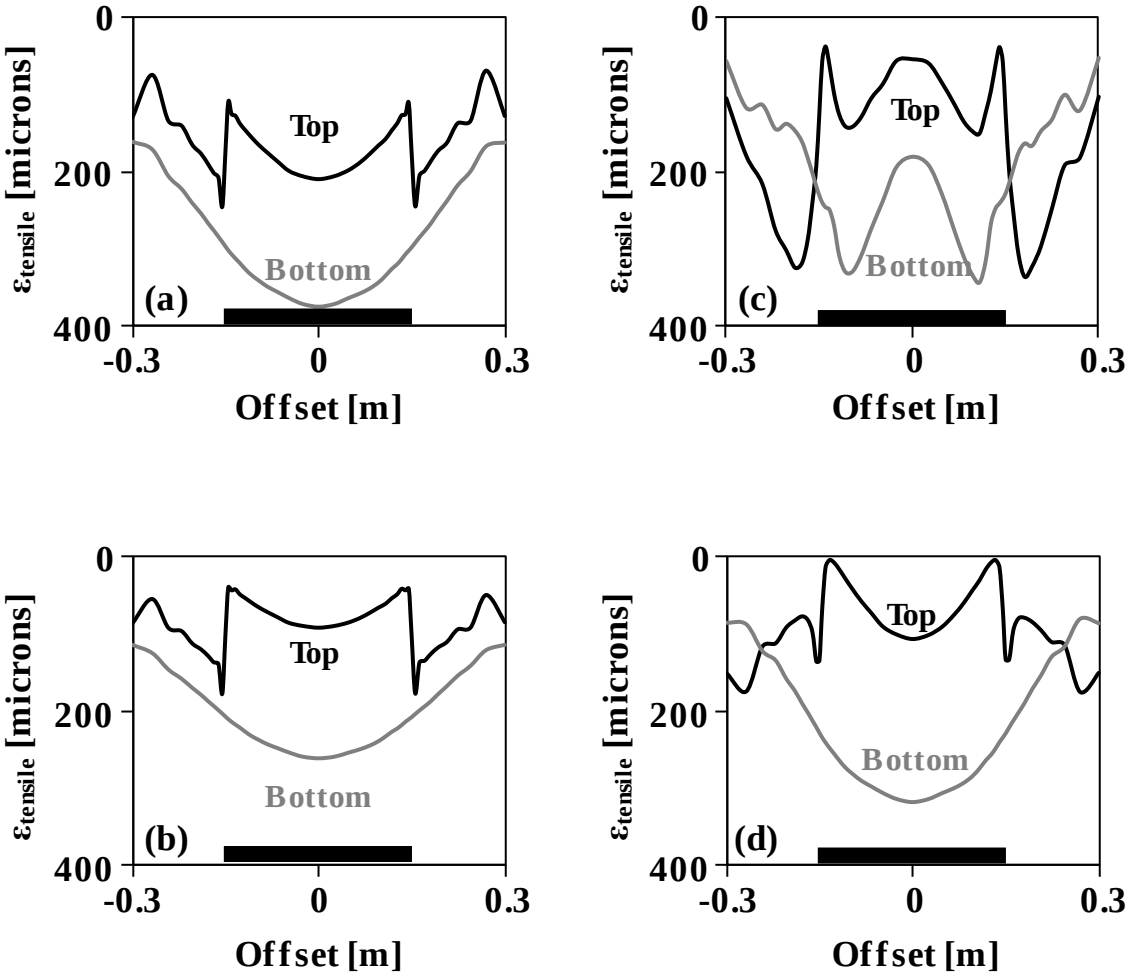

Figure 7.7. Tensile strain along the top and bottom of the asphalt concrete layer under the wheel load for the conventional and inverted base pavements described in figure 7.4. The applied load imprint is shown with the black line.

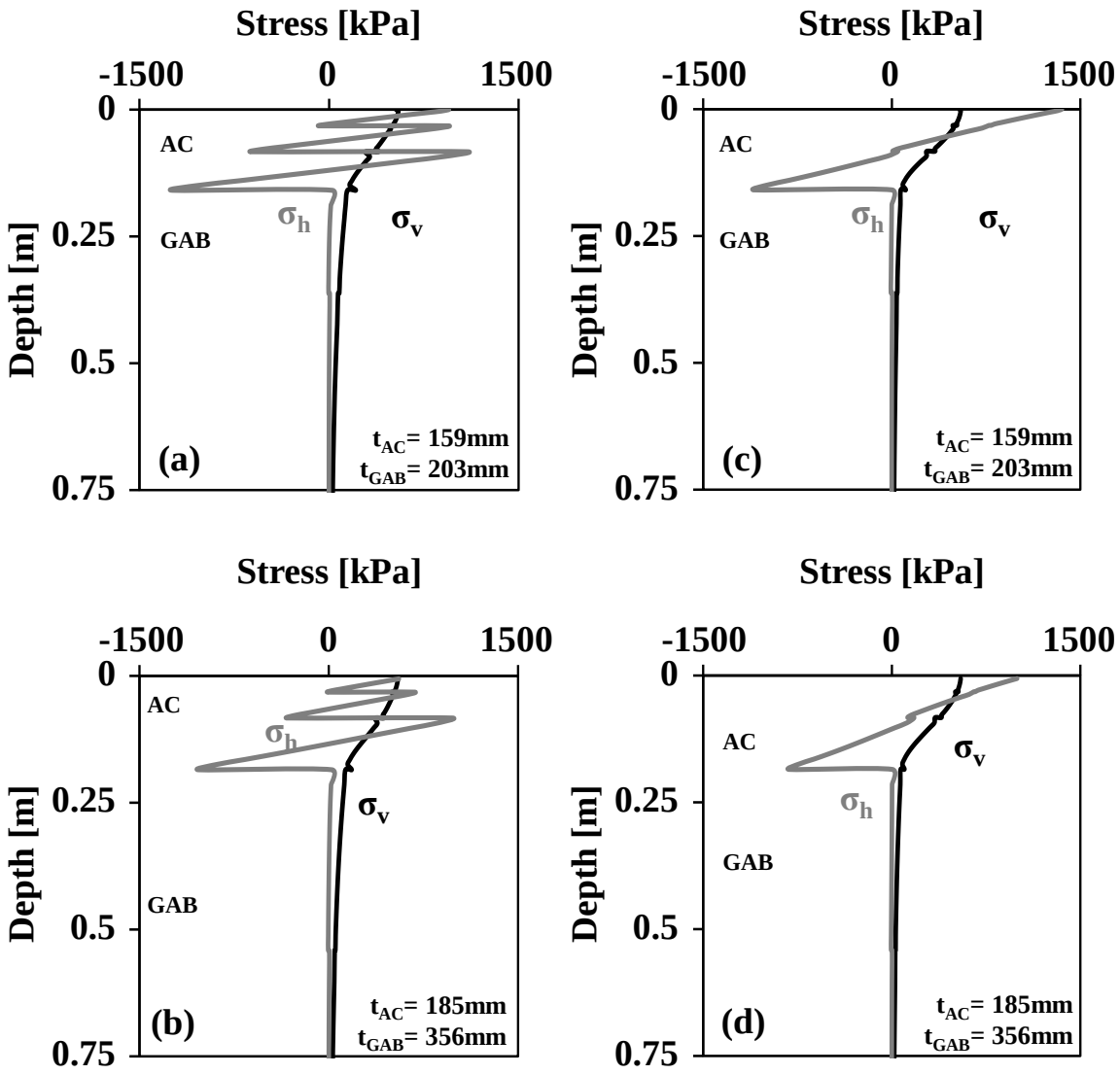

Figure 7.8. Layer bonding effect. Vertical stress σ_v and horizontal stress σ_h distribution versus depth for the two conventional pavements described in figure 7.4. (a and b) Interface model shown in figure 7.3 is used. (c and d) Perfect bonding is assumed between AC layers.

Pictorial Manual of Equivalent Designs

Conventional Pavement		Inverted Base Pavement
	A-8	
	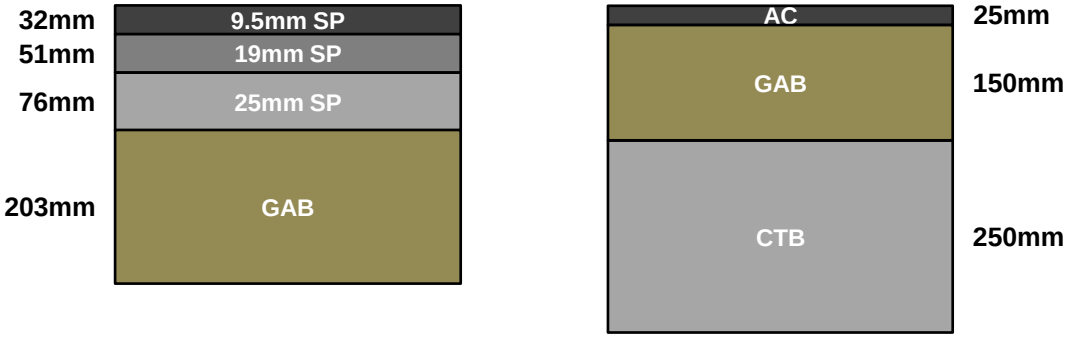	
ε_t^{AC}:	$4.6 \cdot 10^{-4}$	$3.5 \cdot 10^{-4}$
ε_v^{AC} :	$5.4 \cdot 10^{-4}$	$3.6 \cdot 10^{-4}$
ε_v^{SG} :	$14 \cdot 10^{-4}$	$2.0 \cdot 10^{-4}$
SN :	3.79	3.35

Conventional Pavement	Inverted Base Pavement

B-8

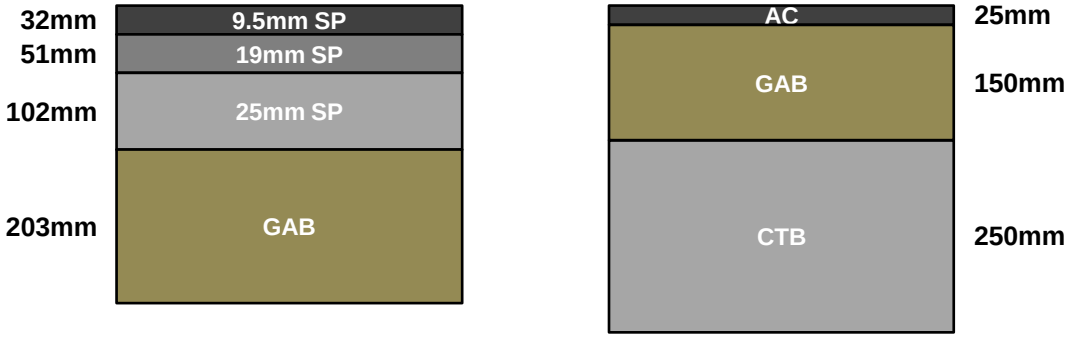

ε_t^{AC}:	$4.1 \cdot 10^{-4}$	$3.5 \cdot 10^{-4}$
ε_v^{AC} :	$4.8 \cdot 10^{-4}$	$3.6 \cdot 10^{-4}$
ε_v^{SG} :	$11 \cdot 10^{-4}$	$2.0 \cdot 10^{-4}$
SN :	4.09	3.35

Conventional Pavement		Inverted Base Pavement
	B-10	
	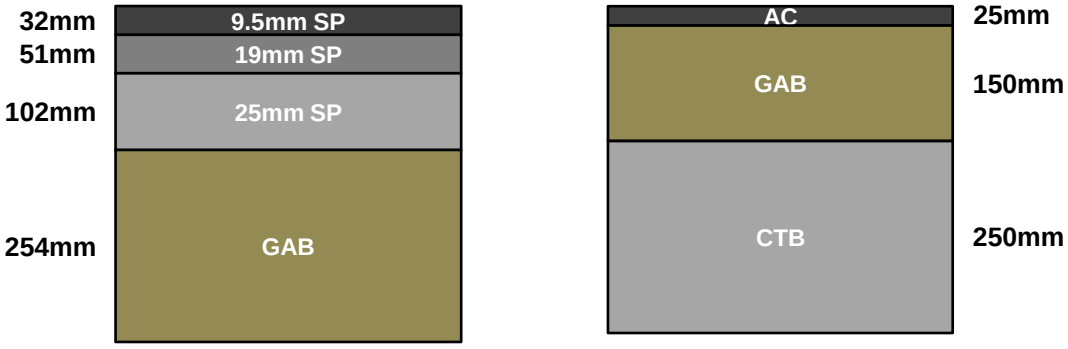	
ε_t^{AC}:	$4.0 \cdot 10^{-4}$	$3.5 \cdot 10^{-4}$
ε_v^{AC} :	$4.8 \cdot 10^{-4}$	$3.6 \cdot 10^{-4}$
ε_v^{SG} :	$10 \cdot 10^{-4}$	$2.0 \cdot 10^{-4}$
SN :	4.41	3.35

Conventional Pavement	Inverted Base Pavement

B-12

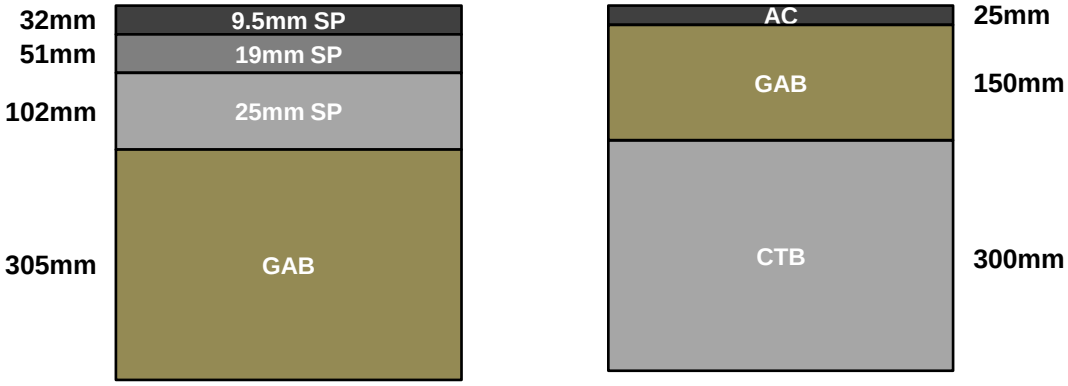

ε_t^{AC}:	$3.9 \cdot 10^{-4}$	$3.5 \cdot 10^{-4}$
ε_v^{AC} :	$4.7 \cdot 10^{-4}$	$3.7 \cdot 10^{-4}$
ε_v^{SG} :	$9.1 \cdot 10^{-4}$	$1.6 \cdot 10^{-4}$
SN :	4.73	3.74

Conventional Pavement	Inverted Base Pavement

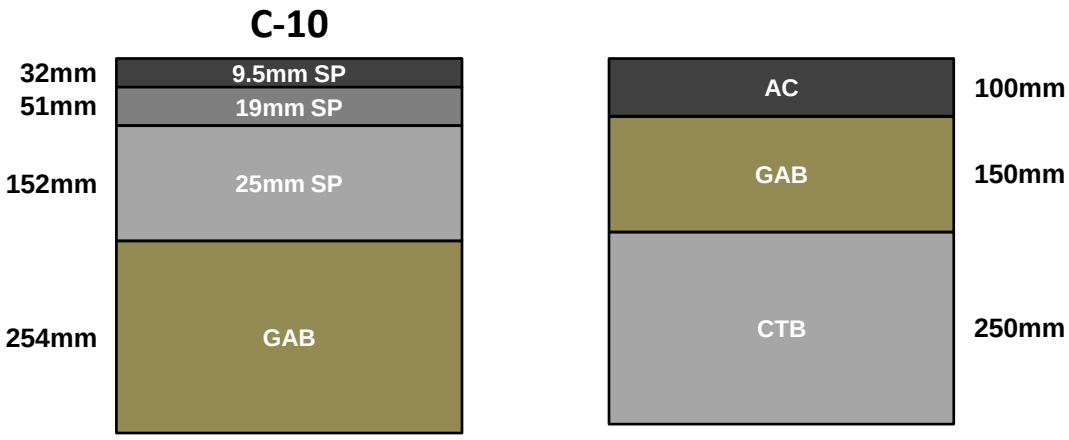

ε_t^{AC}:	$3.0 \cdot 10^{-4}$	$3.1 \cdot 10^{-4}$
ε_v^{AC} :	$3.6 \cdot 10^{-4}$	$4.4 \cdot 10^{-4}$
ε_v^{SG} :	$7.1 \cdot 10^{-4}$	$1.8 \cdot 10^{-4}$
SN :	5.01	4.65

	Conventional Pavement	Inverted Base Pavement
	B-14	
		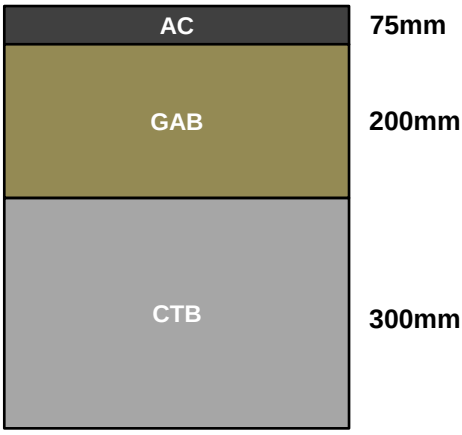
ε_t^{AC}:	$3.8 \cdot 10^{-4}$	$3.8 \cdot 10^{-4}$
ε_v^{AC} :	$4.5 \cdot 10^{-4}$	$5.4 \cdot 10^{-4}$
ε_v^{SG} :	$6.0 \cdot 10^{-4}$	$1.5 \cdot 10^{-4}$
SN :	5.05	5.04

Conventional Pavement		Inverted Base Pavement
	C-12	
32mm	9.5mm SP	AC 100mm
51mm	19mm SP	
152mm	25mm SP	GAB 150mm
305mm	GAB	CTB 300mm
ε_t^{AC}:	$2.9 \cdot 10^{-4}$	$3.2 \cdot 10^{-4}$
ε_v^{AC} :	$3.5 \cdot 10^{-4}$	$4.6 \cdot 10^{-4}$
ε_v^{SG} :	$6.5 \cdot 10^{-4}$	$1.5 \cdot 10^{-4}$
SN :	5.33	5.04

Conventional Pavement		Inverted Base Pavement
	D-12	
32mm	9.5mm SP	
51mm	19mm SP	AC 100mm
178mm	25mm SP	GAB 150mm
305mm	GAB	CTB 300mm
ε_t^{AC}:	$2.5 \cdot 10^{-4}$	$3.2 \cdot 10^{-4}$
ε_v^{AC} :	$3.0 \cdot 10^{-4}$	$4.6 \cdot 10^{-4}$
ε_v^{SG} :	$5.5 \cdot 10^{-4}$	$1.5 \cdot 10^{-4}$
SN :	5.63	5.04

CHAPTER 8
CONCLUSIONS AND RECOMMENDATIONS

8.1 Conclusions

The purpose of this thesis is to assess the potential for implementation of inverted base pavements in the US. The unbound aggregate base plays a critical part in the performance of inverted base pavements. To this end, part of this study was devoted to the study of the mechanical behavior of granular bases. The key insights arising from this work are presented below:

- Inverted base pavements are flexible pavements that can be constructed using conventional techniques and have demonstrated excellent performance to date, in both laboratory scale testing, field testing and under real traffic conditions.
- The unbound aggregate base is a critical part of the load-bearing mechanism in inverted base pavements.
- True triaxial tests reveal that the stiffness of the GAB is anisotropic and stress-dependent. The small-strain longitudinal stiffness in each principal direction is determined by the collinear normal stress.
- The small-strain stiffness results from contact-level at constant fabric conditions. On the other hand, the slope of the stress-strain curve captures changes in fabric and it is inherently different from the small-strain stiffness.

- The compaction of granular bases cannot be assessed on the basis of dry density or water content alone. Indeed, there is very small correlation between these parameters and the small-strain stiffness.
- The in-situ small-strain stiffness of unbound aggregate bases is anisotropic and stress-dependent. Field-compacted bases exhibit a higher degree of inherent anisotropy compared to laboratory-compacted specimens.
- Results from numerical simulations of inverted base pavements show that the response of the asphalt concrete layer changes from beam-like to membrane-like and the tensile stress at the bottom of the layer decreases as the thickness of the asphalt decreases.
- Inverted base pavements with thin asphalt layers were found to be particularly susceptible to shear loading at the pavement surface due to the high tensile strains in the asphalt layer.
- The unbound aggregate base in inverted base pavements develops much higher stiffness under load compared to conventional pavements, and has a greater contribution to load redistribution.
- Numerical simulations were used to identify equivalent inverted base pavement designs for typical conventional pavement structures. Design methods based on Structural Number fail to capture layer interaction in inverted base pavements and should not be used for their design.

8.2 Recommendations for Future Studies

The following recommendations address the implementation of inverted base pavements and the needs for characterization of granular bases:

- The construction of new inverted base pavement structures in strategic projects is encouraged. Extensive instrumentation is suggested so that the pavement's performance is monitored closely. New inverted base pavements of different structural capacities should be constructed to evaluate different designs, particularly those with thin asphalt layers.
- The transition from beam to membrane-like asphalt response requires further study. Possible factors that affect this boundary include temperature, asphalt stiffness and asphalt mix properties.
- The sensitivity of unbound aggregate bases to water should be explored further. Studies should focus on material degradation due to stress corrosion or hydro-mechanical effects at inter-particle contacts.
- The anisotropic nature of granular base stiffness must be taken into consideration in design guidelines.
- Direct stiffness tests should be conducted during the compaction of granular bases. Developments in continuous compaction control methodologies offer a viable alternative towards performance based compaction.

APPENDIX I:
CODA ANALYSIS – THE STRETCHING COEFFICIENT METHOD

In several chapters of this thesis, wave propagation is used to monitor the properties of geomaterials, most importantly stiffness. Wave propagation measurements can be very useful as they are less affected by boundary effects. For example, in the case of specimen stiffness, it is shown in chapter 4 that wave propagation is much less affected by the wall friction and even in that case, it is underestimated, which is conservative in the conventional sense.

The standard technique that is used for stiffness measurements using wave propagation is that of the first arrival. In that case, wave velocity is calculated by dividing the travel length over the travel time. For p-waves, which are the fastest traveling signal in an elastic medium, the travel time is measured as the time between the excitation of the source transducer and the time the first perturbation in the response of the receiver, called the "first arrival". There has been great controversy in the interpretation of small-strain measurements, particularly in the choice of first arrival (Clayton 2011; Lee and Santamarina 2005; Youn et al. 2008). The inherent uncertainty associated with the first arrival does not allow the monitoring of slow processes where the rate of parameter change among subsequent signals is small.

Contrary to the first arrival, the signal tail or coda captures the scattered and reflected waves. These waves have travelled greater distance within the medium and have therefore been more affected by the change in the medium property. Therefore, the signal tails can be used to estimate the change between subsequent signals (Snieder 2006). There are several techniques in the literature that have been used to monitor signal codas

(Dai et al. 2011; Grêt et al. 2005). In this thesis, the stretching coefficient method has been used (Snieder et al. 2002). This method assumes that two consecutive signals will overlap by stretching, that is multiplying all the time values of the "faster" signal by λ. It involves an iterative procedure to estimate the "stretching coefficient" λ that yields the best match between the two signals. Usually, the cross-correlation between the signals is used as a measure of match. Once the relative difference between all signals is calculated, the absolute value for one signal needs to be estimated. This method dramatically reduces the uncertainty in the values, as only one value needs to be estimated.

An algorithm for time-stretch coda was implemented in MATLAB and used throughout this study to monitor the stress sensitivity of the stiffness of granular bases. The algorithm involved normalizing all the received signals and time-stretching consecutive signals to infer the stretching coefficient. Finally, one signal was used as the base, and the wave velocity was calculated for that signal through the first arrival technique. The algorithm used in presented below for one case of signals:

```
%% Read .csv files
name_scopes= ; % search give names of .csv files for scopes
for n_calcul=1:14
% search for the file with name "name_scopes(n_calcul)"
scope=csvread(char(name_scopes(n_calcul)),2,0);
% create temporary time and voltage values
t(:,1)=scope(:,1);
v(:,1)=scope(:,3);
```

```
% Pass temporary files to the temporary 3D matrix
temp_all_scopes(:,:,n_calcul)=[t v];
% plot all scopes to see which part we will keep
figure(1)
hold on
plot(v(:,1))
% set the minimum value to clear negative time values
nmin(n_calcul) = find(t<=0,1,'last');
clear scope t v
end
% ask which point to take ass signal cut-off
nmax=input('Give me the final element cut-off point: ');
nminn=min(nmin)+1;
all_scopes(:,:,:)=temp_all_scopes(nminn:nmax,:,:);
%% Form cascades
 n_end=size(all_scopes,3);  %% number of scopes
% For each signal, Normalize by the maximum value and subtract the DC offset, then shift down by 1
hold on
 for i=1:n_end;
plot(all_scopes(:,2,i))
end
hold off
```

```
DC_range=input('give  me range  of your DC offset: ');
for n=1:n_end
figure(1)
hold on
plot(all_scopes(:,2,n))
t_old_scope(:,1)=all_scopes(:,1,n);  % Temporary  files  with time
v_old_scope(:,1)=all_scopes(:,2,n);  % Temporary  files  with voltage
max_value(n)=1.2*max(max(all_scopes(:,2,n)),-min(all_scopes(:,2,n)));
DC_offset=mean(all_scopes(1:DC_range,2,n));
norm_scope(:,1,n)=t_old_scope(:,1);
norm_scope(:,2,n)=(v_old_scope(:,1)-DC_offset)/max_value(n);
shift_scope(:,1,n)=t_old_scope(:,1);
shift_scope(:,2,n)=(v_old_scope(:,1)-DC_offset)/max_value(n)-n+1;
figure(2)
hold on
plot(norm_scope(:,1,n),norm_scope(:,2,n))
figure(3)
hold on
plot(shift_scope(:,1,n),shift_scope(:,2,n))
end
%% Plot all signals  to determine  which  will  be the Base signal  that has l=0
 n_end=size(norm_scope,3);  % number  of signals
 figure(1)
```

```
hold on
hold all
for i=1:n_end
plot(shift_scope(:,2,i))
end
h_legend=legend(name_scopes);
set(h_legend,'FontSize',8);
xlabel('element number')
ylabel('voltage [V]')
figure(2)
hold on
hold all
for i=1:n_end
plot(norm_scope(:,2,i))
end
h_legend=legend(name_scopes);
set(h_legend,'FontSize',8);
xlabel('element number')
ylabel('voltage [V]')
n_stable=input('Provide the number of the Base scope: ');
 % ask which point to take as imitial signal cut-off
 nmin=input('Give me the initial element cut-off point for the CC: ');
 norm_scope1(:,:,:)= norm_scope(nmin:size(norm_scope,1),:,:);
```

```
%% Begin identifying the stretching coefficient l for every signal
tic
for n=n_stable-1:-1:1
% store values of the signal that will be stretched and the Base Signal in
% dummy variables
t_old_scope(:,1)=norm_scope1(:,1,n);
v_old_scope(:,1)=norm_scope1(:,2,n);
t_stable_scope(:,1)=norm_scope1(:,1,n+1);
v_stable_scope(:,1)=norm_scope1(:,2,n+1);
% initialize a counter to track the iteration number for lamda
count=1;
% Initialize FOR loop to get the CC=f(lamda) curve
for lamda=1:-0.001:0.7
t_new(:,1)=t_old_scope(:,1).*lamda; % Calculate stretched time vector
scope_new(:,:)=[t_new v_old_scope]; % new scope with the new time and the old V
ts1(:,1)=timeseries(v_old_scope(:,1),t_new(:,1)); % time-series of stretched signal
% Construct a time-series element from the base signal
tsBase(:,1)=timeseries(v_stable_scope(:,1),t_stable_scope(:,1));
%% Synchronize the time values of the two signals to permit cross-correlation
[temp1, temp2]=synchronize(ts1,tsBase,'Union');
%% Do the cross-correlation to determine the similarity between
% signals
v1(:,1)=temp1.data; % new V of scope
```

```
v2(:,1)=temp2.data;  % new V of stable  scope
v1v2(:,1)=v1(:,1).*v2(:,1);  % multiplication  of V
cc=sum(v1v2);  % sum  of V1*V2  - cross correlation
%% Save for count  (one scope)
lamda_s(count,1)=lamda;
temp1_s(:,count)=temp1(:,:);
temp2_s(:,count)=temp2(:,:);
cc_s(count,1)=cc;
clear t_new scope_new ts1 tsBase temp1 temp2 v1 v2 v1v2 cc
count=count+1;
end
lamda_all(:,n)=lamda_s(:,1);
cc_all(:,n)=cc_s(:,1);
% save values  for all scopes
save results_scopes2  lamda_all  cc_all norm_scope  shift_scope  n_end n_stable
clear lamda_s  temp1_s  temp2_s cc_s
toc
end
 %%
 for n=n_stable+1:  n_end
% store values  of the signal  that will  be stretched and the Base Signal  in
% dummy  variables
t_old_scope(:,1)=norm_scope1(:,1,n);
```

```
v_old_scope(:,1)=norm_scope1(:,2,n);
t_stable_scope(:,1)=norm_scope1(:,1,n-1);
v_stable_scope(:,1)=norm_scope1(:,2,n-1);
% initialize a counter to track the iteration number for lamda
count=1;
% Initialized FOR loop to get the CC=f(lamda) curve
for lamda=1:-0.001:0.7
t_new(:,1)=t_old_scope(:,1).*lamda; % Calculate stretched time
scope_new(:,:)=[t_new v_old_scope]; % new signal with the new time and the old V
ts1(:,1)=timeseries(v_old_scope(:,1),t_new(:,1)); % time-series of stretched signal
% Construct a time-series element from the base signal
tsBase(:,1)=timeseries(v_stable_scope(:,1),t_stable_scope(:,1));
% Synchronize the time values of the two signals to permit cross-correlation
[temp1, temp2]=synchronize(ts1,tsBase,'Union');
% Do the cross-correlation to determine the similarity between signals
v1(:,1)=temp1.data; % new V of scope
v2(:,1)=temp2.data; % new V of stable scope
v1v2(:,1)=v1(:,1).*v2(:,1); % multiplication of V
cc=sum(v1v2); % sum of V1*V2 - cross correlation
% save for count (one scope)
lamda_s(count,1)=lamda;
temp1_s(:,count)=temp1(:,:);
temp2_s(:,count)=temp2(:,:);
```

```
cc_s(count,1)=cc;
clear t_new scope_new ts1 tsBase temp1 temp2 v1 v2 v1v2 cc
count=count+1;
end
lamda_all(:,n)=lamda_s(:,1);
cc_all(:,n)=cc_s(:,1);
save results_scopes2 lamda_all cc_all norm_scope shift_scope n_end n_stable
clear lamda_s temp1_s temp2_s cc_s
toc
end
%% Find max cc and lamda
load('results_scopes2') %% read scopes
lamda_max=0;
for n=n_stable:-1:1
% When n==10 =stable scope, pass to the next iteration
if n==n_stable
lamda_max_s(n,1)=1;
continue
end
% Find max value of cc for each scope
max_cc(1,1)=max(cc_all(:,n));
% Find the positiom of the maximum value of cc
pt = find(cc_all(:,n)==max_cc(1,1));
```

```
% Find lamda for this position
if n==n_stable-1
lamda_max=lamda_all(pt,n);
else
lamda_max=lamda_max_s(n+1,1).*lamda_all(pt,n);
end
% Save max cc and lamda
max_cc_s(n,1)=max_cc(:,1);
lamda_max_s(n,1)=lamda_max;
end
for n=n_stable+1: n_end
% Find max value of cc for each scope
max_cc(1,1)=max(cc_all(:,n));
% Find the positiom of the maximum value of cc
pt = find(cc_all(:,n)==max_cc(1,1));
% Find lamda for this position
if n==n_stable+1
lamda_max=lamda_all(pt,n);
 else
lamda_max=lamda_max_s(n-1,1).*lamda_all(pt,n);
 end
% Save max cc and lamda
max_cc_s(n,1)=max_cc(:,1);
```

```
lamda_max_s(n,1)=lamda_max;
end
max_cc_s(n_stable,1)=max(max_cc_s);
%% Plot lamda_max-cc_max
figure(1)
plot(max_cc_s,'ob')
ylabel('CC  [.]')
format_figures
figure(2)
plot(lamda_max_s,'ob')
ylabel('lamda  [.]')
format_figures
n_end=size(norm_scope,3);  %% number  of scopes
figure(3)
hold  on
hold  all
for  i=1:n_end
plot(shift_scope(:,2,i))
end
xlabel('element  number')
ylabel('voltage  [V]')
hold  off
figure(4)
```

```
plot(norm_scope(:,1,n_stable),norm_scope(:,2,n_stable))
xlabel('Time [s]')
ylabel('voltage/Vmax []')
xlim ([0 max(norm_scope(:,1,n_stable))]);
ylim ([-1 1])
format_figures
First_Arrival=input('Give me the first arrival of the Base wave in seconds');
Length=input('What is the travel length??');
Velocity=Length./First_Arrival*lamda_max_s;
save final_results2.mat lamda_max_s max_cc_s norm_scope shift_scope n_stable
Velocity
clear all;
close all;
clc;
```

REFERENCES

AASHO (1962). "The AASHO Road Test, Report 5." *Pavement Research*, Highway Research Board, 86-111.

AASHTO (1993). "Guide for Design of Pavement Structures." AASHTO, Washington, D.C.

ABAQUS (2010). *Standard User's Manual v6.10*.

Abbas, A. R., Papagiannakis, A. T., and Masad, E. A. (2004). "Linear and nonlinear viscoelastic analysis of the microstructure of asphalt concretes." *Journal of Materials in Civil Engineering*, 16(2), 133-139.

Abelev, A. V., and Lade, P. V. (2003). "Effects of cross anisotropy on three-dimensional behavior of sand. I: Stress-strain behavior and shear banding." *Journal of engineering mechanics*, 129(2), 160-166.

Acum, W. E. A., and Fox, L. (1951). "Computation of load stresses in a three-layer elastic system." *Geotechnique*, 2(4), 293-300.

Adu-Osei, A., Little, D. N., and Lytton, R. L. (2001). "Cross-anisotropic characterization of unbound granular materials." *Transportation Research Record: Journal of the Transportation Research Board*, 1757(-1), 82-91.

Ahlvin, R. G., Turnbull, W. J., Sale, J. P., and Maxwell, A. A. (1971). "Multiple-Wheel Heavy Gear Load Pavement Tests. Volume I. Basic Report." A. F. W. Laboratory, ed., U.S. Army Engineer Waterways Experiment Station, Vicksburg, Mississippi.

Al-Qadi, I. L., Wang, H., and Tutumluer, E. (2010). "Dynamic Analysis of Thin Asphalt Pavements by Using Cross-Anisotropic Stress-Dependent Properties for Granular Layer." *Transportation Research Record*(2154), 156-163.

Alshibli, K. A., and Williams, H. S. (2005). "A true triaxial apparatus for soil testing with mixed boundary conditions." *ASTM geotechnical testing journal*, 28(6), 534-543.

Arthur, J. R. F., and Menzies, B. K. (1972). "Inherent anisotropy in a sand." *Geotechnique*, 22(1), 115-128.

ASCE (2013). "Report Card for America's Infrastructure." *America's Infrastructure*, ASCE, ed.

Bang, E.-S., and Kim, D.-S. (2007). "Evaluation of shear wave velocity profile using SPT based uphole method." *Soil dynamics and earthquake engineering*, 27(8), 741-758.

Barden, L. (1963). "Stresses and Displacements in a cross-anisotropic soil." *Geotechnique*, 13(3), 198-210.

Barden, L., and Sides, G. R. (1970). "Engineering behavior and structure of compacted clay." *Journal of Soil Mechanics & Foundations Div*.

Barker, W. R., Brabston, W. N., and Townsend, F. C. (1973). "An Investigation of the Structural Properties of Stabilized Layers in Flexible Pavement Systems." US Army Engineers Waterways Experiment Station.

Barksdale, R. D. (1984). "Performance of Crushed-Stone Base Courses." *Transportation Research Record*, 954, 78-87.

Barksdale, R. D., Brown, S. F., and Chan, F. (1989). *Potential benefits of geosynthetics in flexible pavement systems*.

Barksdale, R. D., and Todres, H. A. (1983). "A study of factors affecting crushed stone base performance." Georgia Institute of Technology, 639.

Bilodeau, J.-P., and Doré, G. (2012). "Water sensitivity of resilient modulus of compacted unbound granular materials used as pavement base." *International Journal of Pavement Engineering*, 13(5), 459-471.

Bishop, A. W., and Blight, G. E. (1963). "Some aspects of effective stress in saturated and partly saturated soils." *Geotechnique*, 13(3), 177-197.

Bishop, A. W., and Wesley, L. D. (1975). "A hydraulic triaxial apparatus for controlled stress path testing." *Geotechnique*, 25(4), 657-670.

Borja, R. I., Chao, H.-Y., Montáns, F. J., and Lin, C.-H. (1999). "Nonlinear ground response at Lotung LSST site." *Journal of geotechnical and geoenvironmental engineering*, 125(3), 187-197.

Brown, S. F. (1996). "Soil mechanics in pavement engineering." *Geotechnique*, 46(3), 381-426.

Brown, S. F., and Pappin, J. W. (1981). "Analysis of pavements with granular bases." *Transportation Research Record*(810).

Buchanan, S. (2010). "Inverted Pavement Systems." *AGG1*.

Burmister, D. M. (1945). "The general theory of stresses and displacements in layered systems. I." *Journal of applied physics*, 16(2), 89-94.

Burmister, D. M., Palmer, L. A., Barber, E. S., Casagrande, A., and Middlebrooks, T. A. "The theory of stress and displacements in layered systems and applications to the design of airport runways." *Proc., Highway Research Board Proceedings*.

Cascante, G., and Santamarina, J. C. (1996). "Interparticle contact behavior and wave propagation." *Journal of Geotechnical Engineering*, 122(10), 831-839.

Cha, M., Santamarina, J. C. K., H.S., and Cho, G. C. (2014). "Small-Strain Stiffness, Shear Wave Velocity and Soil Compressibility." *Journal of Geotechnical and Geoenvironmental engineering (under review)*.

Cho, G. C., and Santamarina, J. C. (2001). "Unsaturated particulate materials-particle-level studies." *Journal of Geotechnical and Geoenvironmental engineering*, 127(1), 84-96.

Choi, C., Arduino, P., and Harney, M. D. (2008). "Development of a true triaxial apparatus for sands and gravels." *ASTM geotechnical testing journal*, 31(1), 32-44.

Claria, J. J., and Rinaldi, V. A. (2007). "Shear wave velocity of a compacted clayey silt." *ASTM geotechnical testing journal*, 30(5), 399-408.

Clayton, C. R. I. (2011). "Stiffness at small strain: research and practice." *Geotechnique*, 61(1), 5-37.

Corté, J., and Goux, M. (1996). "Design of pavement structures: the French technical guide." *Transportation Research Record: Journal of the Transportation Research Board*, 1539(1), 116-124.

Cortes, D. D. (2010). "Inverted Base Pavement Structures." Ph.D., Georgia Institute of Technology, Atlanta, GA.

Cortes, D. D., and Santamarina, J. C. (2013). "The LaGrange case history: inverted pavement system characterisation and preliminary numerical analyses." *International Journal of Pavement Engineering*, 14(5), 463-471.

Cortes, D. D., Shin, H., and Santamarina, J. C. (2012). "Numerical simulation of inverted pavement systems." *Journal Of Transportation Engineering*, 138(12), 1507-1519.

Cunningham, C. N., Evans, T. M., and Tayebali, A. A. (2012). "Gradation effects on the mechanical response of crushed stone aggregate." *International Journal of Pavement Engineering*, 14(3), 231-241.

Dai, S., Wuttke, F., and Santamarina, J. C. (2011). "Coda Wave Analysis to Monitor Processes in Soils " *Journal of Geotechnical and Geoenvironmental engineering*.

Davich, P., Labuz, J., Guzina, B., and Drescher, A. (2004). "Small strain and resilient modulus testing of granular soils." M. DoT, ed., University of Minesota.

Dawson, A., Mundy, M. J., and Huhtala, M. (2000). "European research into granular material for pavement bases and subbases." *Transportation Research Record*, 1721(1), 9.

Delage, P., Audiguier, M., Cui, Y.-J., and Howat, M. D. (1996). "Microstructure of a compacted silt." *Canadian Geotechnical Journal*, 33(1), 150-158.

Donaghe, R. T., and Townsend, F. C. (1976). "Scalping and replacement effects on the compaction characteristics of earth-rock mixtures." *Soil specimen preparation for laboratory testing: ASTM Special Technical Publication*, 599, 248-277.

Drnevich, V. P., Evans, A. C., and Prochaska, A. B. (2007). "A Study of Effective Soil Compaction Control of Granular Soils."

Du Plessis, L., Coetzee, N. F., Hoover, T. P., Harvey, J. T., and Monismith, C. L. "Three decades of development and achievements: The Heavy Vehicle Simulator in accelerated pavement testing." *Proc., GeoShanghai International Conference 2006*, ASCE.

Duncan, J. M., and Chang, C.-Y. (1970). "Nonlinear analysis of stress and strain in soils." *Journal of the Soil Mechanics and Foundations Division*, 96(5), 1629-1653.

Duncan, J. M., Monismith, C. L., and Wilson, E. L. (1968). "Finite element analyses of pavements." *Highway Research Record*.

Duncan, J. M., and Seed, R. B. (1986). "Compaction-induced earth pressures under K0-conditions." *Journal of Geotechnical Engineering*, 112(1), 1-22.

Ekblad, J., and Isacsson, U. (2006). "Influence of water on resilient properties of coarse granular materials." *Road materials and pavement design*, 7(3), 369-404.

Ekblad, J., and Isacsson, U. (2008). "Influence of water and mica content on resilient properties of coarse granular materials." *International Journal of Pavement Engineering*, 9(3), 215-227.

FHWA (1996). "Resilient Modulus of Unbound Granular Base/Subbase Materials and Subgrade Soils Long Term Pavement Performance Protocol 46." Federal highway Administration Pavement Performance Division.

FHWA (2013). "Public Road Length 2011." *Highway Statistics*, FHWA.

Filz, G. M. D., J. M. (1996). "Earth pressures due to compaction: Comparison of theory with laboratory and field behavior." *Transportation Research Record*, 1526, 28-37.

Fleming, P. R., Frost, M. W., and Lambert, J. P. (2007). "Review of lightweight deflectometer for routine in situ assessment of pavement material stiffness." *Transportation research record: journal of the Transportation Research Board*, 2004(1), 80-87.

Fleming, P. R., Frost, M. W., and Rogers, C. D. F. (2000). "A comparison of devices for measuring stiffness in situ."

Freeme, C. R., Maree, J. H., and Viljoen, A. W. (1982). *Mechanistic design of asphalt pavements and verification using the heavy vehicle simulator*, National Institute for Transport and Road Research.

Freeme, C. R., Otte, E., and Mitchell, M. F. (1980). *Economics of Pavement Type Selection for Major Roads*, Pavement type selection committee for the National Transport Commission, Pretoria.

Garg, N., and Thompson, M. R. (1997). "Triaxial characterization of Minnesota Road Research project granular materials." *Transportation Research Record: Journal of the Transportation Research Board*, 1577(1), 27-36.

Gazetas, G. (1981). "Strip foundations on a cross-anisotropic soil layer subjected to dynamic loading." *Geotechnique*, 31(2), 161-179.

GDOT (2005). "Pavement Design Manual." G. D. o. Transportation, ed., GDOT, Atlanta, GA.

GDOT (2013). "Georgia Department of Transportation Fact Book."

Grau, R. W. (1973). "Evaluation of Structural Layers in Flexible Pavement." U.S. Army Engineer Warterways Experiment Station, Vicksburg, Mississippi.

Grêt, A., Snieder, R., Aster, R. C., and Kyle, P. R. (2005). "Monitoring rapid temporal change in a volcano with coda wave interferometry." *Geophysical Research Letters*, 32(6), L06304.

Gustafsson, F. (1997). "Slip-based tire-road friction estimation." *Automatica*, 33(6), 1087-1099.

Hambly, E. C. (1969). "A new true triaxial apparatus." *Geotechnique*, 19(2), 307-309.

Hardin, B. O. (1978). "The nature of stress-strain behavior for soils." *Proceedings of the ASCE Geotechnical Engineering Division Specialty Conference*Pasadena, CA, 3-90.

Heitor, A., Indraratna, B., and Rujikiatkamjorn, C. (2012). "Use of the soil modulus for compaction control of compacted soils."

Hicks, R. G., and Monismith, C. L. (1971). "Factors influencing the resilient response of granular materials." *Highway Research Record*.

Holtz, R. D. (1990). "Guide of Earthwork Construction." *State of the Art Report*, T. R. Board, ed., National Research Council, Washington D.C.

Horne, D., Belancio, G., Carradine Jr, S. A., Gaj, S., Hallin, J., Jackson, N., Jordan, C., Lucas, D., and Zink, R. (1997). "FHWA Study of South African Pavement and Other Highway Technologies and Practices." FHWA, ed.

Indraratna, B., Heitor, A., and Rujikiatkamjorn, C. (2012). "Effect of compaction energy on shear wave velocity of dynamically compacted silty sand soil."

Ismail, M. A., Sharma, S. S., and Fahey, M. (2005). "A small true triaxial apparatus with wave velocity measurement." *ASTM geotechnical testing journal*, 28(2), 113-122.

Jang, D. J., and Frost, J. D. (2000). "Use of image analysis to study the microstructure of a failed sand specimen." *Canadian geotechnical journal*, 37(5), 1141-1149.

Johnson, C. W. (1961). "Comparative Studies of Combinations of Treated and Untreated Bases and Subbases for Flexible Pavements." *Highway Research Board Bulletin*, 289, 44-61.

Jooste, F., and Sampson, L. (2005). "The Economic Benefits of HVS Development Work on G1 Pavements." Department of Public Transport, Roads and Works.

Kaya, Z., Cetin, A. C., B., and Aydilek, A. "Effect of Compaction Method on Mechanical Behavior of Graded Aggregate Base Materials." *Proc., GeoCongress 2012@ State of the Art and Practice in Geotechnical Engineering*, ASCE, 1486-1494.

Kenis, W. J. (1978). "An Interim Design Method for Flexible Pavements Using the VESYS Structural Subsystem.'." US Department of Transportation, Final Report FHWA-RD-77-154.

Kim, D. S., Kweon, G. C., and Lee, K. H. (1997). "Alternative method of determining resilient modulus of compacted subgrade soils using free-free resonant column test." *Transportation Research Record: Journal of the Transportation Research Board*, 1577(-1), 62-69.

Kim, D. S., and Park, H. C. (1999). "Evaluation of ground densification using spectral analysis of surface waves (SASW) and resonant column (RC) tests." *Canadian Geotechnical Journal*, 36(2), 291-299.

Kim, D. S., Shin, M. K., and Park, H. C. (2001). "Evaluation of density in layer compaction using SASW method." *Soil Dynamics and Earthquake Engineering*, 21(1), 39-46.

Kim, M., Tutumluer, E., and Kwon, J. (2009). "Nonlinear pavement foundation modeling for three-dimensional finite-element analysis of flexible pavements." *International Journal of Geomechanics*, 9(5), 195-208.

Kinchen, R. W., and Temple, W. H. (1980). "Asphaltic concrete overlays of rigid and flexible pavements." L. D. o. T. a. Development, ed.Baton Rouge.

Kjellman, W. "Report on an apparatus for consummate investigation of the mechanical properties of soils." *Proc., Proc., 1st Int. Conf. on Soil Mechanics and Foundation Engineering*, 16-20.

Kleyn, E. G. (2012). "Successful G1 Crushed Stone Basecourse Construction." *31st Southern African Transport Conference*.

Kopperman, S. E., Stokoe, K. H., and Knox, D. P. (1982). "Effect of State of Stress on Velocity of Low-Amplitude Compression Waves Propagating along Principal Stress Directions in Dry Sand." DTIC Document.

Kruntcheva, M. R., Collop, A. C., and Thom, N. H. (2005). "Effect of Bond Condition on Flexible Pavement Performance." *Journal of Transportation Engineering*, 131(11), 880-888.

Lade, P. V., and Duncan, J. M. (1973). "Cubical triaxial tests on cohesionless soil." *Journal of the Soil Mechanics and foundations Division*, 99(10), 793-812.

Lee, J. S., and Santamarina, J. C. (2005). "Bender elements: performance and signal interpretation." *Journal of Geotechnical and Geoenvironmental Engineering*, 131(9), 1063-1070.

Lekarp, F., and Dawson, A. (1998). "Modelling permanent deformation behaviour of unbound granular materials." *Construction and Building Materials*, 12(1), 9-18.

Lewis, D. E., Ledford, K., Georges, T., and Jared, D. M. (2012). "Construction and Performance of Inverted Pavements in Georgia." *TRB 91st Annual meeting*.

Li, F., and Puri, V. M. (2003). "Mechanical behaviour of powders using a medium pressure flexible boundary cubical triaxial tester." *Proceedings of the Institution*

of Mechanical Engineers, Part E: Journal of Process Mechanical Engineering, 217(3), 233-241.

Li, J., Pierce, L., and Uhlmeyer, J. (2010). "Use of the AASHTO 1993 guide, MEPDG and historical performance to update the WSDOT pavement design catalog." *Transportation Research Record*, 2776.

Li, R., Schwartz, C. W., Kim, S. H., and Ceylan, H. "Local sensitivity of mechanistic-empirical flexible pavement performance predictions to unbound material property inputs." *Proc., GeoCongress 2012*, ASCE, 1495-1504.

Lim, S., and Zollinger, D. (2003). "Estimation of the compressive strength and modulus of elasticity of cement-treated aggregate base materials." *Transportation Research Record*, 1837, 30-38.

Liu, Q., and Shalaby, A. (2013). "Simulation of pavement response to tire pressure and shape of contact area." *Canadian Journal of Civil Engineering*(ja).

Long, W., Xiaoguang, X., and Hai, L. (2011). "Influence of laboratory compaction methods on shear performance of graded crushed stone." *Journal of materials in civil engineering*, 23(10), 1483-1487.

Lu, Z., Hickey, C. J., and Sabatier, J. M. (2004). "Effects of compaction on the acoustic velocity in soils." *Soil Science Society of America Journal*, 68(1), 7-16.

Majmudar, T. S., and Behringer, R. P. (2005). "Contact force measurements and stress-induced anisotropy in granular materials." *Nature*, 435(7045), 1079-1082.

Maree, J. H., Van Zyl, N. J. W., and Freeme, C. R. (1981). "Effective Moduli and Stress Dependence of Pavement Materials as Measured in Some Heavy-Vehicle Simulator Tests." *Transportation Research Record*, 852, 52-60.

Marek, C. R. J. J., T. R. "Compaction- An Essential Ingredient for Good Base Performance." *Proc., Proceedings of the Conference on Utilization of Graded Aggregate Base in Flexible Pavements*.

Matsuoka, H., and Nakai, T. "Stress-deformation and strength characteristics of soil under three different principal stresses." *Proc., Proc. JSCE,* 59-70.

McVay, M., and Taesiri, Y. (1985). "Cyclic behavior of pavement base materials." *Journal of Geotechnical Engineering,* 111(1), 1-17.

Metcalf, J. B., Romanoschi, S. A., Li, Y., and Rasoulian, M. (1999). "The first full-scale accelerated pavement test in Louisiana: Developments and findings." Minnesota DoT.

Mitchell, J. K. (1981). "State-of-the-art report on soil improvement." *Journal of the Soil Mechanics and Foundations Division, ASCE,* 96.

Mitchell, J. K., Hooper, D. R., and Campanella, R. G. (1965). "Permeability of compacted clay." *Journal of Soil Mechanics & Foundations Div*, 92(SM5, Proc Paper 490).

Mitchell, M. F., and Walker, R. N. "The economics of pavement type selection." *Proc., 3rd international conference on concrete pavement design and rehabilitation*.

Monismith, C. L. (2004). "Evolution of long-lasting asphalt pavement design methodology: a perspective." *International Symposium of Design and Construction of Long Lasting Asphalt Pavements*, Auburn University.

Morgan, J. R. (1966). "The response of granular materials to repeated loading." *Australian Road Research Board Proc*.

Muller, S., Uchanski, M., and Hedrick, K. (2003). "Estimation of the Maximum Tire-Road Friction Coefficient." *Journal of Dynamic Systems, Measurement, and Control*, 125(4), 607-617.

Nazarian, S., Baker, M. R., and Crain, K. (1993). "Development and testing of a seismic pavement analyzer."

NCHRP (2002). "Recommended Standard Method for Routine Resilient Modulus Testing of Unbound Granular Base/Subbase Materials and Subgrade Soils, Protocol 1-28A." National Cooperative Highway Research Program.

NCHRP (2004). "Guide for mechanistic-empirical design of new and rehabilitated pavement structures." N. R. Council, ed.

NCHRP (2008). "NCHRP Synthesis 381: Falling Weight Deflectometer Usage." T. N. A. Press, ed.Washington, DC.

Oda, M., Nemat-Nasser, S., and Konishi, J. (1985). "Stress-induced anisotropy in granular masses." *Soils and foundations*, 25(3), 85-97.

Otani, J., Mukunoki, T., Takano, D., and Chevalier, B. (2013). "Microscopic observation on compacted sandy soil using micro-focus X-ray CT." *Proc. of the 18th ICSMGE, Paris*.

Park, S. W., and Lytton, R. L. (2004). "Effect of stress-dependent modulus and Poisson's ratio on structural responses in thin asphalt pavements." *JOURNAL OF TRANSPORTATION ENGINEERING*, 130(3), 387-394.

Pasten, C. P., Shin, H., and Santamarina, J. C. (2013). "Long-term Foundation Response to Repetitive Loading." *Journal of Geotechnical and Geoenvironmental engineering, under review*.

Proctor, R. R. (1933). "Fundamental principles of soil compaction." *Engineering News Record*, 111(9), 245-248.

Puppala, A. J. (2008). "Estimating Stiffness of Subgrade and Unbound Materials for Pavement Design." *NCHRP*, T. R. Board, ed., TRB, Washington, D.C.

Raad, L., and Figueroa, J. L. (1980). "Load response of transportation support systems." *Journal of Transportation Engineering*, 106(1).

Rasoulian, M., Becnel, B., and Keel, G. (2000). "Stone interlayer pavement design." *Transportation Research Record*, 1709, 60-68.

Ray, L. R. (1997). "Nonlinear tire force estimation and road friction identification: simulation and experiments." *Automatica*, 33(10), 1819-1833.

Roesler, S. K. (1979). "Anisotropic shear modulus due to stress anisotropy." *Journal of the Geotechnical Engineering Division*, 105(7), 871-880.

Romanoschi, S. A., and Metcalf, J. B. (2001). "Characterization of asphalt concrete layer interfaces." *Transportation Research Record: Journal of the Transportation Research Board*, 1778(1), 132-139.

Rothenburg, L., and Kruyt, N. P. (2004). "Critical state and evolution of coordination number in simulated granular materials." *International Journal of Solids and Structures*, 41(21), 5763-5774.

Rowshanzamir, M. A. (1997). "Resilient Cross-anisotropic Behaviour of Granular Base Materials Under Repetitive Loading."

Santamarina, J. C., and Cascante, G. (1996). "Stress anisotropy and wave propagation: a micromechanical view." *Canadian Geotechnical Journal*, 33(5), 770-782.

Schuettpelz, C. C., Fratta, D., and Edil, T. B. (2010). "Mechanistic corrections for determining the resilient modulus of base course materials based on elastic wave measurements." *Journal of Geotechnical and Geoenvironmental engineering*, 136(8), 1086-1094.

Seed, H. B. (1959). "A Modern Approach to Soil Compaction." *Proceedings of the Eleventh California Street and highway Conference*, Institute of Transportation and Traffic Engineering, University of California, 77-93.

Snieder, R. (2006). "The theory of coda wave interferometry." *Pure and Applied Geophysics*, 163(2), 455-473.

Snieder, R., Grêt, A., Douma, H., and Scales, J. (2002). "Coda wave interferometry for estimating nonlinear behavior in seismic velocity." *Science*, 295(5563), 2253-2255.

Tarefder, R., and Rodriguez-Ruiz, J. (2013). "Local Calibration of MEPDG for Flexible Pavements in New Mexico." *Journal of Transportation Engineering*, 139(10), 981-991.

Terrell, R. G., Cox, B. R., Stokoe, K. H., Allen, J. J., and Lewis, D. (2003). "Field evaluation of the stiffness of unbound aggregate base layers in inverted flexible pavements." *Transportation Research Record*, 1837(2003), 50-60.

Theyse, H. L. (2002). "Stiffness, strength, and performance of unbound aggregate materials: application of South African HVS and laboratory results to California flexible pavements." *Report produced under the auspices of the California Partnered Pavement Research Program for the California Department of Transportation. University of California*, 76.

Theyse, H. L., De Beer, M., Maina, J. W., and Kannemeyer, L. (2011). "Interim revision of the South African Mechanistic-Empirical pavement design method for flexible pavements." *10th Conference on Asphalt Pavements in Southern Africa*.

Thompson, M. R., Tutumluer, E., and Bejarano, M. (1998). "Granular material and soil moduli review of the literature." *Final Report, COE Report*(0), 1.

Titi, H., Rasoulian, M., Martinez, M., Becnel, B., and Keel, G. (2003). "Long-term performance of stone interlayer pavement." *Journal of Transportation Engineering*, 129(2), 118-126.

TRH (1996). "Structural Design of Flexible Pavements for Interurban and Rural Roads." *TRH4: 1996*, C. o. L. T. Officials, ed., Department of Transport, Pretoria, South Africa.

Tutumluer, E. (1995). "Predicting behavior of flexible pavements with granular bases."

Tutumluer, E. (2013). "Practices for Unbound Aggregate Pavement Layers." *Synthesis*, NCHRP, ed.

Tutumluer, E., and Barksdale, R. D. "Behaviour of Pavements with Granular Bases-Prediction and Performance." *Proc., Unbound Aggregates in Roads Proceedings of the Fourth International Symposium on unbound aggregates in roads*

Tutumluer, E., and Barksdale, R. D. (1995). "Inverted Flexible Pavement Response and Performance." *Transportation Research Record*, 1482, 102-110.

Tutumluer, E., and Seyhan, U. (1999). "Laboratory Determination of Anisotropic Aggregate Resilient Moduli Using an Innovative Test Device." *Transportation Research Record*, 1687(1), 9.

Tutumluer, E., and Thompson, M. R. (1997). "Anisotropic modeling of granular bases in flexible pavements." *Transportation Research Record*, 1577, 18-26.

Uzan, J. (1985). "Characterization of granular material." *Transportation Research Record*, 1022(1), 52-59.

Uzan, J. (1999). "Granular material characterization for mechanistic pavement design." *Journal of transportation engineering*, 125(2), 6.

Uzan, J. (2004). "Permanent deformation in flexible pavements." *Journal of Transportation Engineering*, 130(1), 9.

van Niekerk, A. A., Molenaar, A. A. A., and Houben, L. J. M. (2002). "Effect of material quality and compaction on the mechanical behaviour of base course Materials and pavement performance." *6th International Conference on Bearing Capacity of Roads, Railways and Airfields*Lisbon, Prtugal.

Wang, H. (2011). "Analysis of tire-pavement interaction and pavement responses using a decoupled modeling approach." University of Illinois.

Wang, H., and Al-Qadi, I. L. (2012). "Importance of Nonlinear Anisotropic Modeling of Granular Base for Predicting Maximum Viscoelastic Pavement Responses under Moving Vehicular Loading." *Journal of engineering mechanics*, 139(1), 29-38.

Wardle, L. J. (1977). "A Computer Program for the Analysis of Multiple Complex Circular Loads on Layered Anisotropic Media."

Weingart, R. (2009). "Inverted Base Pavement Design: Georgia and Virginia Experience." *National Aggregate Base Conference*Orlando, FL.

West, R. C., Zhang, J., and Moore, J. (2005). "Evaluation of Bond Strength Between Pavement Layers." *NCAT Report 05-08*, National Center for Asphalt Technology.

Williams, R. R., and Nazarian, S. (2007). "Correlation of resilient and seismic modulus test results." *Journal of materials in civil engineering*, 19(12), 1026-1032.

Yoo, P. J., Al-Qadi, I. L., Elseifi, M. A., and Janajreh, I. (2006). "Flexible Pavement Responses to Different Loading Amplitudes Considering Layer Interface Condition and Lateral Shear Forces." *The International Journal of Pavement Engineering*, 7(1), 73-86.

Youn, J. U., Choo, Y. W., and Kim, D. S. (2008). "Measurement of small-strain shear modulus G max of dry and saturated sands by bender element, resonant column, and torsional shear tests." *Canadian Geotechnical Journal*, 45(10), 1426-1438.